Surface and bulk studies of iron phthalocyanine based gas sensors.

O'ROURKE, Jacqueline K.

25/2
17.00

15/3/95
20:59

18/3 17.00

19/3 8 pm

20.50

21/3 17.42

20/3/96.
20:59

BRN 306014

SURFACE AND BULK STUDIES OF IRON PHTHALOCYANINE BASED GAS SENSORS

JACQUELINE KAREN O'ROURKE B.Sc.

A thesis submitted in partial fulfilment of the
requirements of
Sheffield Hallam University
for the degree of Doctor of Philosophy

September 1994

Collaborating Organisation: The Health and Safety Executive

SURFACE AND BULK STUDIES OF IRON PHTHALOCYANINE BASED GAS SENSORS

ABSTRACT

Phthalocyanines films have been noted for their use as chemical sensors by measuring changes in conductivity when a gas is adsorbed at the surface. The sensing mechanism is not well understood. This work uses iron phthalocyanine as a model in an attempt to understand the gas sensing mechanism of metal phthalocyanines.

The alpha and beta polymorphs of iron phthalocyanine (FePc) have been synthesised and then studied using infra-red spectroscopy, scanning electron microscopy (SEM), gas sensing experiments and Mössbauer spectroscopy.

Infra red spectroscopy indicates that a phase change occurs at 205°C and SEM work confirms this since the microcrystallite size changes at this temperature.

Gas sensing work has shown that FePc responds to NO_2 and Cl_2 at room temperature. Variable temperature transmission mode Mössbauer spectroscopy of both phases showed that the alpha phase has a lower recoil free fraction at room temperature than the beta phase suggesting that the beta phase has a more rigid structure i.e. it is less free to vibrate in the lattice than the alpha phase. This also explains the difficulties experienced in attempts to collect backscatter spectra from alpha FePc.

Backscatter Mössbauer spectroscopy has been used in vitro to show a difference at ambient temperature and pressure, of beta FePc before and after exposure to a gas. Conversion electron Mössbauer spectroscopy indicates that NO_2 adsorbs on to the surface of the FePc film preventing the escape of conversion electrons, and conversion x-ray experiments have shown that the NO_2 penetrates the near surface causing a chemical change.

CONTENTS

CHAPTER 1 - LITERATURE REVIEW

CHAPTER TWO - MÖSSBAUER SPECTROSCOPY

CHAPTER THREE - TECHNIQUES

CHAPTER FOUR - EXPERIMENTAL - PREPARATION

CHAPTER FIVE - EXPERIMENTAL

CHAPTER SIX - CONCLUSIONS

CHAPTER ONE

LITERATURE REVIEW

1 INTRODUCTION

The following chapter contains a literature review of the broad area of sensors, the physical and chemical properties of the phthalocyanines, phthalocyanines as chemical sensors, and previous Mössbauer work reported with iron phthalocyanine and related compounds. A summary of iron oxides in the field of sensing is also included.

1.1 SENSORS

A sensor can be described as a device which can change a physical or chemical parameter into an electrical or optical signal. Examples of physical parameters which are monitored are temperature, pressure, force and magnetic field. The chemical parameters are the concentrations of chemical substances.

Chemical sensors need to be specific and selective because there are a large number of chemical parameters i.e. there are a large number of gas pollutants in air and a high number of proteins in the human body. The physical sensors for temperature, acceleration etc, can be hermetically encapsulated unlike the chemical sensors which are affected by interfering substances and are also susceptible to environmental effects such as light or corrosion.

Sensor technology is multidisciplinary. The areas of physics and electronics, are combined with chemistry, biochemistry, and electrochemistry. This means that it is necessary for scientists to cross the disciplinary boundaries forming interdisciplinary research groups (1).

The applications for chemical sensors is infinite. The obvious applications are :

- in chemical laboratories
- in medical clinics
- in industrial processes and bioreactors
- in monitoring air pollution
- in field analysis of plants and soil

The work covered by this research is related to the applications within environmental monitoring. Long term exposure to even trace amounts of hazardous gases have been shown to have severe medical implications. Therefore health authorities require portable sensing apparatus and industry needs systems to alert against elevated levels of toxic and explosive gases.

Gas sensors must be highly sensitive and selective as they are required to measure very low concentrations. It has been easier to develop sensors for the more reactive gases than for the less reactive gases which are also toxic. The lower explosive limit (LEL) for the explosive gases is usually in the per cent range, hence these are easier to monitor than the toxic gases which have exposure limits in the part per billion range.

There are a wide range of chemical sensors available including:

- thermal sensors
- mass sensors
- optical sensors
- electrochemical sensors.

Each of these sections which will be looked at briefly. The major area of interest to this work is the electrochemical sensors so this will be reviewed in most detail.

1.2 THERMAL SENSORS

Thermal sensors are the smallest group represented amongst the chemical sensors. The evolution of heat is the general property of any chemical reaction and so could be thought of as an ideal property to use for sensing. However the flow of heat is not easily controlled. Enzymatic reactions act as chemically selective heat generators and as a result many thermal sensors involve enzymes for their selectivity (2). Enzymatic thermistors (enzyme-linked immunoassay with thermometric detection (4)) are the most significant chemical sensors (5), which combine the enzyme specificity with the universal character of the thermochemical approach (6). Pyroelectric devices have received some attention (7), since they have a very high sensitivity and are capable of measuring the heat of absorption corresponding to a monolayer of gas.

1.3 MASS SENSORS

Mass sensors use a change in mass as their basis for chemical sensing. The principle can be applied to any reactions in which there is a change in mass. This omits most of the selective catalytic reactions including the enzymatic ones (2).

Two types of mass chemical sensors exist: those based on piezoelectric bulk oscillators, and those based on surface acoustic wave (SAW) devices. Chemosensors based on piezoelectric crystals using bulk acoustic waves have been around for some time (8). The first SAW gas sensor used a SAW delay line, covered with a polymer, placed in the feedback loop of an amplifier and the oscillator frequency was measured (9). SAW devices are attractive for chemical sensor application owing to their small size, low cost, sensitivity and reliability (10).

The SAW sensors have been used to detect inorganic gases i.e. nitrogen dioxide (11), and organic vapours.

1.4 OPTICAL SENSORS

The development of optical hardware for communication applications led to an interest in optical sensors. They have a suitability for remote (kilometres) sensing and safety in their operation. Minimal encapsulation is required and fabrication of miniature single-ended probes is possible (2).

Ionic sensors use the optical sensing of pH (12). Such "optrodes" use fluorescence as the mode of transduction and some use multiple wavelength to further suppress interferences. pH can also be measured using an electrometric method. The major difference is that the optical method measures the number of molecules (concentration), whilst the potentiometric measurement is based upon the chemical activity, which is a measure of reactivity.

Optical gas sensors based on fluorescence quenching and optical biosensors are other areas of optical sensing (2).

1.5 ELECTROCHEMICAL SENSORS

The response in electrochemical sensors arises from a change in the electrical properties of a material. There are three types of electrochemical sensor:

- potentiometric sensors
- amperometric sensors
- conductometric sensors.

1.5.1 Potentiometric Sensors

This group of sensors is based on the measurement of cell voltage. The ion sensors contain conventional ion selective electrodes (ISE) as a group. The ISE consists of electrodes which have an ion-selective membrane positioned symmetrically between two solutions. There are also a group of ion sensors which have a solid-state internal contact, these include;

- coated wire electrodes
- hybrid sensors
- extended gate field effect transistors
- ion-selective field effect transistors.

Biosensors are the largest section within the potentiometric field, they are devices which derive their selectivity from a biochemical process with a common and distinguishing process. Use of enzymes particularly glucose oxidase in glucose sensors are dominant in this group.

High temperature potentiometric gas sensors use solid-state electrolytes. Solid-state galvanic cells have proved to be the most sensitive and accurate method of measuring oxygen activities in gases, liquids and solids (13). Stabilized zirconia is the material used for many oxygen sensors (2).

1.5.2 Amperometric Sensors

This group of sensors is based upon the measurement of cell current. Again this group includes a few sections which will be briefly mentioned. The sizes of these sensors can be small, in the order 10μm for fibre and capillary electrodes (6). However amperometric sensors do not necessarily have micrometer dimensions. Modified electrodes achieve selectivity through the control of selective mass transport (i.e., permselectivity, accumulation) and through the control of charge-transfer kinetics. Amperometric biosensors are a subset of modified electrodes. The modifier is the layer which contains the reagent, and the modifier facilitates the electron transfer between the electrode and the substrate in the solution (6). The oldest and most researched group of amperometric biosensors is based on oxygen. The Clarke electrode is one in which the information about the concentration of the substrate is obtained from the effect of the enzymatic reaction on the reduction current of oxygen.

A Clarke-type oxygen electrode is a form of direct amperometric gas sensor and has been used for sensing oxygen, hydrogen, and volatile organic solvents (6).

There are amperometric enzyme sensors which are used for glucose sensing and come under the heading of biomedical applications and are used for diabetics.

1.5.3 Conductometric Sensors

Conductometric sensors are based on the measurement of chemically induced conductivity changes. There are electrical contacts in the surface, in the bulk, and at the interface between the sensing material and the supporting substrate, at which changes occur.

Conductometric sensors may be operated in a dc or an ac mode. In the ac mode, the frequency of the applied signal also becomes important. As mentioned earlier, this section will be reviewed in greater depth than the previous ones owing to its major relevance to this project. The sub sections in the conductometric sensors are:

- semiconductor theory
- fabrication
- dielectrometry
- semiconducting oxides
- chemiresistors.

1.5.3.1 Semiconductor Theory

Semiconductors are materials with electrical conductivities between insulators and conductors. Very pure semiconductors are called intrinsic semiconductors and those to which impurities have been added (which affects the conduction of electricity) are called extrinsic semiconductors.

Intrinsic Semiconductors

Silicon and germanium are tetravalent. At 0K all the valence electrons are involved in bonding and the crystal is an insulator. At higher temperatures some valence electrons break away from the bonds leaving a vacancy or 'hole' in the lattice. The hole is a region of excess positive charge. An electron in its random motion path is likely to fill the 'hole'. Holes are being continually filled and created as electrons are released from their bonds. It appears as if holes are moving randomly through the structure. There are two types of charge carriers in semiconductors, holes (positive) and electrons (negative).

Extrinsic Semiconductors

Doping a tetravalent element with a pentavalent or trivalent element produces an increase in conductivity without distorting the basic crystal structure.

n-type Semiconductors

Addition of pentavalent antimony (Sb) to germanium (Ge) as in figure 1.1, produces an n-type semiconductor.

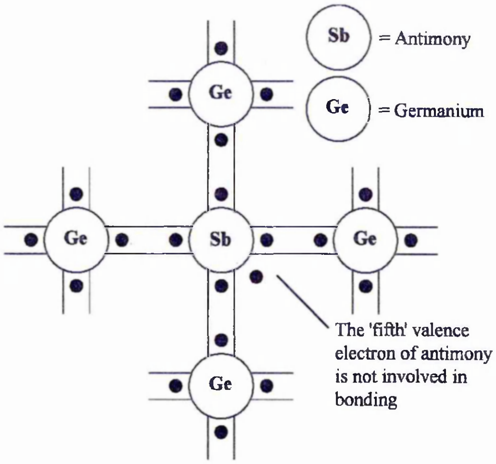

Figure 1.1 The effect of adding a pentavalent impurity into a germanium crystal.

Only four of the five Sb electrons are involved in bonding. The fifth electron is loosely bound and the average thermal energy of the lattice ions is enough to liberate the surplus electrons from their parent nuclei. Conduction electrons are donated to the structure. The negative charge carriers (electrons) are involved when it conducts electricity hence an n-type semiconductor. The majority carriers are electrons and the minority carriers are holes. The crystal is electrically neutral because the excess negative charge associated with the charge carriers is balanced by the excess positive charge at the sites of the Sb nucleus.

p-type Semiconductors

Addition of a trivalent impurity i.e. indium (In) to germanium (Ge) as in figure 1.2, produces a p-type semiconductor.

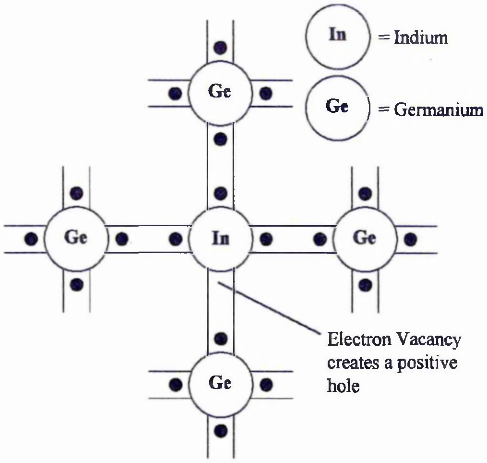

Figure 1.2 The effect of adding a trivalent impurity into a germanium crystal.

Indium forms bonds with three of its four Ge neighbours. At room temperature lattice vibrations provide energy to move an electron from a nearby Ge-Ge bond to fill the vacancy and thus leave a hole in one of the Ge atoms. Majority carriers in a p-type material are holes and as with the n-type semiconductor the crystal is electrically neutral.

Band Theory Treatment of Conduction

When two identical atoms are close, their electrons move under the influence of the combined electric fields of both atoms and each previous single energy level splits into two levels, one higher and one lower than the corresponding level of the isolated atoms. When large numbers of atoms are together as in a crystal the energy levels spread into bands. Each band contains a large number of levels which are so close that there is in effect a continuous range of energies available to the electrons. The bands are separated by gaps in which there are no available energy levels. To take part in conduction of an electric current an electron must be able to be accelerated by an applied potential difference and be capable of being raised to slightly higher energy levels. A material conducts electricity if some of its electrons are in a band that is not full, otherwise the energy levels available are in higher bands and the energy differences involved are not permitted. Figure 1.3 compares the energy band diagrams of an intrinsic semiconductor and an insulator.

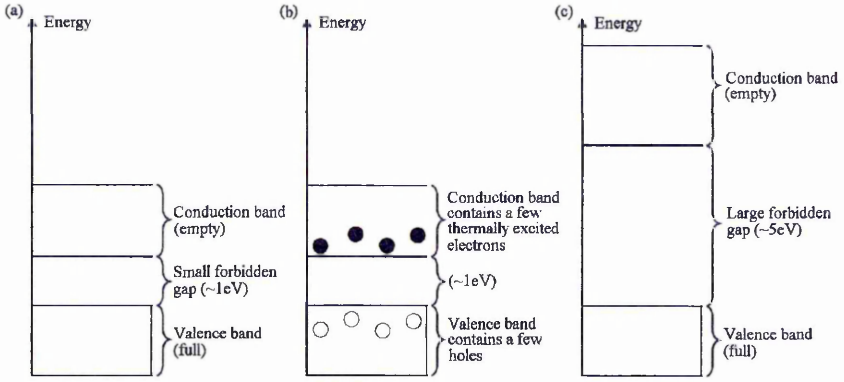

Figure 1.3 Energy band diagrams of (a) an intrinsic semiconductor at 0K, (b) an intrinsic semiconductor at room temperature and (c) an insulator at room temperature.

At 0K the valence band is full and the conduction band empty. The semiconductor behaves like an insulator. At room temperature some electrons in the valence band gain energy from lattice vibrations and move up to the conduction band creating an equal number of holes in the valence band. Conductivity increases with temperature as there is more thermal excitation of electrons into the conduction band. Insulators have full valence bands and empty conduction bands. The forbidden gap is large and at room temperature the few electrons acquiring enough energy to cross the gap is insignificant.

Band Theory of Extrinsic Semiconductors

In a n-type semiconductor there are extra energy levels below the conduction band. At room temperature lattice vibrations provide the energy necessary to raise the electrons to the conduction band where they can conduct an electric current. Figures 1.4 and 1.5 show the energy bands of p- and n-type semiconductors.

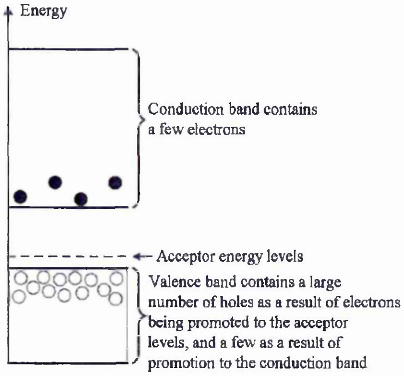

Figure 1.4 The energy band diagram of a p-type semiconductor.

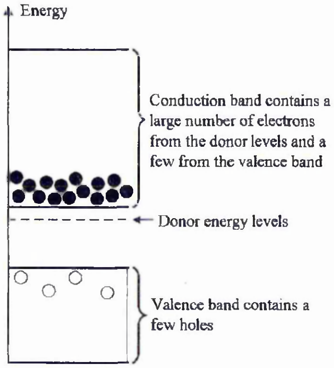

Figure 1.5 The energy band diagram of a n-type semiconductor.

In a p-type semiconductor there are extra energy levels above the top of the valence band. At room temperature these levels are occupied by electrons which have been thermally excited from the valence band. This leaves a large number of holes in the valence band and so there is an increase in conductivity.

1.5.3.2 Fabrication

Gas sensors using the gas-dependent resistance variation of semiconducting oxides have been known for about 30 years (14). Recently their technology was changed using microelectronic technology to produce a gas sensor (15). A laboratory model was manufactured using technology compatible with microelectronics. The most critical point of miniaturization was the heater which determined the size of the sensor. Semiconducting gas sensors have been miniaturized successfully and they can be produced by applying mainly standard semiconductor processes resulting in low costs and high reliability (15). Microelectronic technology has advantages over conventionally fabricated sensors on ceramic substrates in terms of more accurate temperature control and low level of heating power (16).

Conventional low pressure vapour deposition is used to deposit films such as phthalocyanines on to sensor arrays. The film thicknesses are typically up to one micron (17). Thin films of tin dioxide (200nm) are produced using a sputtering technique (18). An alternative method to thermal evaporation is to use thick-film screen printing as a deposition technique. The phthalocyanine compounds are made into screen printable inks, through powdering and the addition of solvent carriers prior to being printed at thicknesses typically of 25 microns (17). Screen printing has been used for the production of 10μm tin dioxide films and further developed to produce a 200nm thin film (18). Screen printing is quicker, easier and cheaper than thermal evaporation (17).

1.5.3.3 Dielectrometry

These sensors are designed to operate as capacitors in the ac mode. Humidity sensors are the largest group in this section and are designed around alumina, strontium-containing materials, and various ceramics (6). Dielectric biosensors have been designed using the capacitance change caused by enzymatic reactions.

1.5.3.4 Semiconducting Oxides

The materials that are classed in this category include tin oxides, iron oxides, zinc oxide, chromium oxide, indium oxide, niobium oxide, tungsten oxide, titanium oxide, perovskites, mixed oxides of titanium/bismuth, carbon black and vanadium, aluminium/vanadium, indium/chromium, strontium/titanium, bismuth/iron, indium/palladium/lanthanum, strontium/calcium/iron, bismuth/iron/molybdenum, and barium/titanium/lead. Obviously there are too many materials to examine in a great depth so the materials to be reviewed in this section are:

(i) tin oxides

(ii) iron oxides

(i) Tin Oxide Gas Sensors

Tin oxide is the most studied sensor material and it responds to reducing gases in air by undergoing a change in resistance. They are an attractive option as a gas alarm owing to their high sensitivity, cheapness and simplicity (19). Experiments have been conducted using tin oxides for detecting gases such as carbon monoxide (20, 21, 22, 24), methane (20, 21, 25), nitrogen oxides (20), hydrogen (21, 22, 23), sulphur dioxide (20), water vapour (26, 27), and oxygen (26, 27).

(ii) Iron Oxide Gas Sensors

Fe_2O_3 has two modifications, alpha (haematite) and gamma (maghemite). Both these modifications have gas sensitive properties as does magnetite (Fe_3O_4). Ferromagnetic γ-Fe_2O_3 can be obtained from the oxidation of Fe_3O_4 or the dehydration of γ-FeOOH. It has a spinel type structure and is transformed to the anti-ferromagnetic alpha modification at 400°C (28). This α-Fe_2O_3 has a corundum type rhombohedral structure. Reduction of the γ or α form results in ferrimagnetic Fe_3O_4. Gas sensitive characteristics have been observed in γ-Fe_2O_3 ceramics, characterised by the decrease in electrical resistance when placed in contact with reducing gases (29). Haematite has a high chemical stability and as a result is generally gas insensitive. However it was found that a large gas sensitivity resulted from the preparation of haematite ceramics from iron salt containing sulphate ion by a wet process. The sulphate ion remains in the ceramic and has an important role in inducing a fine crystallite and low crystallinity, and a large gas sensitivity. Vaporisation of the sulphate ion at 760°C results in a decrease in the gas sensitivity with crystallization and microscopic grain growth. The presence of the sulphate ion affects the microstructure and hence gas sensitivity. It was also found that the sensitivity could be greatly enhanced by the addition of quadrivalent metal eg. titanium, zirconium, or tin (30). There is a relationship between the gas sensitive properties and the microstructure as a parameter of the residual sulphate ion (i.e. the sulphate ion vaporises at 750°C resulting in grain growth and crystallinity accompanying a decrease in gas sensitive properties (28)).

Thin film type gas sensors have been developed and it is supposed that the chemisorption of the gas on the surface of a semiconductor leads to the addition or removal of localised charges on the surface. This is detected by the change in conductivity of the film (31).

A highly sensitive sintered haematite gas sensor was reported in 1985 (32) which was very sensitive to methane but not very sensitive to smoke or alcohol and therefore gives little danger of false alarms from such sources. The major part of the sensor is a sintered haematite body which affects the grain size, increases porosity and also increases the surface area, hence making the sensing element active and produces a sensitivity and selectivity towards methane which owing to its high stability can be difficult to detect. Haematite and maghemite have surface resistivities which decrease in an atmosphere of combustible gases such as methane, propane, and isobutane. The haematite and maghemite gas sensors function at a temperature of 400°C and 250°C respectively and have been studied using conversion electron Mössbauer spectroscopy with the following conclusions (33):

- in the α sensor the sulphate ion and microstructure of fine particles plays an important role in the sensing mechanism. A decrease in resistivity in the sensors was caused by the production of a small amount of Fe(II) species (conduction mechanism was not clear).
- in the γ sensor, the decrease in resistivity was a result of a redox reaction at the surface and the gas sensitivity depended on the crystal structure (33).

Thick film haematite (with sulphate and tin incorporated) gas sensors have been fabricated using screen printing technology. The haematite was deposited at different pH values and exhibited different microstructures. The sulphate ion as mentioned enhanced the sensitivity to methane. Sulphur existed as S^{2-} and SO_4^{2-} ions at the surface but only as SO_4^{2-} in the bulk. α-alumina added to mechanically strengthen the film decreased the sensitivity to methane but the sensitivity recovered to some extent when palladium was added to the thick film. The palladium assumed the form of PdO at the surface but the metallic form in the layer below the surface (34).

The microstructure and humidity sensitive characteristics of haematite porous ceramics have been examined. The conclusions were that the humidity sensitive properties of a ceramic material can be governed by controlling the shape, dimension, sintering conditions, and intergranular porosity of the precursor powder (35).

Selectivity and Sensitivity

Selectivity studies on tin oxide based semiconductors have shown that selectivity can be enhanced by operation of the sensor at different temperatures i.e. at 300°C the tin oxide sensor has an enhanced response to the presence of carbon monoxide but none to methane which gives an enhanced response at temperatures above 600°C (24). There are four ways of obtaining selectivity in semiconductor gas sensors:

- the use of temperature control (already mentioned)
- the use of catalysts and promoters
- the use of specific surface additives
- the use of filters (36, 38).

Various coatings have been used to consume gases that are not wanted to pass to the gas sensor or to permit the passage of selected gases to the sensor. For example hydrogen sensitivity can be obtained by use of a silica surface layer since hydrogen passes through silica more freely than hydrocarbons (36, 38).

Selectivity can be obtained if material which specifically adsorbs or reacts with the gas of interest is placed on the surface of the semiconductor. One obvious example of this is the use of hygroscopic salts to concentrate water in humidity sensors (36, 38).

Catalysts impart speed of response and selectivity in gas sensors, and promoters are surface additives that are not catalysts but help the selectivity or reactivity of the catalyst (36). Noble metal catalysts such as platinum, palladium, or rhodium are used to activate the sensing elements of the metal oxides (37)

Sensitivity of gas sensors can be affected by the use of different particle size (22), or by the addition of an activator or sensitiser i.e. addition of silver to tin oxide increases the sensitivity to hydrogen in preference to propane, or methane thus enabling the selective detection of hydrogen (36).

1.5.3.5 Chemiresistors

This type of conductometric sensor is popular due to its ease of preparation and low cost. The principle is to measure changes of conductivity in the chemically selective layer (2).

Most chemiresistors are based upon phthalocyanines. In the pure state phthalocyanines (Pc's) have low conductivity. When an electron acceptor gas such as nitrogen dioxide (NO_2) is adsorbed onto the surface, electrons are transferred from their closely bound states within the phthalocyanine molecules leaving vacancies ('holes'). The material becomes a p-type semiconductor in the vicinity of the surface. The change in electrical characteristics can be detected in the presence of low concentrations of such gases. These materials have a large potential for highly sophisticated sensing applications (39).

To be useful as a gas sensor, a semiconductor requires the following properties (40):

- the conductivity of the material must vary with the concentration (in ambient air), of the gas to be measured.
- the conductivity effect must be reversible returning to its original value in the absence of the gas.
- reproducibility of response if the sensor is to be used in instruments.
- the material needs to be stable when heated to temperatures high enough for the reaction of interest to take place quickly and reversibly, and to temperatures greater than 100°C to minimize water condensation effects.
- economic factors require that fabrication should be cheap.
- it would be advantageous to be able to modify the structure of the semiconductor in order to vary the sensitivity to various gases.

The phthalocyanines satisfy most of these conditions. Oxygen affects the electrical conductivity of copper, cobalt, lead, magnesium (41), and zinc (42) phthalocyanines.

Lead phthalocyanine shows a response and recovery to NO_2 (43, 44, 45). Ammonia causes a decrease in conductivity in zinc phthalocyanine (42).

Most phthalocyanines are stable up to 400-500°C (46) at which temperature the material decomposes but does not melt (40).

Before discussing the various gas sensors based on the phthalocyanines the structure, phases and properties of the phthalocyanines will be presented.

1.6 PHTHALOCYANINES

The synthesis of phthalocyanine was an accidental discovery when a small amount of blue precipitate was isolated after heating o-cyanobenzamide in alcohol (43). Linstead and co-workers reported the synthesis of many metal phthalocyanines and suggested that the phthalocyanine moiety consisted of four units of isoindole and possessed a highly conjugated system (48, 49). The basic structure of phthalocyanine consists of four pyrrole rings inter connected by nitrogen bridges. In the phthalocyanines there is a benzene ring fused to each pyrrole subunit. The giant ring structure is planar and fully conjugated except for PbPc in which the metal atom is above the plane of the rest of the molecule (50).

X-ray diffraction has been used to confirm the structure of CuPc (51, 52), CoPc(53), SnPc(54), FePc(55), H_2Pc, BePc, MnPc, PtPc (56). Metal phthalocyanines show intense absorption in the red region of the visible spectrum and the colour of the solids range from dark blue to metallic bronze to green, depending on the central metal, the crystalline form and the particle size (57). They are used as colorants for plastics, ink, fabrics and automobile paints. They also have interesting optical, magnetic, catalytic, semiconductive and photoconductive properties (58, 59).

1.6.1 Synthesis and Structural Variation

Many procedures for the synthesis of metal phthalocyanines exist and are summarised in figure 1.6.

A variety of phthalocyanines can be synthesised depending on the metal salt and the valence of the metal. Monovalent elements produce M_2Pc (M = H, Li), whereas divalent ions such as magnesium result in MgPc. Metals which are trivalent can form hydroxy or halogenometal phthalocyanines eg. AlOHPc and AlClPc. In the case of tetravalent metals, compounds such as oxy, dihydroxy, or dihalogeno phthalocyanine may be formed eg. TiOPc, $Si(OH)_2Pc$, and $SiCl_2Pc$. To date nearly all metals and semi-metals are known to form complexes with the phthalocyanine ligand (58, 59).

Substitutions on the phthalocyanine ring can also cause structural variations (60, 61). These substituents usually enhance the solubility of the phthalocyanines in solvents and induce morphological changes in the solid state due to steric effects. The change in morphology can affect the photoconductivity.

1.6.2 Optical Absorption and Electronic Structure

The absorption spectra of a number of phthalocyanines in solution have been studied: H_2Pc (62, 63), CuPc (62), ZnPc (64), FePc (63), NiPc (65), CoPc (65), PdPc (65), and MgPc (65). This data revealed that phthalocyanines have two absorption bands one in the visible region at about 600-700nm and the other in the near UV region at about 300-400nm. H_2Pc shows two clear vibronic bands at about 698.5nm and 663nm in 1-chloronaphthalene solution, but most phthalocyanines show only one absorption band and an absorption shoulder in the visible region. The visible absorption of phthalocyanine is not sensitive to the central metal atom.

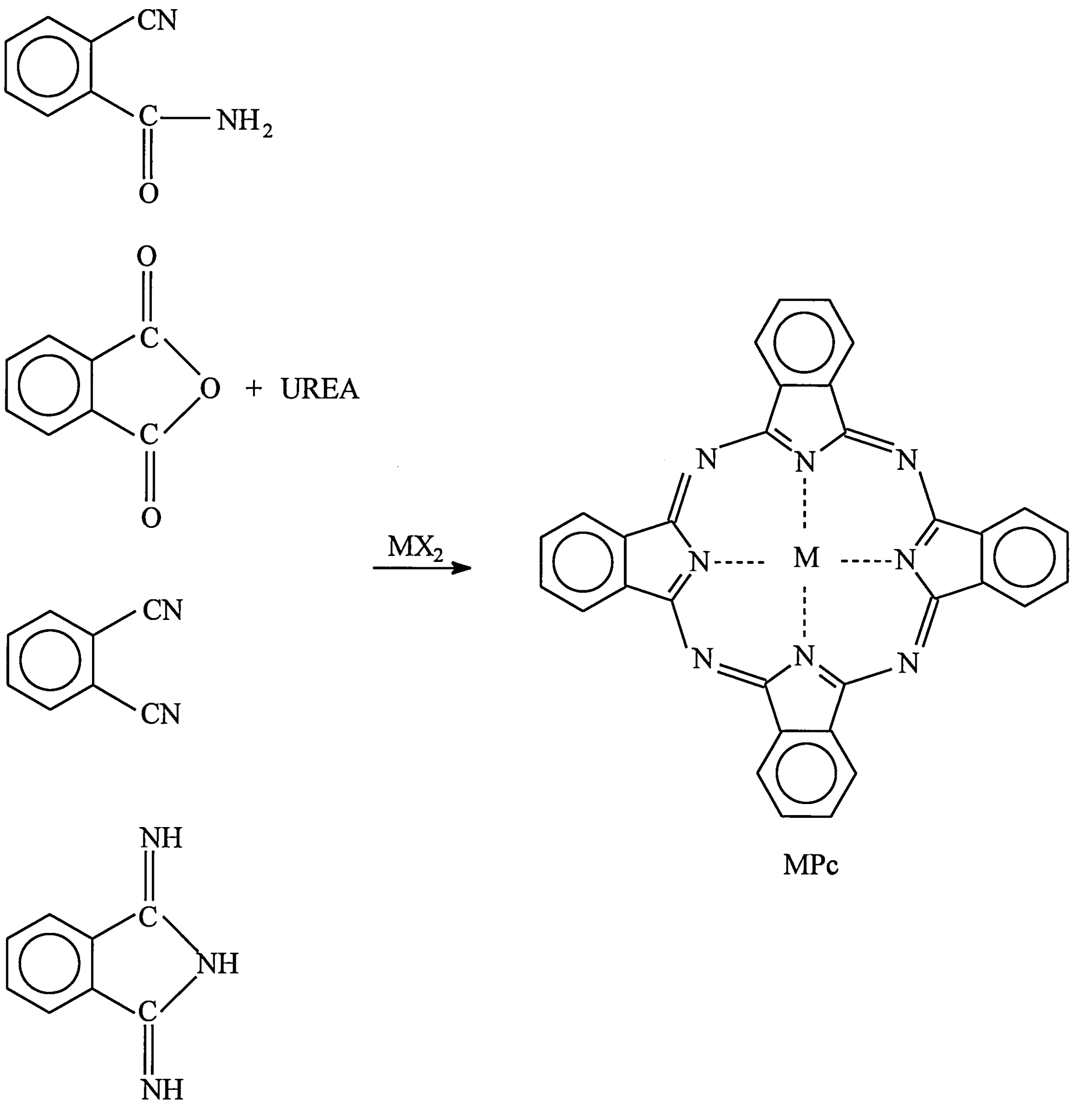

Figure 1.6 Various syntheses of metal phthalocyanines.

Theoretical molecular orbital studies have shown that the $\pi \rightarrow \pi^*$ transition within the delocalised phthalocyanine ring system gives rise to the visible absorption band. The $\pi \rightarrow \pi^*$ transition involves a charge transfer from the outer benzene rings of the phthalocyanine to the inner macrocyclic ring (57).

1.6.3 Polymorphism in Phthalocyanines

Polymorphism is a common phenomenon in the phthalocyanines. This occurs because the intermolecular forces between phthalocyanine molecules are relatively weak allowing a variety of molecular stacking arrangements of similar interaction energies.

1.6.3.1 Metal Free Phthalocyanine (H_2Pc)

H_2Pc exists in four polymorphic forms in the solid state. These forms are the α, β, χ, and τ forms (57). The β-form is the most stable polymorph (66) and can be formed by direct synthesis or recrystallisation (57, 67). Single crystals of the β-form can be obtained by sublimation at 550°C (66). α-H_2Pc is obtained by precipitation from concentrated sulphuric acid upon addition of water (68) or by sublimation in thin films (68).

The χ-phase is produced by milling α-H_2Pc for one week. Thin films of χ-H_2Pc are produced by deposition of χ-H_2Pc in heptane on to potassium bromide (KBr) or pyrex windows and allowing evaporation of the heptane (66). The solid state spectra and x-ray diffraction patterns of these three polymorphs are known and the spectra and diffraction patterns of τ-H_2Pc and χ-H_2Pc are similar.

1.6.3.2 Copper Phthalocyanine (CuPc)

CuPc exhibits five polymorphic forms (α, β, γ, δ and ε) (69). The β-form is the most stable polymorph (70) formed by vacuum sublimation of the crude material (71). The α-CuPc is obtained by acid pasting β-CuPc (71) or thermal treatment (57). γ, δ and ε CuPc can also be obtained by precipitation from sulphuric acid and are converted to β-CuPc upon heating or recrystallisation from an organic solvent. The five polymorphs of CuPc exhibit characteristic absorption spectra, x-ray diffraction patterns and infrared spectra (57, 72). The molecular arrangements for α and β phases of CuPc are shown in figure 1.7.

1.6.3.3 Zinc Phthalocyanine (ZnPc)

ZnPc exists in two polymorphic forms, the α and the β forms. β-ZnPc can be obtained by recrystallisation of the crude material resulting in the formation of needle-like crystals, whereas the α-modification is obtained by the acid paste method (76). X-ray diffraction and transmission electron microscopy have been used to study the polymorphs of thin film ZnPc (77). The existence of an intermediate crystal form during transformation of α to β ZnPc in the vapour of various alcohols was found (78).

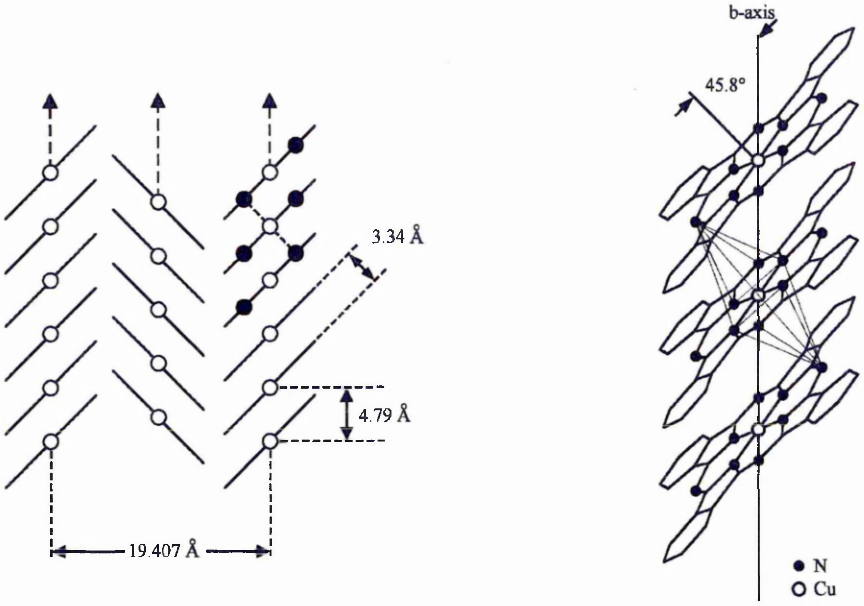

Molecular arrangements of β-CuPc

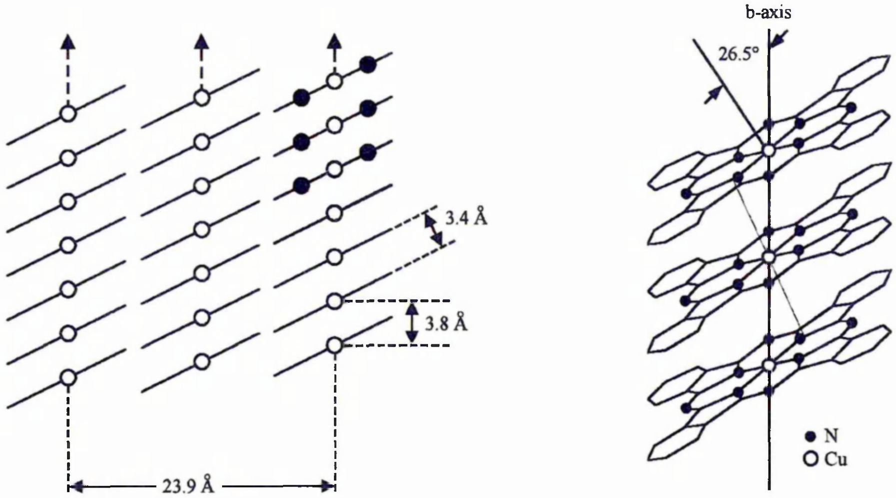

Molecular arrangement of α-CuPc

Figure 1.7 Molecular stacking arrangements of α and β-CuPc.

1.6.3.4 Lead Phthalocyanine (PbPc)

PbPc exists in both α and β forms. The α-phase consists of small crystallites of monoclinic material whilst the β-phase is triclinic and consists of larger rod-like crystals (73). X-ray crystal structure analysis of monoclinic PbPc showed the molecules arranged in a closely packed molecular column where Pb atoms form a one dimensional chain with a short interatomic distance (74). In the β-form the molecules stack along the a axis orienting their convex and concave sides alternately (75).

Crystals of both α and β forms of PbPc are produced by entrainer sublimation, the former being deposited at 523K and the latter at 593K (75). Films of α and β PbPc are obtained by varying the substrate temperature during evaporation (73). Thermal treatment converts the α phase to the β phase. The molecular arrangement for the α-phase PbPc molecule is shown in figure 1.8.

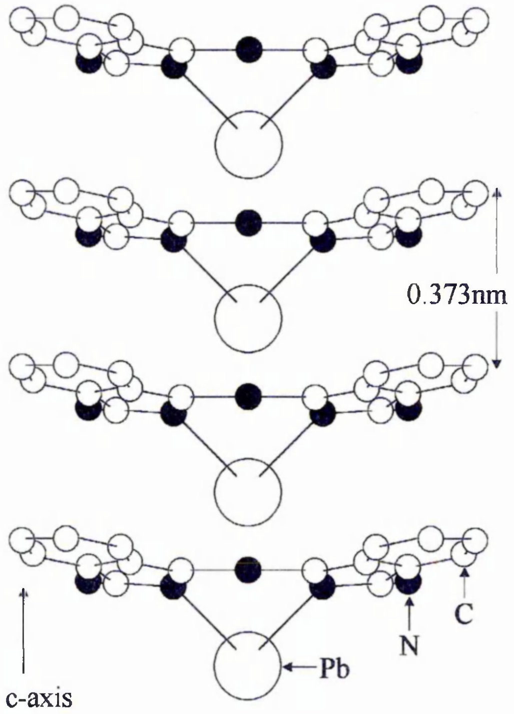

Figure 1.8 Molecular arrangement of α-phase PbPc.

1.6.3.5 Iron Phthalocyanine (FePc)

FePc exists in the α and β polymorphic forms. β-FePc is prepared by entrainer sublimation of the crude material. Vacuum sublimation of the crude material yields both phases, the β-phase being collected on a 'finger' maintained above 250°, and the α-phase onto a water cooled finger (79). Conversion of the α-phase film to the β-phase can be caused by heating at 160°C for 9 days (80). FePc can be used in Mössbauer spectroscopic studies owing to the presence of ^{57}Fe in the compound. The Mössbauer investigations of FePc will be discussed later in this chapter (section 1.7).

1.6.3.6 Summary of Phthalocyanine Morphology

Generally the most common polymorphic forms of H_2Pc and metal phthalocyanines are the α and β. The β-form can be formed by entrainer sublimation, vacuum sublimation or recrystallisation of the crude material and is the most stable form. The β-film can be obtained by heat treatment of the α-film at temperatures below 300°C (68, 81). The α-form can be achieved through acid pasting, sublimation to a film, or heat treatment. The χ-form is formed using milling, whilst the γ, δ and ε forms are also formed by precipitation from concentrated sulphuric acid. The morphology of phthalocyanine films ranges from amorphous to highly crystalline. The phase obtained during vacuum sublimation is dependent upon sublimation conditions (82). Amorphous films are prepared at 10^{-6} torr on to liquid nitrogen cooled substrates. These films are stable at room temperature but crystallise to the α-phase when annealed (60-140°C), followed by an α to β transition at 210°C (68). A substrate held at room temperature gives the α-phase at sublimation pressures less than 50 torr. At higher pressures or substrate temperatures greater than 210°C, the β-phase is formed.

The α-phase consists of microscopic granular crystallites down to 100Å in diameter, whilst the β-phase is formed of large fibrous crystals (70). This morphology difference is important for gas sensing applications, i.e. the α-phase is more sensitive to oxygen (83).

1.6.4 Phthalocyanine Gas Sensors

When electron acceptor gases such as NO_2 interact with solid organic or organometallic compounds with delocalised π-electron systems, charge transfer between the solid and adsorbed gas leads to charge-carrier generation and large increases in electrical conductivity, forming the basis of a sensitive gas sensor (84).

The gases normally detected are NO_2 and chlorine (Cl_2), and much fewer reports exist on the detection of reducing gases (84). Metal phthalocyanines have a high chemical and physical stability and show large conductivity increases which allows NO_2 to be detected in the part per billion (ppb) range. The conductivity change can be slow after a change in NO_2 concentration even when the films are kept at temperatures > 150°C (85). The response rate of NO_2 increases with time because, to adsorb onto a phthalocyanine film in air, NO_2 first displaces adsorbed oxygen from the surface in competition with the excess of oxygen present. Oxygen displacement occurs most easily from the weakest adsorption sites on the surface, but the sticking coefficient will also be small at such sites so the initial rate of adsorption of NO_2 in the presence of competing oxygen will be small. As NO_2 is slowly adsorbed, lateral repulsions with adsorbed oxygen in neighbouring sites increase, resulting in displacement of more strongly bound oxygen at sites where the sticking coefficient for NO_2 will be higher. The rate of uptake of NO_2 therefore increases (86). Part of this effect may be a result of morphological changes occurring during heating of the phthalocyanine films. Surface chemical changes are also involved (85). Reproducible response kinetics for NO_2 sensors based on phthalocyanine films can be obtained if the amount of strongly bound residual adsorbed NO_2 at the start of a sampling pulse is constant (87). The main cause of slow response components are the strong adsorption sites. Heating the film removes some strong adsorption sites leaving a film with a faster response to changes in NO_2 concentration. Some strong adsorption sites do remain after heat treatment, which get involved in the sensing once traces of strongly-bound NO_2 have accumulated on the surface. The onset of the slow component to the response after several hours would cause a drift in the sensor performance. A brief heating to 360°C (2 minutes) drives off the strongly bound NO_2 responsible for the onset of the slow component returning the response to that seen after the initial heat treatment (85).

1.6.4.1 Lead Phthalocyanine Gas Sensors

PbPc's electrical properties give it great sensitivity, stability and conductivity. In an optimized film the NO_2 in the ppb range can be detected (88). The investigation of the effect of NO_2 on the conductance of PbPc has been carried out over the range 100-170°C. These temperatures are low enough for the material to be stable but high enough to eliminate physisorption of water vapour. The conductance of PbPc increases in the presence of NO_2 and the effect is reversible. Long recovery times were experienced at low temperatures. The electrical conductivity change in PbPc at temperatures $\geq$150°C provides selective detection of NO_2 over a wide range of low concentrations in air which include the atmospheric pollution level (30-40 ppb) and the industrial hygiene levels (~5ppm) for NO_2 (40).

Heat pretreatment of PbPc films improves the adsorption process and the recovery time (89). Fast NO_2 detection is obtained even at room temperature using optimized PbPc thin films which have been annealed in air at 300°C or higher (90). Archer and co workers showed the response could be improved by annealing at 150°C in air for several hours (86). These improvements can be attributed to the crystallization of amorphous regions. A film annealed in air at 300°C shows faster response and recovery times for the changes in conductance after step changes from air to NO_2 diluted with air, than for the film annealed at a lower temperature (89).

The surface of the PbPc particles is oxidized by annealing at 300°C in air and the PbPc crystal growth is suppressed by lead oxide forming on the surface. The heat treatment in air of PbPc thin films results in the formation of very fine particles. The oxygen concentration on the surface of these small particles is higher than that of the larger rod-like crystals in which both particles and crystals are formed during the heat-treatment procedure (91). Electron microscopy of thin phthalocyanine films showed that heating induced crystallisation, indicating the faster response of heat treated films could arise from thermally induced structural change (86). The occurrence of reactions between PbPc films and NO_2 depends on the type of surface sites populated by the initially adsorbed gas. Reactions between gases and molecular crystals depends on the particular face on which the gas adsorbs (92). Polycrystalline films present a variety of faces to the adsorbing gas, and there will be a statistical preference for initial population of the weakest (and therefore probably least reactive) sites from which the adsorbed oxygen is not easily displaced (92).

PbPc is not selective to SO_2 or CO individually, but the presence of CO results in a decrease in the conductance response to NO_2 and an increase in the PbPc sensitivity is seen when exposed to SO_2 along with NO_2. One ppm of NO_2 is detectable in a mixture containing 5000ppm of both CO and SO_2 (92).

Metal phthalocyanines mixed with some metal oxides can produce sensors with a low resistivity in air and a high sensitivity for reducing gases at low sensor temperatures.

PbPc mixed with RhO_2 and Pd has a high sensitivity for H_2 gas and a low resistivity in air. These sensors also displayed the properties of an n-type semiconductor to H_2 gas even though pure PbPc is a p-type semiconductor (45).

Multilayer devices using PbPc have also been designed. Aluminum-PbPc-aluminium and palladium-PbPc-aluminium devices have been fabricated. The electrode material can have a significant effect on the PbPc response to gases. These effects are not dependent on the H_2 adsorption/dissociation properties of Pd, although they are probably associated with the catalytic properties of the electrode material. The devices with Pd interdigitated planar electrodes showed gas sensitivity by a decrease in conductance to NO_2 and O_2, and an increase in conductivity was seen with the electron-donor gases NH_3 and H_2. These results implied n-type behaviour of the active material when incorporated in this type of structure. This is contrary to the reported behaviour of PbPc and most phthalocyanines in which p-type behaviour is normal (93).

1.6.4.2 Zinc Phthalocyanine Gas Sensors

The effect of the oxidizing gases O_2 and NO_2 on the p-type semiconductivity of ZnPc films treated in nitrogen at 350°C were examined and the conductance increased in the presence of these gases. The effect was reversible (94).

ZnPc films are sensitive to NO_2 in the range 1-100ppm. The sensitivity was dependent upon the morphology and structure of the active layer. The largest sensitivity came from the β-modification film rich in elongated whiskers (95). The purity of ZnPc has a significant effect on the electrical gas sensing properties. Material that has been entrainer sublimed had the highest conductivity, showed linear behaviour, less drift and hysteresis compared with unpurified ZnPc.

The conductivity of the α and β ZnPc critically depends on the presence of oxygen, and the relative sensitivities of both α and β ZnPc to various gases are modified by the presence of oxygen.

1.6.4.3 Copper Phthalocyanine Gas Sensors

The effects of O_2 (94, 97), NO_2 (94, 97), Cl_2 (96), NH_3, ethanol, and water (98) on CuPc films has been studied. The CuPc films were found to be sensitive to interferences from Cl_2, HCl, H_2S, and NH_3 when monitoring NO_2 (99). Oxygen generally induced a lower conductivity than NO_2 or Cl_2 but was more strongly bound to the phthalocyanine. This meant O_2 was present in the film at the temperatures at which it would be used for NO_2 and Cl_2 sensors, and would occupy some of the adsorption sites on the CuPc surface (96). The displacement of adsorbed oxygen molecules by NO_2 and Cl_2 molecules which are thought to take their place, has been reported as being responsible for long response times (86) such as those seen in CuPc. CuPc films prepared by evaporation were sensitive and fast, responding to 25ppb NO_2 at room temperature. Plasma deposited films were found to be more durable but not as sensitive (100). The deposition conditions of the films affected the morphology. There is a change in crystal morphology and the direction in which the molecules stack becomes highly conductive (101) upon reaction with oxidizing agents. To maximize the change in conductivity caused by NO_2, a film with crystal stacking axes orientated parallel to the measurement direction was thought to be desirable. A substrate temperature of 150°C caused the stacking axes of the crystals to orientate parallel to the substrate surface, which was the conductivity measurement direction (100). Exposure of unpurified CuPc to oxygen increased the p-type conductivity. High electron affinity gases i.e. halogens caused an increase in p-type conductivity of CuPc by many orders of magnitude over the oxygen induced level. This increase was partially reversible at room temperature, but completely reversed by heating in vacuum (102).

An organic-inorganic multilayer device using CuPc and TiO_X was fabricated. This was based on the model where charge carrier photogeneration occurs in the CuPc layers and the TiO_X layers have the function of transportation of electrons-in-plane after charge separation at the interfaces. The multilayers exhibited larger photoconductivity than a single CuPc layer, which was attributed to a greater probability of charge carrier separation through transfer of excited electrons from CuPc to the conduction band of TiO_X (103).

1.6.4.4 Metal Free Phthalocyanine Gas Sensors

The effects of NO_2 (94, 100) and O_2 (94) on the p-type semiconductivity of H_2Pc has been investigated in a similar way to the CuPc films with similar results. The use of H_2Pc as a detector of NO_2 was investigated at concentrations of 1ppb - 20ppm (88). It was also reported that 5ppm H_2S, 40ppm NH_3, 10ppm SO_2, 100ppm H_2, 1% CH_4 and H_2O vapour at 50% relative humidity caused less than 20% change in the resistance. This resistance change was thought to be a surface phenomenon as the effect was the same in films throughout the thickness range (88).

1.7 MÖSSBAUER SPECTROSCOPY USING IRON PHTHALOCYANINE

1.7.1 Definitions

1.7.1.1 High and low spin complexes

Complexes possessing the maximum number of unpaired electrons are called high-spin or spin-free complexes, while those in which the d-electrons are paired as far as possible are referred to as low-spin or spin-paired complexes.

1.7.1.2 Magnetic Moment

For ions in the first transition series the magnetic moment (μ) is given by

$$\mu = \sqrt{(4S\ (S+1) + L\ (L+1))} \qquad (1.1)$$

where

S = total spin quantum number

L = total orbital angular momentum quantum number.

In practice the orbital contribution is often considerably less than the spin contribution, so a further approximation can be written

$$\mu = \sqrt{[4S\ (S+1)]} \qquad (1.2)$$

The absolute value if the spin quantum number $s = \pm \frac{1}{2}$ only and $S = \sum s$, so the number of unpaired electrons in a system is given by $n = 2S$. Substituting S into equation gives

$$\mu = \sqrt{[n\ (n+2)]} \qquad (1.3)$$

This result is known as the spin-only formula (104). The unit of magnetic moment is the Bohr Magneton (B.M.). The Bohr magneton is defined in terms of fundamental constants as (105)

$$1B.M = \frac{eh}{4\pi mc} \qquad (1.4)$$

e = Electronic charge

h = Planck's constant

m = Electron mass

c = Speed of light

1.7.2 Iron Phthalocyanine Mössbauer Studies Found in the Literature

Iron-57 Mössbauer parameters characterise the electronic structure of iron complexes because the isomer shift reflects the electron density at the iron nucleus and the quadrupole splitting relates to the electron distribution among the iron orbitals.

The transmission Mössbauer spectrum of a thin sample of pure FePc consists of one quadrupole doublet of Lorentzian lines. The isomer shift (δ) and quadrupole splitting (Δ) do not characterise FePc as an ionic or covalent complex. The isomer shift value of $\delta = 0.6$mm/s (106) occurs between the higher values characteristic of the high spin, and the lower values characteristic of the low spin ferrous ion. The quadrupole value of $\Delta = 2.6$mm/s is characteristic of high spin ferrous ion (106). It has been established that FePc is a true intermediate spin complex (107) although its magnetic susceptibility of approximately $3.9\mu_B$ is larger than the spin only value of $2.8\mu_B$ (108, 109, 110). The iron ion is situated in or very close to the phthalocyanine plane. To become high spin, it would be necessary to raise the iron completely out of the plane which would weaken the Fe-N bonds so much that high spin FePc is energetically unfavourable (111).

Table 1.1 shows the various Mössbauer parameters for FePc found in the literature. The large quadrupole splitting is indicative of an unsymmetric distribution of electrons in the iron d-orbitals as well as the lack of cubic symmetry (107). The isomer shift and quadrupole splitting of the β-FePc are greater than those of the α-form. In a metal phthalocyanine molecule, the metal atom is at the centre of a square of ligating nitrogens at approximately 1.83Å. In the β-form, there are in addition nitrogen atoms of the neighbouring molecules present in the octahedral positions i.e. above and below the central atom, at 3.38Å (figures 1.9). In the α-form, the nitrogens from the nearest molecules are not in axial positions and therefore do not form the nitrogen octahedron about the central metal atom.

Table 1.1 Mössbauer parameters for FePc found in the literature.

Sample	Temp. (K)	δ mm/s (Fe)	Δ mm/s	Reference
FePc	4.2	0.48	2.70	112
FePc	4.8	0.58	2.70	106
FePc	77	0.44	2.46	113
Monomeric FePc	77	0.31	2.59	114
Polymeric FePc	77	0.49	2.60	111
α-FePc	80	0.46 ± 0.01	2.49 ± 0.01	115
β-FePc	80	0.48 ± 0.01	2.68 ± 0.01	115
FePc	80	0.51 ± 0.02	2.62 ± 0.02	108
FePc	80	0.48 ± 0.02	2.60 ± 0.02	116
FePc	80	0.53 ± 0.02	2.62 ± 0.02	117
FePc	80	0.64	2.64	106
FePc	80	0.48	2.63	118
FePc	81	0.64	2.64	106
FePc	81	0.77	2.71	108
FePc	110	0.46	2.65	119
FePc	293	0.66	2.64	106
FePc	293	0.68	2.67	108
FePc	298	0.39	2.60	119
FePc (pure)	RT	0.40	2.63	120
FePc	RT	0.39	2.58	107

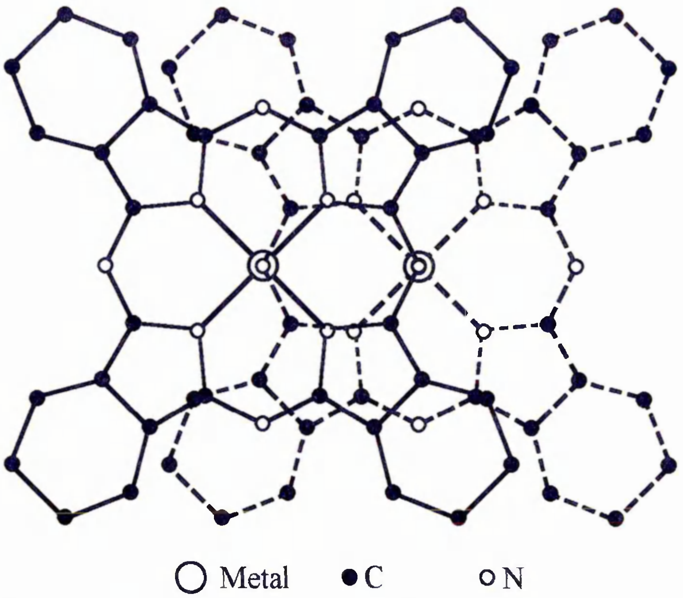

Figure 1.9 Normal projection of two parallel beta molecules. Solid lines outline the upper molecule and the dotted lines the underlying molecule.

The difference in parameters of the α and β-forms can be attributed to intermolecular interactions. The larger chemical shift of β-FePc can be understood by visualising the π-electrons of the aromatic rings of the neighbouring molecules as being delocalised through two axially substituted nitrogens on the $3d_{xy}$ and $3d_{yz}$ orbitals of the central iron atom. This would mean enhanced shielding of the s electrons by d electrons and so decrease the s-electron density on the iron nucleus. This would account for the larger chemical shift of the β-FePc compared to the α-form (115). Measurements on magnetic susceptibility of FePc at very low temperatures has shown that the ground state of the central metal ion is in an $S=1$ state. Figure 1.10 shows a schematic representation of the $3d^6$ electronic configuration of iron (II) in the free ion and a strong-field tetragonal environment (109).

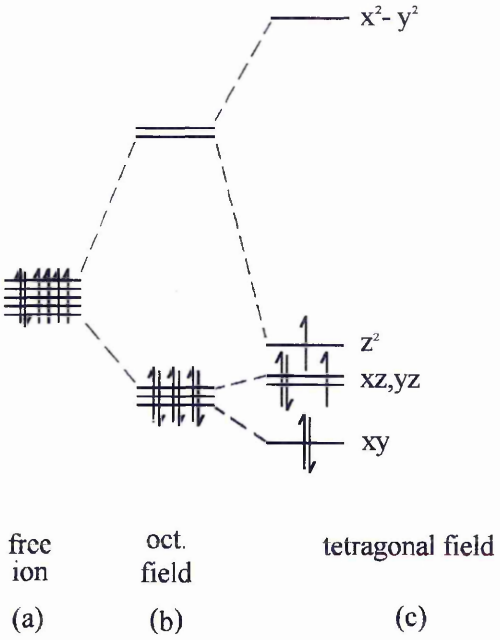

Figure 1.10 A schematic representation of the $3d^6$ electronic configuration of iron (II) in: (a) the free ion (S=2); (b) a strong-field octahedral environment (S=0); (c) a strong-field tetragonal environment (S=1).

Mössbauer spectroscopy has been used to study the effect of pressure on FePc. FePc was prepared using 90% ^{57}Fe enriched iron. The Mössbauer parameters are shown in table 1.2.

Table 1.2 Mössbauer parameters showing the effect of pressure on FePc.

Pressure (Kbar)	δ mm/s (Fe)	Δ mm/s	Reference
0	0.39	2.58	107
25	0.37	2.74	107
50	0.35	2.90	107
75	0.32	3.06	107
100	0.30	3.14	107
125	0.29	3.18	107
150	0.28	3.21	107
175	0.27	3.23	107

The isomer shift (δ) showed a small decrease with increasing pressure indicating an increase in the electron density at the nucleus. The quadrupole split (Δ) showed a large increase with increasing pressure (0.7mm/s in 170Kbar) (107).

Mössbauer spectra of monomeric and polymeric FePc on carbon supports prepared by dissolution-precipitation techniques have been collected. A number of isomer shifts and quadrupole interaction parameters were noted which at high loading (45wt% FePc) appear to be governed by interaction with the solvent and atmospheric oxygen. At low loadings (< 15wt%) a quadrupole doublet ($\delta = 0.32$mm/s, $\Delta = 0.66$mm/s) was observed and thought to be due to the interaction with the carbon substrate (120). The Mössbauer parameters of monomeric and polymeric FePc with and without carbon supports are listed in table 1.3.

Table 1.3 Mössbauer parameters of FePc with and without carbon supports.

Sample	δ mm/s (Fe)	Δ mm/s	Reference
Monomer	0.49	2.60	111
Monomer + carbon	0.26	1.25	111
	0.45	0.63	
	0.48	2.46	
Polymer	0.19	2.95	111
	0.46	2.66	
	0.25	1.97	
	0.48	0.83	
Polymer + carbon	0.35	2.88	111
	0.13	1.95	
	0.44	0.82	

Dispersing FePc on carbon changed the electronic state of the monomer to low spin (S=0) but the polymeric spin remained unchanged (S=1). A suggestion was that bonding between polymeric FePc and carbon took place through the side groups present on the peripheral parts of the polymer and/or through stable chemical groups present on the carbon surface (111).

REFERENCES

1 C. Nylander, *J. Phys. E*, 1985, 18, 736.

2 J. Janata, *Anal. Chem.*, 1992, 64, 196R - 219R.

3 J. Hubble, *J. Chem. Technol. Biotechnol.*, 1986, 36(10), 487.

4 S. Birnbaum, L. Buelow, K. Hardy, B. Danielsson, K. Mosbach, *Anal. Biochem.*, 1986, 58(1), 12.

5 B. Danielsson, *J. Biotechnol.*, 1990, 15(3), 187-200.

6 J. Janata, *Anal.Chem.*, 1992, 64, 196R - 219R.

7 H. Schopf, P. Wurfel, W. Ruppel, *Sens. Mater.*, 1991, 3(1), 25 - 40.

8 W. H. King, *Anal. Chem.*, 1964, 36, 1735 -1739.

9 H. Wohltjen, R. Dessy, *Anal. Chem.*, 1979, 51, 1458 - 1478.

10 M. Nieuwenhuizen, A. Nederlof, A. Barendsz, *Anal. Chem.*, 1988, 60, 230 - 235.

11 M. Nieuwenhuizen, A. Nederlof, *Anal. Chem.*, 1988, 60, 236 - 240.

12 J. Attridge, K. Lever, J. Cozens, *J. Phys. E: Sci. Instrum.*, 1987, 20(5), 548.

13 J. Fouletier, E. Siebert, *Ion-Selective Electrode Rev.*, 1986, 8, 133-151.

14 T. Seiyama, K. Kato, K. Fujishi, M. Nagatani, *Anal. Chem.*, 1962, 341, 1502-1503.

15 U. Dibbern, *Sens. Actuators B*, 1990, 2, 63-70.

16 I. Stoev, D. Kohl, *Sens. Actuators B*, 1990, 2, 233-236.

17 A. Cranny, J. Atkinson, *Inst. Phys. Conf. Ser. N^o 1*, paper presented at Int. Conf. on New Materials and Their Applications, Univ. Wawick, 1990, 345-354.

18 P. Van Geloven, J. Moons, M. Honore, J. Ruggen, *Silicates Industrial*, 1990, 3-4, 81-85.

19 J. McAleer, P. Moseley, J. Norris, D. Williams, P. Taylor, *Materials Chemistry and Physics*, 1987, 17, 577-583.

20 P. Romppainen, H. Torvela, J. Vaananen, S. Leppavuori, *Sens. Actuators*, 1985, 8, 271-279.

21 J. Gutierrez, F.Cebollada, C. Elvira, E. Millan, J. Agapito, *Materials Chemistry and Physics*, 1987, 18, 265-275.

22 C. Xu, J. Tamaki, N. Miura, N. Yamazoe, *Denki Kagaku*, 1990, 58, 1143-1148.

23 G. Sberveglieri, S. Groppelli, P. Nelli, *J. Mater. Sci. Lett.*, 1991, 10, 602-604.

24 G. Coles, G. Williams, B. Smith, *Sens. Actuators B*, 1991, 3, 7-14.

25 G. Coles, G. Williams, B. Smith, *J. Phys. D: Appl. Phys.*, 1991, 24, 633-641.

26 S. Semancik, D. Cox, *Sens. Actuators*, 1987, 12, 101-106.

27 N. Yamazoe, J. Fuchigami, M. Kishikawa, T. Seiyama, *Surface Science*, 1979, 86, 335-344.

28 Y. Nakatani, M. Matsuoka, *Jpn. J. Appl. Phys.*, 1982, 21, L758-L760.

29 Y. Nakatani, M. Matsuoka, *Jpn. J. Appl. Phys.*, 1983, 22, 233-239.

30 Y. Nakatani, M. Sakai, M. Matsuoka, *Proc. Int. Meet. on Chem. Sensors*, Fukova, Tokyo, 1983.

31 D. Guorui, C. Lihua, Y. Bailiang, L. Mingdeng, *Journal de Physique 2*, 1991, 1, C2, 233-239.

32 H. Takenaka, *New Materials and New Processes*, 1985, 3, 372-375.

33 M. Fujinami, Y. Ujihira, *J. Mater. Sci.*, 1985, 20, 1859-1863.

34 W. Chung, D. Lee, *Thin Solid Films*, 1991, 200, 329-339.

35 C. Cantalini presented at *Eurosensor V*, Rome, October 1991.

36 S. Morrison, *Sens. Actuators*, 1987, 12, 425-440.

37 Y. Nakatani, M. Sakai, M. Matsuoka, *Jpn. J. Appl. Phys.*, 1983, 22, 912-916.

38 N .Yamazoe Y. Kurokawa, T. Seiyama, *Chem. letts.*, 1982, 1899-1902.

39 P. Thomas, *Physics World*, 1993, 31.

40 B. Bott, T. Jones, *Sens. Actuators*, 1984, 5, 43-53.

41 J. Bornmann, *J. Chem. Phys.*, 1957, 27, 604-605.

42 R. Collins, K. Mohammed, *Thin Solid Films,* 1986, 145, 133-145.

43 Y. Sadaoka, T. Jones, W. Gopel, *J. Mater. Phys. Letts.*, 1989, 8, 1095-1097.

44 A. Wilson, G. Rigby, J. Wright, S. Thorpe, T. Terui, Y. Maruyama, *J. Mater. Chem.*, 1992, 2, 303-308.

45 S. Kanefusa, M. Nitta, *Sens. Actuators B*, 1992, 9, 85-90.

46 E. Orti, J. Brédas, *J. Am. Chem. Soc.*, 1992, 114, 8669-8675.

47 A. Brown, J. Tcherniac, *J. Ber. Dtsch. Chem. Ges.*, 1907, 40, 2709.

48 R. Linstead, A. Lowe, *J. Chem. Soc.*, 1934, 1016.

49 C. Dent, R. Linstead, *J. Chem. Soc.*, 1934, 1027.

50 D. Grenoble, H. Drickamer, *J. Chem. Phys.*, 1971, 55, 1624-1633.

51 M. Robinson, G. Klein, *J. Am. Chem. Soc.*, 1965, 74, 6294-6295.

52 C. Brown, *J. Chem. Soc.(A)*, 1968, 2488-2493.

53 J. Assour, *J. Am. Chem. Soc.*, 1965, 4701-4706.

54 M. Friedel, B. Hoskins, R. Martin, S. Mason, *Chemical Communications,* 1970, 400-401.

55 J. Kirner, W. Dow, W. Scheidt, *Inorg. Chem.*, 1976, 15, 1685-1690.

56 R. Linstead, J. Robertson, *J. Chem. Soc.,* 1936, 1736.

57 K. Law, *Chem. Rev.*, 1993, 93, 449-486.

58 A. Lever in *Adv. Inorg. Chem. Radiochem.*, Ed. H. Emeléus, A. Sharpe, Academic Press, New York and London, Vol 7, pg 27 - 114.

59 R. Moser, A. Thomas, *The Phthalocyanines,* CRC Press, Boca Raton, FL, 1983, Vols 1 and 2.

60 J. Sounik, L. Schechtman, B. Rinter, W. Ford, M. Rogers, M. Kenney, *Proc. Spie.*

(Int. Soc. Opt. Eng.) 1990, Vol 1203, *(Proc. Photodyn. Ther: Mech.* 2 1990) 224 - 232.

61 M. Hanack, A. Gul, A. Hirsch, B. Mandal, L. Subramanian, E. Wilke, *Mol. Cryst. Liq. Cryst.*, 1990, 187, 365 - 382.

62 J. Assour, M. Harrison, *J. Am. Chem. Soc.*, 1965, 651 - 652.

63 D. Grenoble, H. Drickamer, *J. Chem. Phys.*, 1971, 55, 1624 - 1633.

64 F. Iwatsu, T. Kobayashi, N. Uyeda, *J. Phys. Chem.*, 1980, 84, 3223 - 3230.

65 M. Whalley, *J. Chem. Soc.*, 1936, 1719.

66 J. Sharp, M. Lardon, *J. Phys. Chem.*, 1968, 72, 3230 -3235.

67 L. Lyons, J. Walsh, J. White, *J. Chem. Soc.,* 1960, 167 - 175.

68 S. Harrison, K. Ludewig, *J. Chem. Phys.*, 1966, 45, 343 -348.

69 R. Sappok, J. *Oil Colour Chem. Assoc.* 1978, 61, 299.

70 M. Ashida, N. Uyeda, E. Suito, *J. Cryst. Growth*, 1971, 8, 45 -56.

71 J. Beynon, A. Humphries, *Trans. Faraday Soc.*, 1955, 51, 1065 - 1071.

72 A. Erbert, H. Gottlieb, *J. Am. Chem. Soc.*, 1952, 74, 2806 - 2810.

73 R. Collins, A. Belghachi, *Materials Letters,* 1989, 8, 349 -352.

74 K. Ukei, *Acta. Cryst.,* 1973, B29, 2290 - 2292.

75 Y. Iyechika, K. Yakushi, I. Ikenoto, H. Kuroda, *Acta. Cryst.*, 1982, B38, 766 - 770.

76 T. Kobayashi, N. Uyeda, E. Suito, *J. Chem. Phys.*, 1968, 72, 2446 - 2456.

77 T. Kobayashi, Y. Fujiyoshi, F. Iwatsu, N. Uyeda, *Acta. Cryst.*, 1981, A37, 692 - 697.

78 F. Iwatsu, T. Kobayashi, N. Uyeda, *J. Phys. Chem.*, 1980, 84, 32.

79 T. Srivastava, J. Przybylinski, A. Nath, *Inorg. Chem.*, 1974, 13, 1526 - 1564.

80 J. Silver, P. Lukes, A. Houlton, S. Howe, P. Hey, M. Ahmet, *J. Mater. Chem.*, 1992, 2, 849 - 855.

81 A. Sidorov, *Opt. Spectry*. 1961, 11, 92.

82 M. Mindorff, D. Brodie, *Can. J. Phys.*, 1981, 59, 249-254.

83 Y. Sadaoka, *Denki. Kagaku*, 1978, 46, 597.

84 J. Wright, *Progress in Surface Science*, 1989, 31, 1-60.

85 A. Wilson, J.Wright, *Mol. Cryst. liq. Cryst.*, 1992, 211, 321-326.

86 P. Archer, A. Chadwick, J. Miasik, M. Tamizi, J. Wright, *Sens Actuators*, 1989, 16, 379.

87 A. Wilson, J. Wright, A. Chadwick, *Sens. Actuators B*, 1991, 499-504.

88 T. Jones, B. Bott, S. Thorpe, *Sens Actuators*, 1989,17,467.

89 Y. Sadaoka, M. Matsuguchi, Y. Sadai, Y. Mori, *J. Mater. Sci. Letts.*, 1992, 27, 5215-5220.

90 Y. Sadaoka, T. Jones, W. Gopel, *Sens Actuators B*, 1990, 1, 148.

91 Y. Sadaoka, W. Gopel, B. Suhr, A. Rager, *J. Mater. Sci.*, 1990, 9, 1481-1483.

92 A. Heilmann, M. Müller, C. Hamann, V. Lantto, H. Tovela, *Sens Actuators* B, 1991, 4, 511-513.

93 W.Ruihua, T. Jones, *Sens Actuators B*, 1990, 12, 33-42.

94 Y. Sadaoka, Y. Sakai, T. Jones, W. Gopel, *J. Mater. Sci.*, 1990, 25, 3024-3028.

95 S. Pizzini, G. Timo, M. Beghi, N. Butta, C. Mari, J. Faltenmaier, *Sens. Actuators,* 1989, 17, 481-491.

96 S. Dogo, J. Germain, C. Maleysson, A. Pauly, *Sens. Actuators B,* 1992, 8, 257-259.

97 R. Weaver, J. Wright, *Sens Actuators B*, 1991, 4, 505-510.

98 W. Barger, H. Wohltjen, A. Snow, J. Lint, N. Jarvis, *Fundamentals and Applications of Chemical Sensors*, American Chemical Society, 1986, pg.155-165.

99 C. Honeybourne, R. Ewen, C. Hill, *J. Chem. Soc. Faraday Trans.* 1, 1984, 80, 851-863.

100 K. Schoch, T. Temofonte, R. Sadher, J. Greggi, Z. Sanjana, *Synthetic Metals*, 1989, 29, F89-F94.

101 B. Diel, T. Inabe, J. Lyding, K. Schoch, C. Kannewurf, T. Marks, *J. Am. Chem. Soc.*, 1983, 105, 1551.

102 H. Laurs, G. Heiland, *Thin Solid Films*, 1987, 149, 129-142.

103 J. Takada, H. Awaji, M. Koshioka, A. Nakajima, W. Nevin, Appl. *Phys, Lett.*, 1992, 61, 2184-2186.

104 D. Nicholls, *Complexes and First Row Transition Elements*, Macmillan, Hampshire and London, 1990.

105 F. Cotton, G. Wilkingson, *Advanced Inorganic Chemistry: A Comprehensive Text*, Wiley, New York, 1972.

106 I. Dézsi, A. Balázs, B. Molnar, V. Gorobchenko, I. Lukashench, *J. Inorg. Nucl. Chem.*, 1969, 31, 1661 - 1666.

107 D. Grenoble, H. Drickamer, *J. Chem. Phys.*, 1971, 55, 1624 - 1633.

108 A. Hudson, H. Whitfield, *Inorg. Chem.*, 1967, 6, 1120.

109 B. Dale, R. Williams, C. Johnson, T. Thorp, *J. Chem. Phys.*, 1968, 49, 3441 - 3444.

110 A. Lever, *J. Chem. Soc.*, 1965, 1821 - 1829.

111 J. Blomquist, L. Moberg, *J. Inorg. Nucl.Chem.*, 1981, 43, 2287.

112 T. Ohya, N. Kobatashi, M. Sato, *Inorg. Chem.*, 1987, 26, 2506 - 2509.

113 J. Silver, P. Lukes, A. Houlton, S. Howe, P. Hey, M. Ahmet, *J. Mater. Chem.*, 1992, 2, 849 - 855.

114 J. Blomquist, L. Moberg, *Inorg. Chim. Acta.*, 1981, 53, L39 - 40.

115 T. Strivastava, J. Przybylinski, A. Nath, *Inorg. Chem.*, 1974, 13, 1562 - 1564.

116 R. Taube, H. Drevs, E. Fluck, P.Kuhn, K. F. Brauch, *Z. Anorg. Allg. Chem.*, 1969,

364, 297.

117 T. Moss, A. Robinson, *Inorg. Chem.*,1968, 7, 1692.

118 J. Thompson, J. Ching, E. Fung, *Radiochim. Acta.*, 1972,18, 57.

119 C. Frampton, J. Silver, *Inorg. Chim. Acta.*, 1985, 96, 187 - 191.

120 C. Melendres, *J. Phys. Chem.*, 1980, 84, 1936 - 1939.

CHAPTER TWO

MÖSSBAUER SPECTROSCOPY

2 INTRODUCTION

2.1 THE MÖSSBAUER EFFECT

The Mössbauer effect was discovered in 1957 by Rudolph Mössbauer for which he was later awarded the Nobel prize in 1961. The Mössbauer effect had been foreseen by Lambe in 1939 who described the capture of neutrons by atoms in a crystal (1) and Dicke in 1953 who explained the effect of collisions upon the Doppler width of spectral absorption or emission lines (2). The Mössbauer effect is the process of emitting or absorbing a gamma ray photon without energy loss due to recoil of the nucleus and without thermal broadening. Monochromatic electromagnetic radiation, with a narrowly defined energy spectrum, can thus be detected, and hence can be used to resolve minute energy differences. The Mössbauer effect can detect small variations in the energy of interaction between the nucleus and the extra-nuclear electrons, and hence has a direct application to chemistry (3).

The discovery of the Mössbauer effect in iron-57 had an important effect on the technique. Previous work had been carried out at liquid helium temperatures with iridium-191, which was not necessary with Fe-57 and so the effect was easier to observe. A large amount of information about the magnetic and electronic properties of the iron atom was obtainable and the range of applications was extended when found in tin-119 (4).

2.1.1 Nuclear Resonance Fluorescence

A photon of energy is emitted when a nucleus decays from a high energy to a low energy state, and is absorbed upon transition from a low energy to a higher energy state. The energy difference between two such states is equivalent to that of the emitted or absorbed photon. In nuclear cases the absorption is referred to as nuclear resonance absorption and the photon needs precisely the right energy to create a transition from ground state to an excited state. The absorbed or emitted energy in the form of electromagnetic radiation obeys the relationship given in equation 2.1

$$\Delta E = h\nu \tag{2.1}$$

ΔE = Absorbed or emitted energy

h = Planck's constant

υ = Frequency of radiation.

2.1.2 Recoil Energy and Resonance Absorption

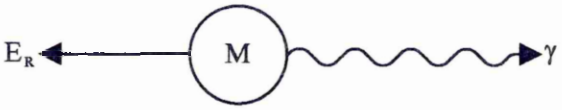

Figure 2.1 Schematic diagram of nucleus recoil.

A nucleus of mass M with transition energy E_o available to it, experiences a recoil energy E_R, upon emission of a γ-ray with energy E_{γ}. According to conservation of energy:-

$$E_o = E_\gamma + E_R \tag{2.2}$$

Assuming the mass was initially at rest, it has a velocity V_R, upon emission of the γ-ray, given by:

$$E = \frac{MV_R^2}{2} = \frac{(MV_R)^2}{2M} = \frac{P_n^2}{2M} \tag{2.3}$$

where P_n = Momentum of the nucleus.

The law of conservation of momentum means that the momentum of the emitted γ-ray and the momentum gained by the recoiling mass are of equal magnitude and opposite sign.

$$P_{nucleus} = -P_{\gamma-ray} = -\frac{E_\gamma}{c} \tag{2.4}$$

The situation can be treated in a non-relativistic way since the recoils are small ($E_R \ll Mc^2$).

Conservation of momentum means

$$E_R = \frac{P_\gamma^2}{2M} = \frac{E_\gamma^2}{2Mc^2} \tag{2.5}$$

Since $E_R \ll E_o$ we may assume $E_\gamma \approx E_o$, and hence

$$E_R \approx \frac{E_o^2}{2Mc^2} \tag{2.6}$$

The same effect can be considered for absorption when the absorbing nuclei recoils conserving momentum. Figure 2.2 shows the emission and absorption transitions of a γ-ray.

The presence of recoil in nuclear systems means that the emission and absorption spectra are not identical, and since the energy difference ($2E_R$) is likely to be large there will usually be no overlap and hence no resonance.

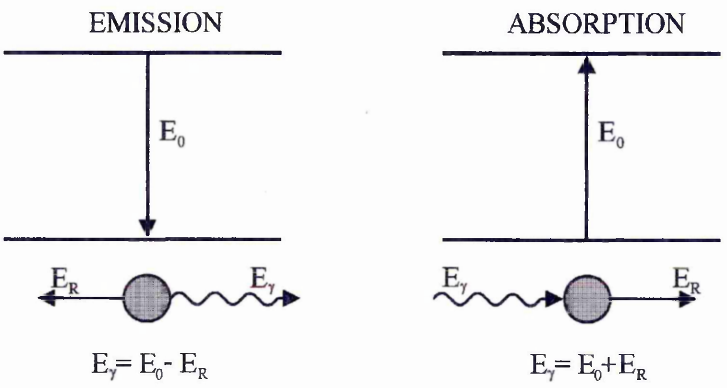

Figure 2.2 Emission and absorption transitions of a γ-ray.

Energies in the region of 10KeV give significant recoil energies and there is little overlap between the energy profiles (figure 2.3). High temperatures were used in an attempt to increase the amount of overlap due to Doppler broadening created by random thermal velocities of the source and absorber nuclei.

The Doppler broadening E_D can be written (3) as

$$E_D = 2\sqrt{E_R kT} \qquad (2.7)$$

T = Temperature

k = Boltzmann constant

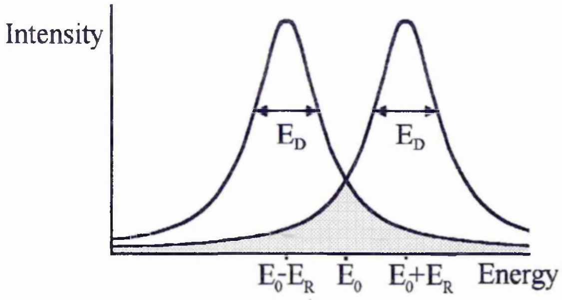

Figure 2.3 The effect of recoil on the nuclear emission and absorption spectrum.

Doppler broadening increases the line overlap and so the amount of absorption, but at the expense of a decrease in the resolution.

The Doppler broadening is proportional to the square root of the recoil energy, hence zero recoil would mean no Doppler broadening, resulting in good resolution i.e. the natural line width.

2.1.3 The Recoil Free Fraction and Recoil Free Emission

Mössbauer found that the resonant absorption of a sample containing ^{191}Ir suddenly increased at low temperatures. Equation 2.7 would appear to contradict this as E_D decreases as the temperature decreases, hence less overlap of source and absorber energy profiles. Mössbauer postulated that a proportion of gamma rays were emitted with zero recoil.

In order to understand this, consider the following. An excited nucleus is rigidly held in a solid. Upon gamma ray emission the emitting atom cannot move (recoil/eject) from its lattice position since E_R is much smaller than the chemical binding energy. Hence the mass of the whole crystal becomes the recoiling mass and is large. E_R is now much smaller than the Heisenberg line width (Γ_H). The atom cannot experience random thermal motion hence the Doppler broadening E_D becomes negligible in comparison to

Γ_H. So for a rigidly bound atom $E_o \approx E_\gamma$, and source and absorber profiles overlap and have widths near Γ_H.

However, generally the emitting atom is free to vibrate, and the recoil energy could be transferred into excitation of lattice vibrations since these energies are similar to E_R. The Einstein model of a quantised lattice shows specific energies ±hυ, ±2hυ, ±3hυ, etc are necessary to excite the lattice to its lowest excited level.

If E_R is less than this minimum quantum of energy then the emitting atom effectively does not experience recoil and the whole mass takes up the recoil, E_R and E_D become very small and $E_o \approx E_\gamma$ resulting in resonance being easily observed (6).

As mentioned the lattice excitation energies and E_R are of similar magnitude so only a certain fraction (f) of emissions and absorptions take place without recoil. The value of f varies from solid to solid and decreases as E_γ (and hence E_R) increases. The Mössbauer recoil free fraction (f) is expressed as:

$$f = \exp\left[\frac{-4\pi^2\langle X^2\rangle}{\lambda^2}\right] \tag{2.8}$$

λ = Wavelength of gamma photon

$\langle X^2\rangle$ = Mean square vibrational amplitude of the emitting (or absorbing) nucleus in the solid.

2.1.4 Mössbauer Line Width

The energies of emitted gamma rays are not identical. There is a range of energies about a mean with the emitted line having a natural breadth. The Briet Wigner equation gives the intensity distribution (7).

$$I(E)=\frac{f_s\Gamma}{2\pi}\frac{1}{(E-E_o)+(\Gamma/2)^2} \qquad (2.9)$$

I (E) = Intensity of distribution of energy E

f_s = Probability of recoil-free emission from the source

E_o = Transition energy

Γ = Natural line width

The Breit Wigner equation describes a Lorentzian line shape (figure 2.4).

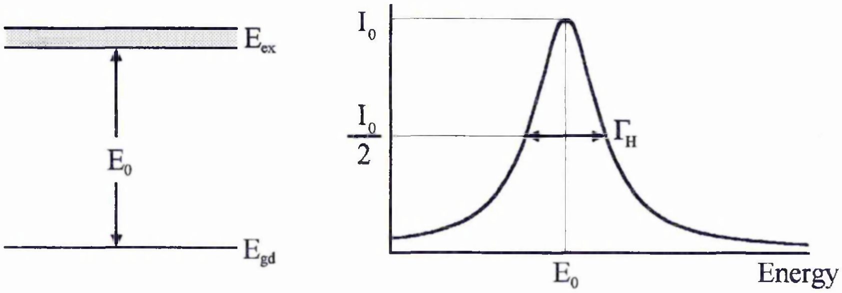

Figure 2.4 The Lorenzian distribution of emitted γ-rays.

For the ground state, the mean lifetime is infinite and the state is sharp ie $\Delta E \rightarrow O$. The full width at half height Γ_H governs the resolution of the Mössbauer experiment and is determined by the mean life τ of the nuclear state,

$$\tau=\frac{t_{1/2}}{0.693} \qquad (2.10)$$

and the Heisenberg uncertainty principle.

$$\Gamma_H\tau=\frac{h}{2\pi}=\hbar \qquad (2.11)$$

h = Planck's constant (6.626 × 10^{-34} Joule-second)

Solving for Γ_H we have

$$\Gamma_H \tau = \frac{6.626\times10^{-34}}{2\pi} = 1.055\times10^{-34} JS \tag{2.12}$$

remembering 1 Joule = 6.24 × 10^{18}eV

$$\Gamma_H = \frac{1.055\times10^{-34}\times6.24\times10^{18}}{\tau} = \frac{6.58\times10^{-16}eV}{\tau} \tag{2.13}$$

or

$$\Gamma_H = \frac{6.58\times10^{-16}\times0.693}{t_{½}} = \frac{4.56\times10^{-16}eV}{t_{½}} \tag{2.14}$$

Considering ^{57}Fe which has a $t_{½} = 97.7 \times 10^{-9}$s and a transition energy of 14.4×10^{3}eV. The line width Γ_H is 4.67×10^{-9}eV which is infinite compared to the transition energy. The resolution is shown by:

$$\frac{\Delta E}{E} = \frac{\Gamma_H}{E} = \frac{4.67\times10^{-9}eV}{14.4\times10^{3}eV} = 3.24\times10^{-13} \tag{2.15}$$

Thus a resolution of 1 part in 10^{13} is possible.

2.1.5 The Doppler Effect and the Mössbauer Spectrum

Minimising the recoil energy loss and Doppler broadening does not result in resonant absorption. Exact overlap of emission and absorption profiles is necessary. This coincidence does not usually occur because of energy differences between the source and absorber. In Mössbauer spectroscopy the source is mounted on a vibrator moving back and forth with respect to the absorber resulting in a range of energies due to the Doppler effect.

The Doppler effect is the phenomenon by which apparent sound or electromagnetic frequencies are changed by the motion of the emitter (source) relative to the observer (absorber).

$$\Delta E = \left[\frac{V}{c}\right] E_\gamma \tag{2.16}$$

Consider a photon source with energy E_γ and velocity V moving directly toward the observer. A change of energy ΔE_S results as seen by the observer. Using the 14.4KeV ^{57}Fe gamma ray as an example:- If this source moves with a velocity 1cm/s then from equation 2.16

$$\Delta E = \frac{1cm/s \times 14.4 \times 10^3 eV}{3 \times 10^{10} cm/s} = 4.80 \times 10^{-7} eV \tag{2.17}$$

The energy 4.8×10^{-7}eV is minute compared with E_γ (14.4×10^3eV) but two orders of magnitude larger than Γ_H derived earlier (4.67×10^{-9}eV). This shows that production of large changes in the gamma ray energy (w.r.t Γ_H) using small velocities is possible. For a recoiless emission of transition energy E_o the γ-ray energy E_γ can be modified by the Doppler velocity V as follows:

$$E_\gamma = E_o \left[\frac{E_o V}{c}\right] \tag{2.18}$$

Scanning a range of velocities results in energies coinciding at a particular velocity and resonance is at a maximum. Absorption decreases, at any higher or lower velocities, to effectively zero.

The conventional Mössbauer spectrum (figure 2.5) is a plot of absorption verses a series of relative Doppler velocities between the moving source and stationary absorber.

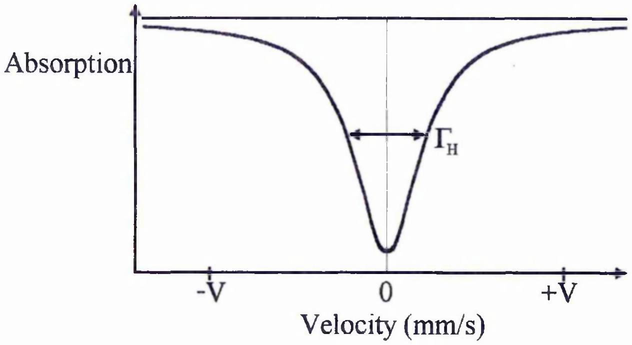

Figure 2.5 Conventional Mössbauer spectrum.

2.2 THE HYPERFINE INTERACTIONS

Different compounds give rise to different Mössbauer spectra, since the peak positions in a Mössbauer spectrum are sensitive to the extranuclear environment. The Mössbauer effect detects electronic changes caused by for example chemical bonding or magnetic impurities. The changes are attributed to interactions between the nuclear charge distribution and the electric and magnetic fields.

There are three hyperfine interactions:

(i) The Electric Monopole Interaction

(ii) The Electric Quadrupole Interaction

(iii) The Magnetic Interaction

Each of these will be considered separately.

2.2.1 The Isomer Shift

An atomic nucleus occupies a finite volume and s-electrons can penetrate the nucleus spending time in the nuclear region. Electrostatic interaction occurs between the nuclear charge and the s-electron charge cloud in the nucleus, resulting in a slight shift in the nuclear energy level of δE, (figure 2.6).

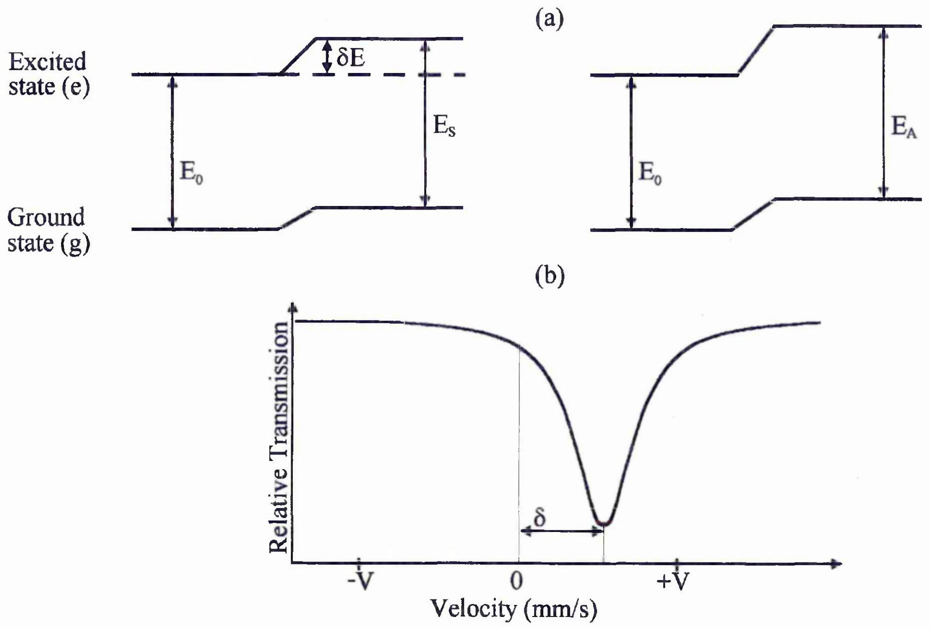

Figure 2.6 (a) and (b). Origin of isomer shift.

(a) Electric monopole interaction shifts nuclear energy levels without lifting the degeneracy.

(b) Resultant Mössbauer spectrum (schematic).

The energy shift can be calculated assuming the nucleus to be a uniformly charged sphere of radius R and the electron cloud to be uniformly distributed over the nuclear range. The energy difference between the coulombic (electrostatic) interaction of a (hypothetical) point nucleus and one of actual radius R, possessing the same charge Ze is represented by δE.

$$V_P(r) = \frac{Ze}{r} \tag{2.19}$$

where $0 \leq r \leq \infty$

$V_p(r)$ = Electrostatic potential of point-charge nucleus at a distance r

$$V_f(r) = \frac{Ze}{R}\left[\frac{3}{2} - \frac{r^2}{2R^2}\right] \quad \text{for } r \leq R \qquad (2.20)$$

$$V_f(r) = \frac{Ze}{R} \qquad \text{for } r \geq R \qquad (2.21)$$

$V_f(r)$ = Electrostatic potential of a nucleus of finite size ρ_{el}

The energy difference δE is given by :-

$$\delta E = \int_{\infty}^{0} \rho_{el}(V_f - V_p) 4\pi r^2 \delta r \qquad (2.22)$$

where

$4\pi r^2$ = Surface area

$4\pi r^2 dr$ = Elemental volume

$4\pi r^2 dr\rho$ = Change in elemental volume

$V4\pi r^2 dr\rho$ = Electrostatic energy

Therefore

$$\delta E = \frac{4\pi\rho Ze}{R}\int_0^R \left(\frac{3}{2} - \frac{r^2}{2R^2} - \frac{R}{r}\right) r^2 dr \qquad (2.23)$$

$$\delta E = -\left(\frac{2\pi}{5}\right) Ze\rho R^2 \qquad (2.24)$$

$$\delta E = -\left(\frac{2\pi}{5}\right) Ze^2 |\Psi(0)|^2 R^2 \qquad (2.25)$$

Equation 2.24 is derived from 2.23 because the electrostatic potential of a nucleus of finite size ρ is the electron density at the nucleus, which can be expressed in terms of the electron wave function Ψ by $-e|\Psi(0)|^2$.

The nuclear volume will be different in each state of excitation, and so the electrostatic shift δE will be different in each nuclear state. Thus, in a transition of a nucleus between its ground state and an excited state the energy change of a gamma ray due to this "volume effect" will be, relative to a point-charge nucleus:

$$\Delta E=(\delta E)_e-(\delta E)_g=\left(\frac{2\pi}{5}\right)Ze^2|\Psi(0)|^2(R_e^2-R_g^2) \tag{2.26}$$

In the Mössbauer experiment, a Doppler velocity is applied to either source (S) or absorber (A) so that the emitted gamma ray and absorption energy are coincident. The absorber and source material generally differ in chemical and/or physical properties hence the electron density at the nucleus in the source will have a different value to that of the absorber. From equation 2.26 the difference in the electrostatic shift between the source and absorber becomes

$$\delta=\Delta E_A-\Delta E_S=(E_A-E_o)-(E_S-E_o)=E_A-E_S=\left(\frac{2\pi}{5}\right)Ze^2(R_e^2-R_g^2)\left[|\Psi(0)|_A^2-|\Psi(0)|_S^2\right] \tag{2.27}$$

2.27 is usually written as

$$\delta=\left(\frac{4\pi}{5}\right)Ze^2R^2(\delta R/R)\left[|\Psi(0)|_A^2-|\Psi(0)|_S^2\right] \tag{2.28}$$

The isomer shift data must be reported with respect to a standard material because Mössbauer spectra of one compound measured using different sources (i.e. ^{57}Co in Pb, Pt, Cr etc.) show different isomer shifts because the s-electron density ($|\Psi(0)|_S^2$) changes with the chemical environment of the Mössbauer nuclide. The common standard reference materials in ^{57}Fe spectroscopy are metallic iron and sodium nitroprusside dihydrate $Na_2[Fe(CN)_5NO] \cdot 2H_2O$ (SNP).

The electron density at the nucleus is mainly due to s-electrons. Chemical bonding does not have a great affect on the inner orbitals and hence changes in the isomer shift mainly depends upon the outermost occupied s-electron shell. The isomer shift can be affected by the 'p' or 'd' electron density as a result of shielding effects which cause rearrangement of the spatial distribution of the s-electrons hence changing the electron density at the nucleus. If the number of d-electrons decreases then there is an increase in the s-electron density at the nucleus for iron. This results in a decrease in the isomer shift. Hence Fe(II) (d^6) has a larger isomer shift than Fe(III) (d^5). The nuclear radius of the ground state R_g is larger than that of the excited state R_e in iron, hence $R_e^2 - R_g^2$ is negative. [The reverse is true for ^{119}Sn where $R_e^2 - R_g^2$ is positive and the isomer shift is more positive with an increase in the s-electron density].

2.2.2 The Quadrupole Splitting

The model for the isomer shift assumed a spherical nucleus and symmetrical charge distribution. However if the nucleus is not spherical and has a spin (I) greater than ½ (only nuclei with I=0 or ½ are spherically symmetric) there is an interaction between the nuclear quadrupole moment Q, and the electric field gradient (EFG). Q reflects the deviation of the nucleus from spherical symmetry (figure 2.7).

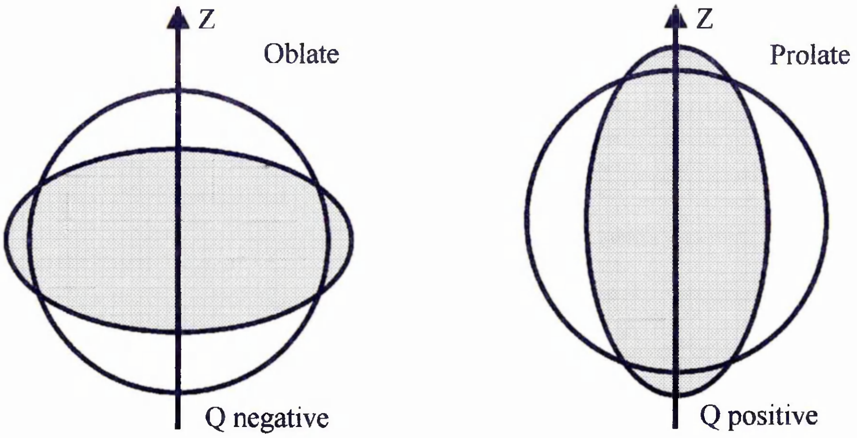

Figure 2.7 Deviation of the nucleus from spherical symmetry.

The ground state of iron-57 has a spin $I_g = {}^1/_2$ and in the excited state $I_e = {}^3/_2$. As already mentioned $I_g = {}^1/_2$ results in a spherical nucleus whilst the excited state $I_e = {}^3/_2$ will have an oblate or prolate (Figure 2.7) shape and therefore a negative or positive quadrupole moment, which will interact with the electric field gradient. The energy change resulting from this quadrupole interaction is given below (3).

$$E_Q = \frac{e^2qQ}{4I(2I-1)}\left[3m_I^2 - I(I+1)\right]\left[1+\frac{\eta^2}{3}\right]^{1/2} \tag{2.29}$$

Where

eq = V_{zz} = Maximum value of the electric field gradient

Q = Nuclear quadrupole moment

e^2qQ = Quadrupole coupling constant

I = Spin state of level

m_I = Magnetic quantum number

η = Asymmetry parameter

The presence of the magnetic quantum number m_I in this equation results in partial removal of degeneracy of the level. States differing in sign only (i.e. not value) do not split but remain degenerate.

Consider the case of Fe-57, assume the nucleus is in an environment where eq and η are finite (non-zero EFG).

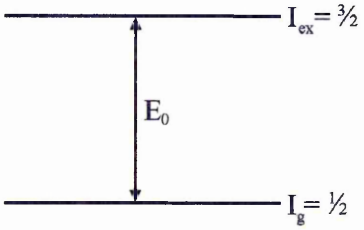

$$K = e^2qQ\left[1 + \frac{\eta^2}{3}\right]^{1/2} \tag{2.30}$$

If $\eta = 0$ then $K = e^2qQ$.

So for $I = {}^1/_2$, $E_Q = 0$.

$$E_Q(m_I) = \left[\frac{K(3m_I^2 - I(I+1))}{4I(2I-1)}\right] \tag{2.31}$$

For $I = {}^3/_2$

$$E_Q(m_I) = \left[\frac{K(3m_I^2 - 15/4)}{12}\right] \tag{2.32}$$

$$E_Q(\pm 1/2) = \left[\frac{K(3/4 - 15/4)}{12}\right] = -\frac{K}{4} \tag{2.33}$$

$$E_Q(\pm 3/2) = \left[\frac{K(27/4 - 15/4)}{12}\right] = +\frac{K}{4} \tag{2.34}$$

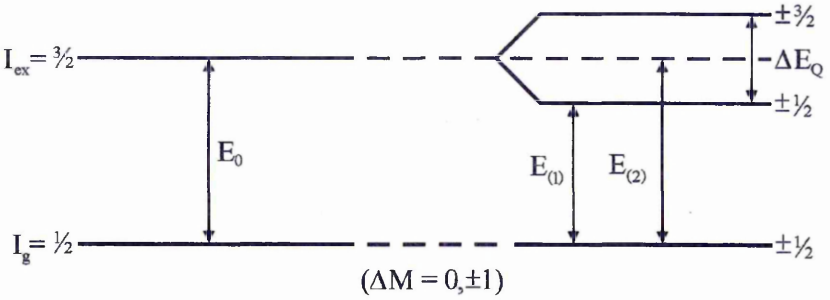

Figure 2.9 Quadrupole splitting in an I = 3/2 → 1/2 transition.

In this case there are symmetrical splittings of levels for I = $^3/_2$. The quadrupole splitting ΔE_Q, is as follows:

$$\Delta E_Q = E_Q(\pm 3/2) - E_Q(\pm 1/2) \tag{2.35}$$

$$\Delta E_Q = \frac{K}{2} = \frac{e^2 qQ}{2} \tag{2.36}$$

The Mössbauer spectrum for this case would look like the one shown in figure 2.10.

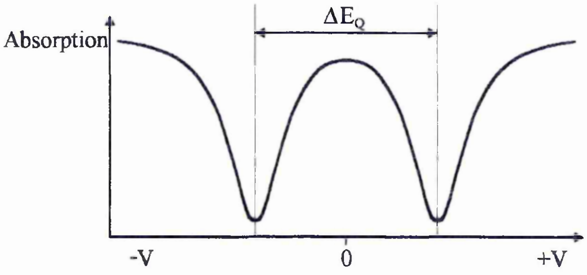

Figure 2.10 Mössbauer spectrum showing a quadrupole splitting.

In general an isomer shift (δ) as well as a quadrupole split (ΔE_Q) is seen as in figure 2.11.

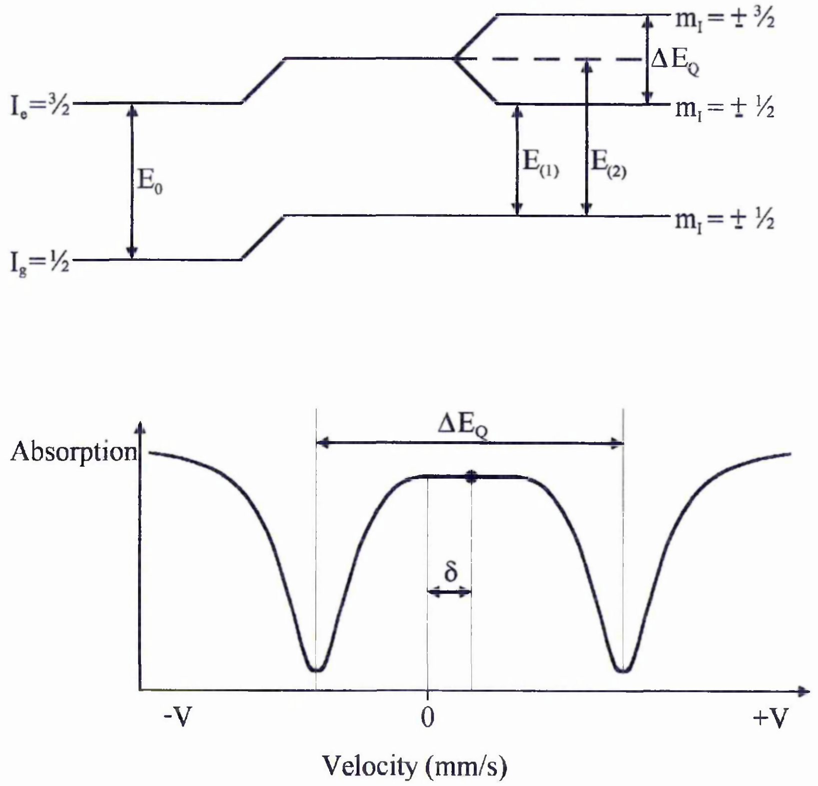

Figure 2.11 An isomer shift and a quadrupole splitting.

The size of the quadrupole splitting is proportional to the z component of the EFG tensor which interacts with the quadrupole moment of the nucleus. The EFG tensor has nine components and the electric field at the Mössbauer nucleus is the negative gradient of the electrostatic potential, V (8).

$$\underline{E}=-\nabla V=-(\underline{i}V_x+\underline{j}V_y+\underline{k}V_z) \tag{2.37}$$

Where

$$V_x=\frac{\delta V}{\delta x} \tag{2.38}$$

$$V_y = \frac{\delta V}{\delta y} \tag{2.39}$$

$$V_z = \frac{\delta V}{\delta z} \tag{2.40}$$

The EFG is the gradient of the electric field E, and is expressed as a 3×3 matrix containing the resultant combinations of the cartesian axes from the centre of the nucleus (8).

$$EFG = \nabla E = \begin{vmatrix} V_{xx} & V_{xy} & V_{xz} \\ V_{yz} & V_{yy} & V_{yz} \\ V_{zx} & V_{zy} & V_{zz} \end{vmatrix} \tag{2.41}$$

Where

$$V_{ij} = \frac{\delta^2 V}{\delta_i \delta_j} \tag{2.42}$$

The tensor can be reduced to diagonal form if the co-ordinate axes are properly chosen so that the EFG is described by the three components V_{xx}, V_{yy} and V_{zz}. These components are related by the Laplace equation in a region where the charge density disappears.

$$V_{xx} + V_{yy} + V_{zz} = 0 \tag{2.43}$$

There are two independent components, usually V_{zz} and an asymmetry term η, where

$$\eta = \frac{(V_{xx} - V_{yy})}{V_{zz}} \tag{2.44}$$

The electric field gradient axes are chosen such that the off diagonal components are zero hence

$V_{zz} \geq V_{yy} \geq V_{xx}$ making $0 \leq \eta \leq 1$

The properties of the EFG tensor are related to the symmetry properties of the crystal. Any changes in symmetry will affect the quadrupole splitting.

The EFG has two contributions. The first comes from the electrons in the atom and is called the valence contribution. If the orbital population is non-spherical then V_{zz} is non-zero. V_{zz} will be positive in sign if there is excess electron density in the xy phase (electrons in p_x, p_y, d_{xy}, $d_{x^2-y^2}$ orbitals). An excess electron density along the z-axis (electrons in p_z, d_{z^2}, d_{xz}, d_{yz} orbitals) results in V_{zz} being negative. Hence the quadrupole splitting is sensitive to changes in the electron distribution around the Mössbauer atom. A second contribution is from ionic changes associated with the ligands called the lattice contribution. This is important for an s-state ion where there is negligible valence contribution.

2.2.3 Magnetic Hyperfine Interaction

The magnetic hyperfine interaction is the result of an interaction between the nuclear magnetic dipole moment μ and the magnetic dipole moment B at the nucleus. This interaction is called the nuclear Zeeman effect and only occurs if there is a magnetic field at the nucleus. The magnetic field may be caused by the atoms own electrons, long-range exchange interactions or an external magnetic field. Whatever the cause the result is removal of the degeneracy associated with the nuclear levels. The energy level shifts are described by equation 2.45.

$$E_m = \frac{-\mu_N B m_I}{I} = -g_N \mu_N B m_I \tag{2.45}$$

$(m_I = I, I-1, I-2, \ldots\ldots\ldots, -I)$

where

μ_N = Nuclear Bohr magnetron

g_N = Nuclear gyromagnetic ratio

m_I = Magnetic quantum number

B = Magnetic hyperfine field

From equation 2.45 it can be seen that there will be 2I + 1 equally spaced sub levels. γ-Transitions between two nuclear levels of spin I_1 and I_2 may be observed in the Mössbauer experiment. Only particular transitions dependent on multipolarity and selection rules are allowed.

Consider the magnetic splitting of natural iron, there are six allowed γ-transitions corresponding to the selection rule (2.46).

$$\Delta m_I = 0, \pm 1 \tag{2.46}$$

This is illustrated in figure 2.12.

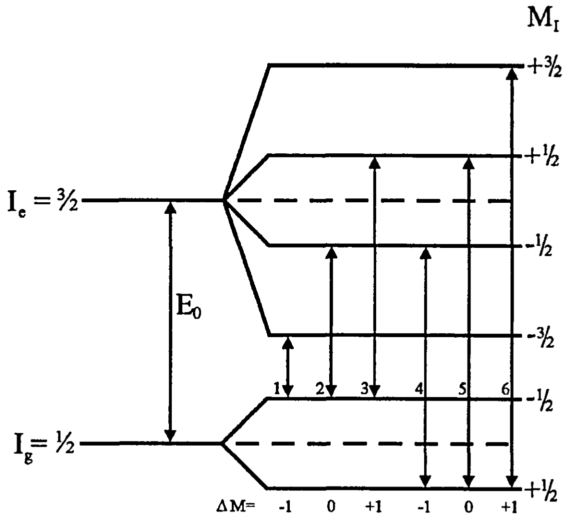

Figure 2.12 Magnetic splitting of natural iron.

The ^{57}Fe spectrum is used as a calibrant owing to the equal spacing between lines (1, 2), (2, 3), (4, 5) and (5, 6). Their intensities however differ.

$$I_1 = I_6 = 3(1 + \cos^2\theta) \quad (2.47)$$

$$I_2 = I_5 = 4\sin^2\theta \quad (2.48)$$

$$I_3 = I_4 = 1 + \cos^2\theta \quad (2.49)$$

Where θ = angle between the effective field B, and direction of the γ-beam.

Integration of the three expressions (2.47, 2.48, 2.49) assuming a random orientation gives an area ratio of the lines as 3:2:1:1:2:3, shown in figure 2.13.

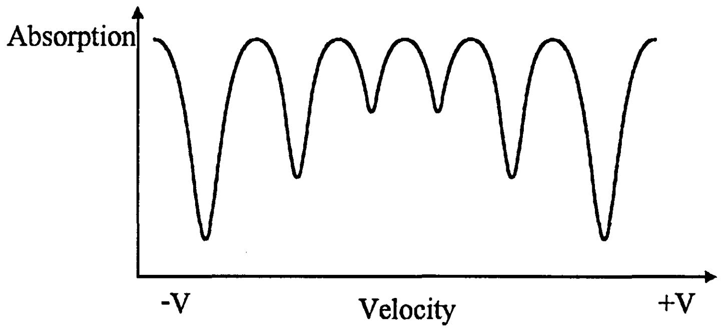

Figure 2.13 Mössbauer spectrum showing the magnetic hyperfine splitting in ^{57}Fe.

REFERENCES

1 W. E. Lambe, Jr., *Physical Rev.*, 1939, 55, 190-197.

2 R. H. Dicke, *Physical Review*, 1953, 89, 472-473.

3 N. N. Greenwood and T. C. Gibb in *Mössbauer Spectroscopy*, Chapman and Hall Ltd, London, 1971.

4 G. J. Long in *Mössbauer Spectroscopy Applied to Inorganic Chemistry*, Vol. 1, Plenum Press, New York and London, 1984, Chapter 1.

5 U. Gonser in *Topics in Applied Physics: Mössbauer Spectroscopy*, Volume 5, Springer-Verlag, Berlin, Heidelberg, New York, 1975, Chapter 1.

6 G. M. Bancroft in *Mössbauer Spectroscopy: An Introduction for Geochemists*, McGraw Hill, London, 1973.

7 G. Breit and E. Wigner, *Phys. Rev.*,1936, 49, 519.

8 G. M. Bancroft and R. H. Platt in *Advances in Inorganic Chemistry and Radiochemistry* Volume II, Academic Press, New York and London, 1972.

CHAPTER THREE

TECHNIQUES

3 EXPERIMENTAL TECHNIQUES AND INSTRUMENTATION

3.1 THE MÖSSBAUER ISOTOPE

A number of factors influence whether a particular isotope is useful for investigation using the Mössbauer technique:-

- the source must emit low energy γ-rays (<150KeV) to give high recoil free values.
- the γ-ray energy must be well separated from other photons to minimise background levels.
- the source must emit an unsplit γ-ray.
- the magnitude of the Mössbauer effect is proportional to the area of absorption. For a 'thin' Mössbauer absorption line (1):

  $$A = \tfrac{1}{2}\pi f_a f_s \sigma_o n x \tag{3.1}$$

  where

  A = Area under absorption curve

  $f_a f_s$ = Recoil-free fraction of the absorber and source

  σ_o = Isotope cross section

  n = Natural abundance of isotope

  x = Absorber thickness

  A useful Mössbauer effect will come from isotopes with a large, natural abundance, recoil free fraction and cross-section.
- the line positions must be sensitive to small changes in the chemical environment and

this change needs to be measurable.

- the half life of the chosen parent isotope must have a sufficiently long-half life for experiments. ^{57}Co with a half life of 270 days is used for ^{57}Fe work. In comparison in nickel work ^{61}Co and ^{61}Cu are the parent isotopes with half lives of 1.65 hours and 3.41 hours respectively. These are too short for routine experiments.

3.2 MÖSSBAUER SOURCE

^{57}Co is used as the parent isotope for ^{57}Fe work. All the Mössbauer experiments in this work were done using ^{57}Fe Mössbauer spectroscopy.

The decay scheme of ^{57}Co is shown in Figure 3.1 (2).

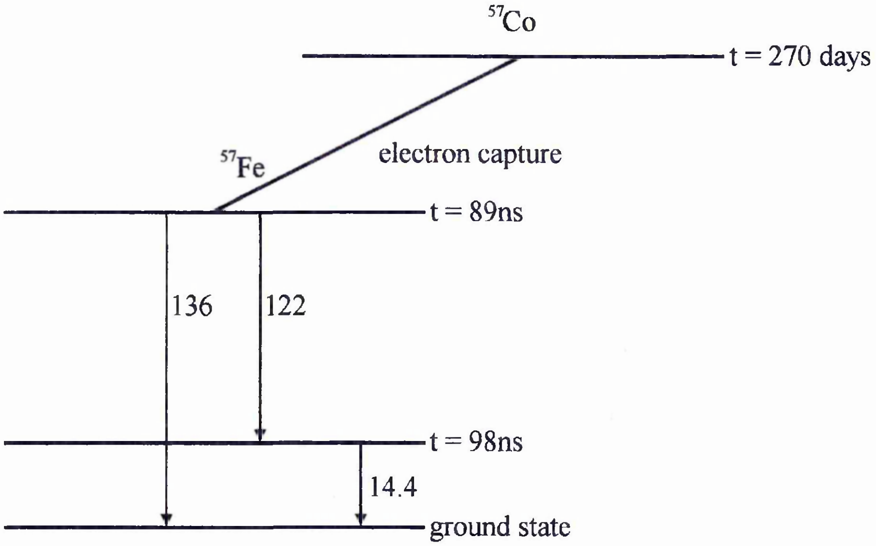

Figure 3.1 Decay scheme for ^{57}Co (2).

^{57}Co decays emitting a 14.4keV γ-ray with a natural line width of 0.1940mms^{-1} (3). The source used during this work has been a 25mCi ^{57}Co isotope in a rhodium matrix from Amersham International Limited. The initial activity of the source was 26.3mci (July 1992). The line width produced by this source is Γ_s = 0.098mm/s and the recoil free fraction at room temperature is f = 0.77. The isomer shift relative to α-Fe is + 0.11mm/s.

3.3 THE ABSORBER

The samples used during the course of this work have been solids:- powders and thin films. The powders have been enclosed in graphite or perspex holders for transmission work and crushed on to double sided Sellotape for backscatter work. The thin films have been sublimed onto graphite for transmission work, and glass for backscatter work. The thickness of the absorber can be found using (4)

$$t=\beta n f_a \sigma_o \tag{3.2}$$

where

t = Effective thickness of an absorber

n = Number of resonant nuclei / cm^3

f_a = Absorber recoil free fraction

σ_o = Resonant cross section

β = Degeneracy of states

Approximations have to be made since the value of f_a is not known for many compounds. For example the optimum amount of FePc needed for a transmission experiment without causing any saturation effect was calculated as follows:

$$t=\beta n f_a \sigma_o$$

f_a = 0.8 (assumption)

σ_o = 2.57×10^{-18} cm^2

β = 1/number lines in spectrum assume singlet = 1 t = 0.5 (for a thin absorber)

$$n=\frac{t}{f\sigma_o}=\frac{0.5}{0.8(2.57\times10^{-18})}=2.43\times10^{17\,57}Fe/cm^2 \tag{3.3}$$

Loading of ^{57}Fe allowed = $\frac{2.43\times10^{17}}{6.02\times10^{23}}\times57=2.30\times10^{-5}g/cm^2$

(Avogadro's number = 6.02×10^{23})

Weight % of ^{57}Fe in iron = 2.14%

Maximum loading of Fe allowed = $2.3\times10^{-5}\times\frac{100}{2.14}=1.075\times10^{-3}g/cm^2$

Maximum loading of thin absorber is approximately 1.075mg/cm^2.

For FePc

Molar weight FePc = 568.372

Molecular weight Fe = 55.847

Weight % Fe = $\frac{55.847}{568.372}\times100=9.826\%$

Max. loading of FePc = $1.075\times\frac{100}{9.826}=10.94mg$

Disc size = 3.46 cm^2

3.46 x 10.94 = 37.85 mg FePc ~ 40mg FePc

FePc spectrum consists of a doublet rather than the assumed singlet so

$$t = nf\sigma_o\beta \qquad n\alpha\frac{1}{\beta}$$

β = ½, n = 2n, therefore 2 × 40 = 80mg FePc.

In FePc 9.8% of the molecule is iron and only 2.14% of that 9.8% iron is ^{57}Fe.

3.4 INSTRUMENTATION

A constant acceleration spectrometer horizontally mounted was used in this work. The source was ^{57}Co in a rhodium matrix. The detector for transmission work was a gas filled proportional counter filled with Ar 95%/CH_4 5%. For backscatter work a gas flow proportional counter was used. The detector was filled with Ar/CH_4 for x-ray detection and He/CH_4 for conversion electron detection. The spectrometer was calibrated using enriched ^{57}Fe foil. The obtained spectra were computer fitted by a least squares method using Lorentzian lineshapes. Three types of Mössbauer experiments were used in this work:- transmission, backscatter (conversion electron and x-ray) and variable temperature Mössbauer spectroscopy.

3.5 TRANSMISSION MÖSSBAUER SPECTROSCOPY

Transmission Mössbauer spectroscopy is used to obtain information relating to the bulk properties of a sample. Figure 3.2 shows a schematic diagram of the geometry of the apparatus for a transmission experiment.

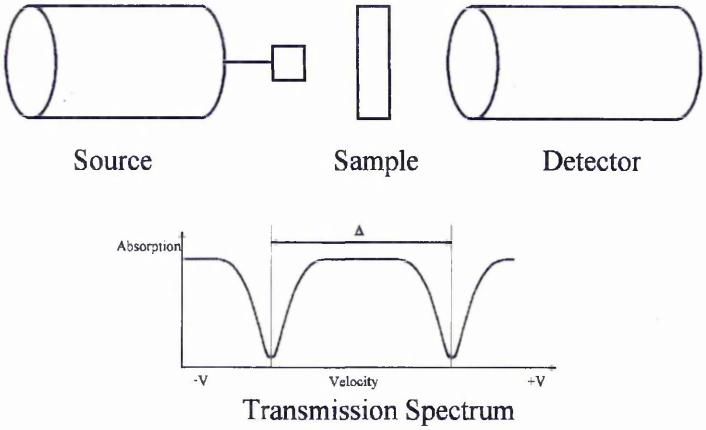

Figure 3.2 Transmission Mössbauer experimental geometry.

There are three main types of detector which are used to record low energy (Mössbauer) γ-rays: NaI(Tl) scintillation counters, proportional counters and Ge(Li) solid state counters (5). For low energy γ-rays ($E_\gamma \leq 40$KeV) gas proportional counters are the best if high energy resolution is not required. For the transmission Mössbauer spectroscopy a gas-filled proportional counter has been used. The detector is filled with a mixture of argon 95% and methane 5%. γ-rays enter the detector through a thin sheet of aluminised plastic ('Mylar'). Each photon of γ-radiation may interact with an atom of argon causing it to lose one of its outer electrons. This photoelectron has a large kinetic energy which is equal to the difference between the γ-ray photon energy and the binding energy of the electron in the argon atom. The photoelectron loses this excess kinetic energy by ionising several hundred additional atoms of the gas. Under the influence of an applied potential the mobile electrons migrate towards the central wire anode held at 2.6KV while the slower moving cations are attracted to the cylindrical metal cathode. The methane acts as a quenching gas to minimize the production of secondary electrons when the cations strike the chamber wall (6). The pulses from the detector are then amplified. The equipment is sufficient to resolve 14.4KeV γ-rays from other γ-ray transitions, the 7.3KeV conversion x-ray peak and low energy amplifier noise.

3.5.1 Cryostat Instrumentation

Recording Mössbauer spectra at low temperatures is necessary for materials with a low Debye temperature and hence recoil free fraction. The ^{57}Co source has a high recoil free fraction at room temperature and so it is kept at room temperature. A liquid nitrogen cryostat which allows temperatures down to 80K to be achieved has been used for this work.

3.5.1.1 Liquid Nitrogen Cryostat

The liquid nitrogen cryostat (figure 3.3) operates on the principle of the controlled continuous transfer of liquid nitrogen from a reservoir to a heat exchanger which surrounds the sample space.

The sample access port is sealed by a plug which fits into an 'O' ring at the top of the sample holder. The sample is top loaded and cooled by a static column of exchange gas which thermally links the sample to a heat exchanger. The heat exchanger is positioned at the lower end of the tube and is connected to a liquid nitrogen reservoir. The coolant flows from the nitrogen reservoir down the feed capillary and into the copper heat exchanger. It leaves the heat exchanger in a concentric space about the stainless steel tube of the sample space before exhausting through a valve at the top plate.

A platinum temperature sensor and a heater are fitted to the sample holder. A sensor is also fitted to the heat exchanger. Electrical connections to the heater and temperature controller are made via a 10-pin feed through on the top plate of the cryostat.

To enable long term operation without frequent pumping of the vacuum space, a sorb pump of charcoal is fitted. This is located in the vacuum space on the nitrogen reservoir.

An integral heater is included for occasional outgassing during re-evacuation (7). The nitrogen cryostat cools to 80K and can be left without refilling with liquid nitrogen for up to 48 hours.

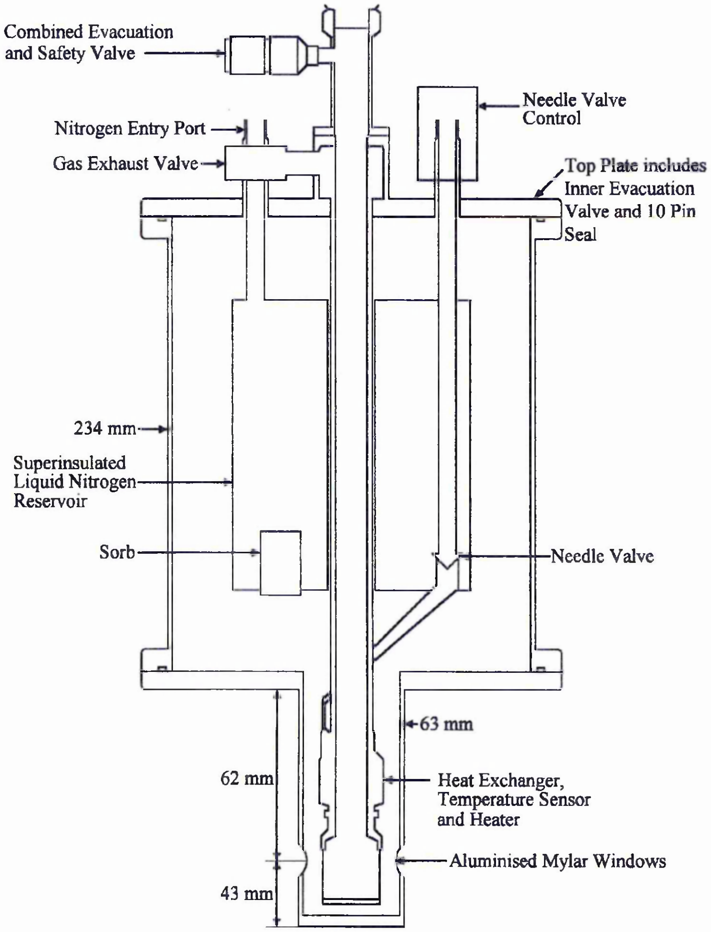

Figure 3.3 Schematic diagram of a liquid nitrogen cryostat.

3.6 VARIABLE TEMPERATURE TRANSMISSION MÖSSBAUER SPECTROSCOPY

A variable temperature Mössbauer study can give useful information about the vibrational states of a solid and hence the Debye temperature. The solid lattice can be considered as a single, quantum mechanical system and as such its levels are quantised. The form of the phonon quantisation is complex and two approximations are commonly used to interpret data:

1. The Einstein model of solids describes the thermal properties of a lattice by vibrational oscillations of the atoms with frequency V_E or angular frequency ω_E (4).
2. A more realistic representation of a solid particularly at low temperatures is the Debye model. The vibrational states are given by a certain distribution of frequencies with a characteristic maximum vibrational frequency V_D and ω_D respectively (4). The Debye temperature can be visualised as an approximate limit which separates the high temperature region where the solid can be treated in a classical fashion, from the low temperature region where quantum mechanical effects are significant (4).

When a Debye model is used instead of an Einstein model, the large number of oscillator levels in the solid and their frequency distribution need to be considered. Each of the levels has a certain probability to be excited by the recoil.

Quantitatively the Debye model gives the following expression for the recoil free fraction (4).

$$f = \exp\left(-\frac{3E_R}{2k_B\theta_D}\left[1 + 4\left(\frac{T}{\theta_D}\right)^2 \int_0^{\theta_D/T} \frac{x}{e^x - 1}\,dx\right]\right) \tag{3.4}$$

In the limit of low or high temperatures the following is obtained approximately (4).

$$f=\exp\left(-\frac{3E_R}{2k_B\theta_D}\right);T\ll\theta_D \tag{3.5}$$

$$f=\exp\left(-\frac{6E_RT}{k_B\theta_D^2}\right);T>\theta_D \tag{3.6}$$

where

f = Recoil free fraction

E_R = Mean energy transferred (recoil energy)

k_B = Boltzmann constant

θ_D = Debye temperature

T = Temperature

A study of the temperature dependence of the absorption area can thus allow a determination of the Debye temperature and hence a determination of the recoil free fraction. A comparison of the different Debye temperatures yields comparative information about lattice structure and the relative strengths of associated chemical bonds.

3.7 BACKSCATTER MÖSSBAUER SPECTROSCOPY

Backscatter Mössbauer spectroscopy is used to obtain information about the surface of a sample. Figure 3.4 shows a schematic diagram of the instrument geometry for backscatter work.

Table 3.1 contains the principal decay products of an excited state ^{57}Fe nucleus.

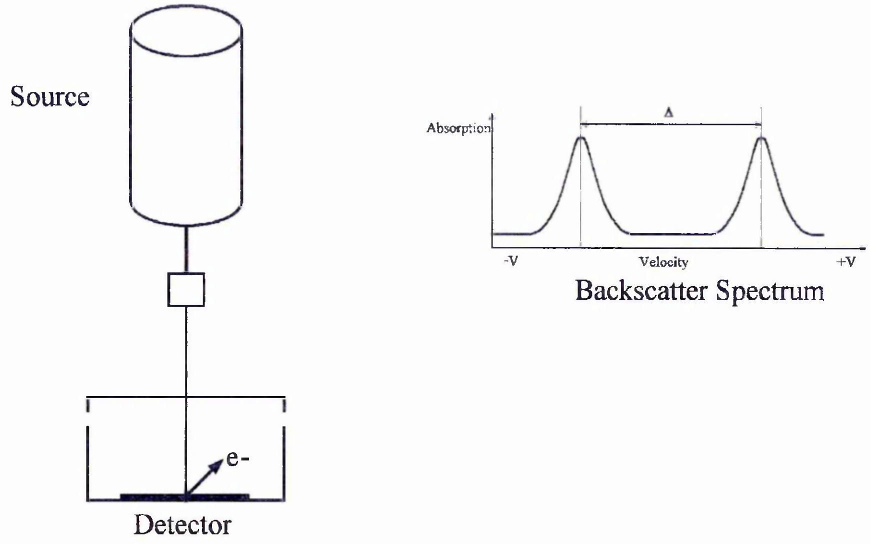

Backscatter Spectrum

Figure 3.4 Backscatter Mössbauer experimental geometry.

Table 3.1 Principal decay products of excited ^{57}Fe nucleus.

Emitted particle/ quanta	Energy KeV	Number per 100 absorption events	Approximate max. range
γ - photons	14.4	9	10,000nm
K - x-rays	6.3	27	10,000nm
K - Conversion electrons	7.3	81	250nm
L - Conversion electrons	13.6	9	900nm
M - Conversion electrons	14.3	1	
KLL - Auger electrons	5.4	63	
LMM - Auger electrons	0.53	1	

90% of the excited state nuclei decay via mechanisms which do not result in the emission of a 14.4KeV γ-ray. The primary decay mechanism involves the reabsorption of the γ-rays by an inner (K) electron shell and subsequent emission 7.3KeV conversion electrons, together with associated 6.3KeV x-rays and Auger electrons. For 100 excited 14.4KeV events there are:-

81 of 7.3KeV K - conversion electrons

63 of 5.4KeV KLL - Auger electrons.

If both are detected, then a 144% effect is possible. If x-rays are detected, then a 27% effect and a 9% effect for detection of γ-rays. The penetration depth is dependent upon the absorbing material. The maximum ranges quoted are for stainless steel which contains a large amount of iron. Organic samples such as FePc containing only a small amount of iron (9.8% of compound) will therefore probably need to be thicker than such inorganic samples containing more iron.

If the backscattered photons are detected information pertaining to the bulk or rather thick over layers of a surface phase will be obtained (8), as the paths of the γ and x radiation are at least in the order of magnitude of microns (10μm). However the backscattered CEM spectrum will be weighted towards the outermost surface regions of the sample, as only electrons produced close to the absorber surface (250nm) will escape the surface (8).

The detector used for backscatter Mössbauer spectroscopy is a gas flow proportional counter. The sample material (fluoresor) is mounted inside the chamber of the proportional detector. A mixture of helium 95% and methane 5% is used for CEMS and argon 95%, methane 5% for detection of conversion x-rays. Figure 3.5 shows the CEMS proportional counter detector. The anode wire is operated at a lower voltage for CEMS than for CXMS.

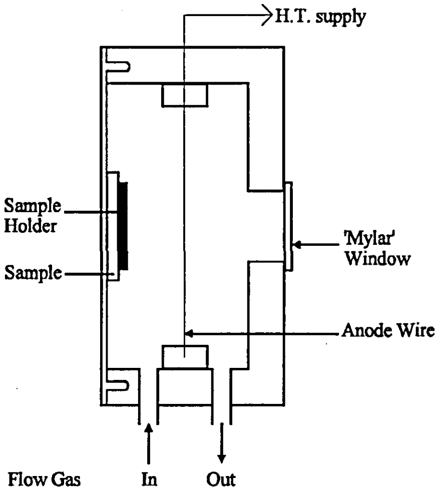

Figure 3.5 Schematic diagram of a backscatter detector.

REFERENCES

1 J. Williams, J Brooks, *Nucl. Instrum. Methods*, 1978, 128, 363.

2 T. Cranshaw, B Dale, G. Longnorth, C. Johnson, *Mössbauer Spectroscopy and its Applications*, Cambridge University Press, 1985, 14.

3 J. Stevens, V. Stevens, *Mössbauer Effect Data Index*, 1975, 54.

4 U. Gonser, *Topics in Applied Physics Volume 5, Mössbauer Spectroscopy,* Springer-Verlag, New York, 1975.

5 V. Goldanski, R. Herber, *Chemical Applications of Mössbauer Spectroscopy,* Academic press, New York, 1968, Chpt 2, N. Benczer-koller, R. Herber, Experimental methods.

6 D Skoog, *Principles of Instrumental Analysis*, Edition 3, Saunders College Publishing, Phildelphia, 1985.

7 Oxford Instruments Limited, *Instruction Manual for Variable Temperature Liquid Nitrogen Cyrostat,* 1984.

8 M. Tricker, *Mössbauer Spectroscopy and its Chemical Applications,* American Chemical Society, Washington DC, 1981, Edited J. Stevens & G. Shenoy Pg 63-101.

CHAPTER FOUR

EXPERIMENTAL - PREPARATION

4 PREPARATION OF IRON PHTHALOCYANINE PHASES

4.1 CHEMICALS USED

The chemicals used in these experiments have been obtained from various sources which are listed below and were used without further purification. Iron powder, iodine, and iron (II) chloride tetrahydrate were supplied by Aldrich Chemical Company Limited. Phthalonitrile, and 1,5 diazabicyclo [4.3.0] non-5-ene were supplied by Lancaster Synthesis Limited. Laboratory dried ethanol was initially used but in later experiments dry ethanol supplied by Aldrich Chemical Company Limited was used. Crude iron phthalocyanine was prepared in the laboratory and was also obtained from Kodak, and Pfaltz and Bauer. The crude FePc was purified before use.

4.2 PREPARATION OF IRON PHTHALOCYANINE

4.2.1 Method 1 Outlined by Busche (1)

Phthalonitrile (2.9g, 0.023 mole) and iron powder (5g, 0.09 mole) were mixed and placed in a 25ml conical flask. The mixture was heated to 260°C for 5 hours in a sandbath. Phthalonitrile condensed on the cooler upper portion of the condenser and was scraped back into the reaction vessel. The finely ground blue product obtained was extracted with a Soxhlet extractor using ethanol (200ml) for 5 hours and then pyridine (200ml) for 5 hours. The ethanol extract was discarded and the pyridine extract reduced in volume using a rotary evaporator to 20ml. Hexane was added to precipitate the blue [phthalocyaninato (2)] bis(pyridine) iron (II), ($Fe(Pc)py_2$). The precipitate was collected by suction filtration, washed with ethanol and dried in vacuum to give Fe(Pc)py_2, yield 9.5%. The Fe(Pc)py_2 was purified using entrainer sublimation (see section 4.6).

4.2.2 Method 2 Outlined by Tomoda et al (2)

This method used a metal halide : phthalonitrile : DBN, ratio of 1 : 4 : 10. Iron (II) iodide was made in-situ: Iron powder (1.96g, 0.0351 moles) was placed in a round bottomed flask in dry ethanol (200ml), iodine (4.16g, 0.0164 mole) was added slowly with constant stirring (magnetic flea). The reaction was kept in a nitrogen atmosphere and left for 48 hours to ensure completion. The solution became a brown colour which darkened as the reaction continued. Phthalonitrile (8.30g, 0.0648 mole), 1,5 diazabicyclo [4.3.0] non-5-ene (20.10g, 0.1618 mole) and dry ethanol (50ml) were added to the iron iodide (5.08g, 0.0164 mole) in ethanol mixture. The flask was wrapped in aluminium foil and the mixture refluxed under nitrogen for 48 hours after which the resultant green solution was filtered, yielding a purple precipitate. This solid was washed with dry ethanol, then diethylether and the purple solid was vacuum dried (yield 75%). The crude material was purified using entrainer sublimation.

4.3 IRON CONTENT ANALYSIS USING ATOMIC ABSORPTION SPECTROSCOPY

The atomic absorption work was carried out on a Phillips PU100 atomic absorption spectroscopy instrument. The instrument conditions for the iron analysis were as follows:

Oxidant setting:	30	Bandpass:	0.2nm
Fuel setting:	30 for ignition, thereafter 20	Wavelength:	247nm
Flame type:	Lean	Lamp current:	5A

Three FePc samples (purified using entrainer sublimation) were analysed in duplicate,

FePc 1 - Pure FePc produced at Sheffield Hallam University 15/8/91 by J. O'Rourke

FePc 2 - Pure Kodak FePc

FePc 3 - Pure FePc produced at Sheffield Hallam University 26/7/91 by N. A. Bell

All glassware used in this experiment was thoroughly cleaned with concentrated nitric acid, followed by concentrated ammonia and then deionised water and distilled water used only for atomic absorption experiments. Calibration standards containing 25, 50, 75 and 100ppm Fe (II) were used. Each FePc sample was carefully weighed and dissolved in 2ml of concentrated nitric acid and made up to 25ml with distilled water in a volumetric flask.

4.4 PREPARATION OF DIFFERENT PHASES OF FePc

4.4.1 Method 1

Concentrated sulphuric acid (20-30ml) was added dropwise with stirring to the β-purple needle-like FePc crystals. The crystals dissolved to form a dark purple viscous solution. The solution was poured into Millipore water (550ml) and a floc immediately formed. The precipitate was left to settle for a few hours and filtered. The precipitate was then placed in another large amount of water to remove all traces of the sulphuric acid and re-filtered yielding a purple powder.

4.4.2 Method 2

β-FePc crystals (0.04g, 7.0×10^{-5} mole) were placed in a small volume of pyridine, picoline, 1,4-dioxane and dimethylamine in four separate glass tubes. The tubes were stoppered and placed in a thermostat controlled water bath at 50°C for 48 hours in a fume cupboard. Each solution was filtered and the precipitate dried at 60°C in a heated drying tube under vacuum.

4.5 COMPARISON OF CRUDE FePc SAMPLES USING MÖSSBAUER SPECTROSCOPY

Three crude FePc samples were compared using Mössbauer spectroscopy :-

(i) Laboratory prepared crude FePc

(ii) Kodak crude FePc

(iii) Pfaltz and Bauer crude FePc.

80mg of each sample were mixed with high purity graphite and placed in a sample holder. A transmission Mössbauer experiment at 80K was set up using a ^{57}Co source in a rhodium matrix. The spectra were computer fitted using a least squares method and Lorenzian lineshapes. The optimum mass was calculated to be 80mg (Chapter 3, section 3.3). If too little sample were used it would not be possible to collect a spectrum and, if too much was used, saturation would occur.

4.6 ENTRAINER SUBLIMATION

Purification of crude iron phthalocyanine was carried out using entrainer sublimation. Figure 4.1 shows the apparatus involved in this procedure

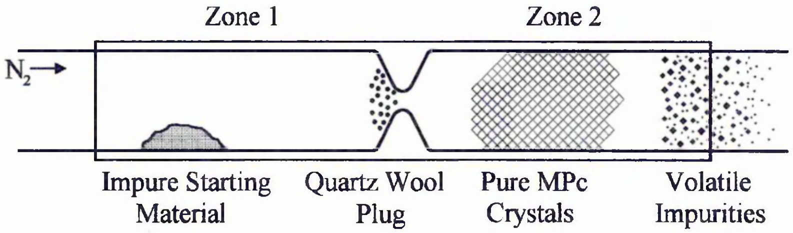

Figure 4.1 Entrainer sublimation apparatus.

The crude FePc was placed in a clean glass tube with a preformed neck about a third of the way along its length. The neck was plugged with a small piece of quartz wool. Oxygen free nitrogen was passed through a top tube containing heated copper turnings to ensure complete removal of oxygen from the nitrogen, and then continuously through the tube containing the sample. The furnace surrounding the glass tube was slowly heated in zone 1 to 500°C and in zone 2 to 300°C. The FePc sublimed and formed crystals in zone 2, while involatile material remained in zone 1 and volatile material was carried beyond zone 2. After sixteen hours the glass tube was left to cool, then broken at the neck and the pure crystals scraped out using a micro spatula. Figures 4.2 and 4.3 (shown overleaf) show the crude and pure forms of FePc respectively.

4.7 SEPARATION OF THE α AND β PHASES OF FePc

Figure 4.4 shows the cold finger apparatus which was used to isolate α and β FePc.

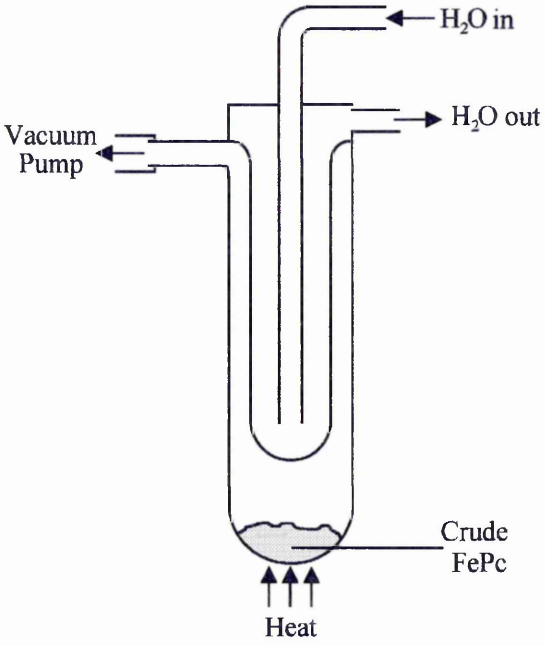

Figure 4.4 Cold finger apparatus.

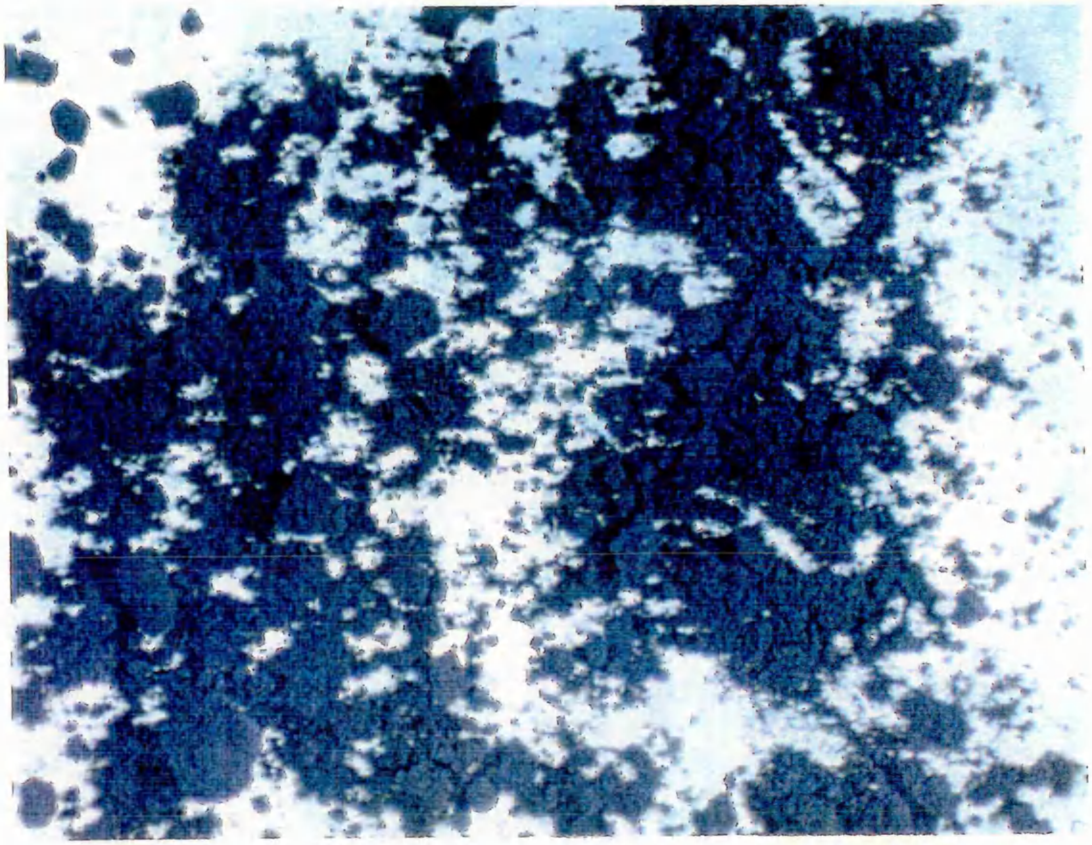

Figure 4.2 Crude FePc.

Figure 4.3 Pure FePc.

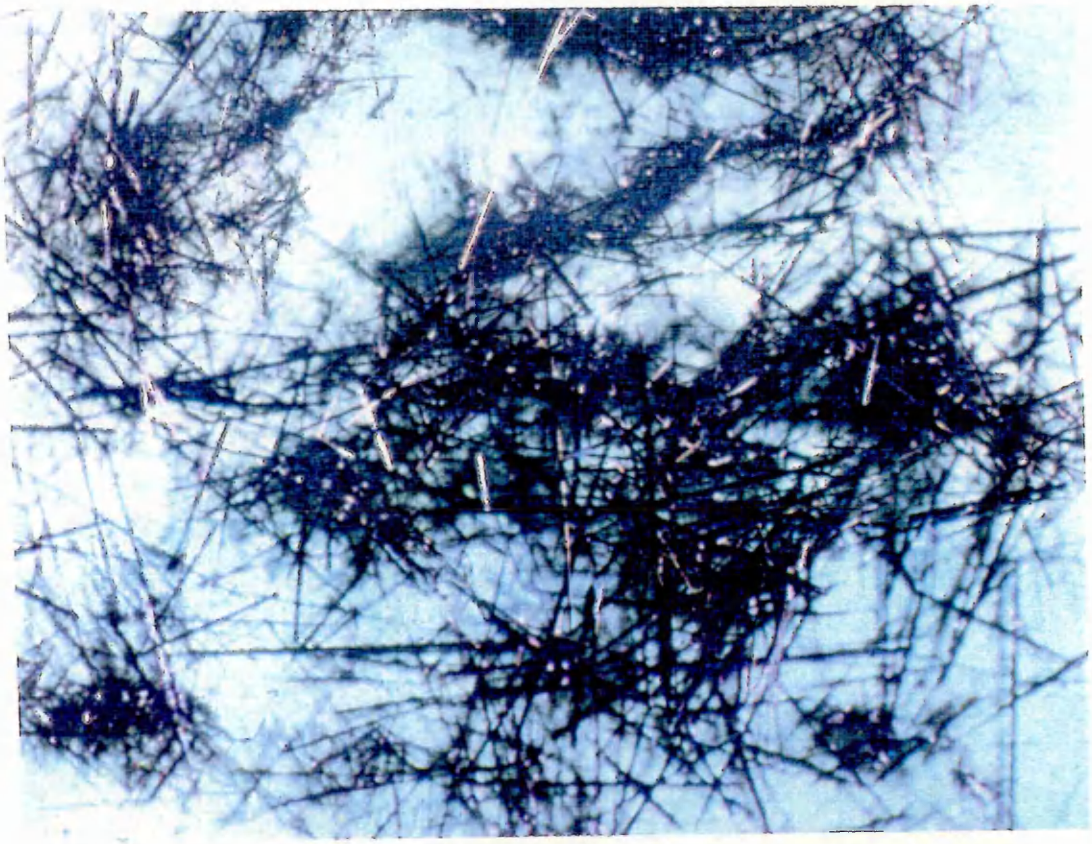

Crude FePc was placed in the bottom of the tube. Water was allowed to flow in and out of the cold finger, keeping the finger cool. A vacuum of 10^{-6}torr was maintained in the apparatus and the apparatus placed in a graphite bath and heated using a cylindrical furnace. During heating a thermocouple was kept in the graphite to monitor the temperature. The initial experiment was operated at a temperature of 200°C when a white impurity sublimed onto the cold finger. When sublimation was complete the white phthalonitrile impurity was cleaned off the cold finger and the tube heated to 500°C and maintained for two days. A dark purple powder sublimed onto the water cooled finger and small needle like crystals formed around the sides of the outer tube.

4.8 EDWARDS VACUUM COATER

Figure 4.5 shows a schematic diagram of the Edwards E306A coater for vacuum sublimation of thin films.

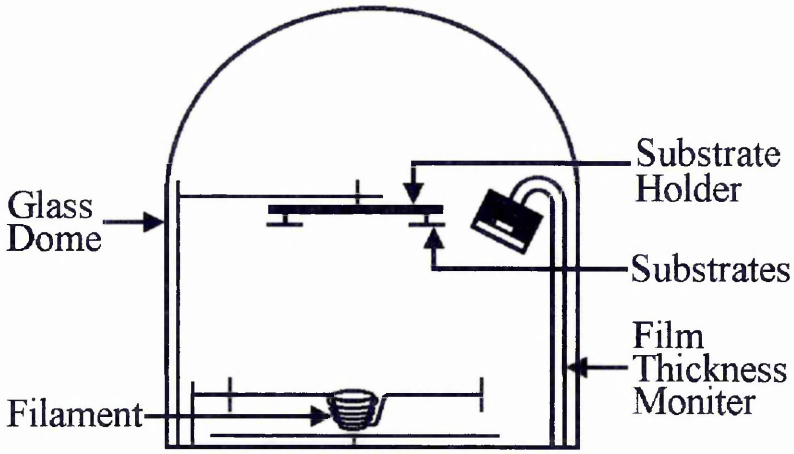

Figure 4.5 Edwards E306A vacuum coater.

Mounted substrates (graphite discs, glass slides, alumina SEM stubs) were held in position in the E306A chamber above a quartz crucible filled with a sample of pure FePc. A piece of glass wool was placed on top of the crucible. The chamber was pumped down to 10^{-5}torr and the crucible slowly heated by means of a heating coil. The substrates were rotated using an electric motor ensuring an even coating. The FePc was slowly sublimed on to the substates. The film thickness was monitored using a quartz FTM5 crystal placed in an equivalent position to the substrates. Thin films (500nm) were sublimed at a rate of 0.2 - 0.3nm/s on to the substrates.

4.9 INFRA-RED SPECTROSCOPY

All infra-red spectroscopic work mentioned in this chapter was carried out using the Perkin Elmer 298 infra red spectrophotometer.

4.10 RESULTS / DISCUSSION

4.10.1 Iron Phthalocyanine Synthesis

Two methods for the synthesis of FePc have been attempted. The first method was outlined by Busche (1) and the second one was based upon a method outlined by Tomoda et al (2), for the production of both metal-free phthalocyanine (H_2Pc) and copper phthalocyanine. Workers at Kent University have successfully adapted the method of Tomoda et al to produce lead phthalocyanine in greater than 70% yields. These methods were adapted for the preparation of FePc. Both methods produced poor yields of FePc. The Busche method resulted in a 9.5% yield and the method of Tomoda et al a 9.8% yield. It was decided to concentrate on only one of the methods, and due to the success that Kent University workers had in adapting the latter method for PbPc, and the undesirable use of large quantities of pyridine in the former method, it was decided to concentrate on the method of Tomoda.

In this method 1,5 diazabicyclo [4.3.0] non-5-ene (DBN) gave a better yield in the production of H_2Pc than 1,8 diazabicyclo [5.4.0] undec-7-ene (DBU) so DBN was chosen for the preparation of FePc. Initially laboratory dried ethanol was used in the preparation but owing to uncertainty in the quality of the ethanol, Aldrich anhydrous ethanol was subsequently used in the method. After some early preparation difficulties the $FeCl_2$ was examined by wet chemical tests and Mössbauer spectroscopy. These tests showed that there was heavy iron (III) contamination of the sample. Removal of water from a new bottle of $FeCl_2.4H_2O$ was attempted by refluxing the sample with thionyl chloride since this is the standard method of preparing anhydrous halides from their hydrated salts.

$$H_2O + SOCl_2 \rightarrow 2HCl + SO_2$$

This proved to be unsuccessful. The possibility of using other Fe(II) halides was investigated. Iron (II) bromide ($FeBr_2$) and iron (II) iodide (FeI_2) can both be prepared easily by reaction of the elements (3). FeI_2 is the least easily oxidised of the two, and so was chosen as the starting material. During the in-situ preparation of FeI_2 an excess of iron powder is used to ensure all the iodine reacts since it is easy to remove the excess iron at the end of the FePc synthesis with a magnet. If too little FeI_2 is produced there is a possibility that the phthalonitrile and DBN in excess could form H_2Pc producing a mixture of FePc and H_2Pc. The FeI_2 is the limiting factor in this reaction. The reaction flask was wrapped in aluminium foil during the reaction to minimise any possible photochemical reactions taking place. After adapting this method the crude product was obtained with a 75% yield as a purple powder.

4.10.2 Possible Reaction Mechanism

Figure 4.6 shows a scheme for the reaction mechanism. The DBN is acting as a base in the reaction and removes hydrogen from the ethanol, resulting in an ethoxide anion. The ethoxide anion, acting as a nucleophile, attacks the carbon attached to nitrogen in

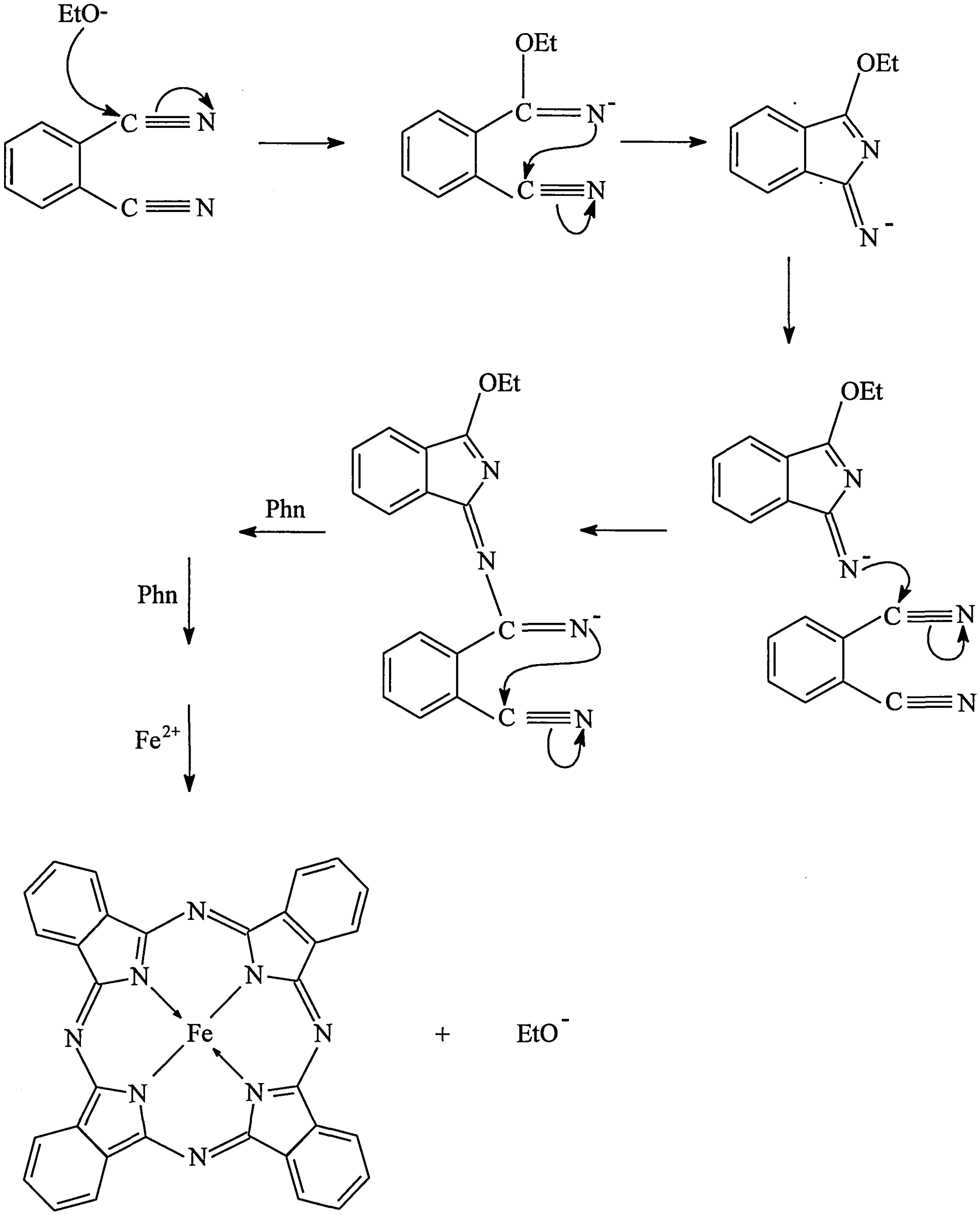

Figure 4.6 Possible reaction mechanism for the formation of FePc.

phthalonitrile, resulting in the formation of a 5-membered ring. This molecule has a resulting negative charge on a nitrogen which in turn acts as a nucleophile and again the carbon attached to the nitrogen in another phthalonitrile molecule is attacked. This continues twice more until all four molecules are joined together in a ring, the metal joins the centre of the ring and the ethoxide anion is regenerated.

4.10.3 Comparison of Crude FePc from Various Sources

Comparison of the crude FePc's produced in the laboratory with the samples obtained from Kodak and, Pfaltz and Bauer was made using Mössbauer spectroscopy. Table 4.1 shows the Mössbauer parameters for these samples.

Table 4.1 Mössbauer parameters of the crude FePc samples.

FePc sample at 80K		δ mm/s (Fe) ±0.02mm/s	Δ mm/s ±0.02mm/s
Lab. prepared (JO223)	A B	0.48 0.47	2.64 0.85
Kodak supplied (JO229)	A B	0.45 0.48	2.67 0.79
Pfaltz and Bauer (JO274)	A	0.47	2.67

Table 4.2 contains the quoted ranges for the isomer shift, δ and the quadrupole splitting, Δ of Fe (II) and Fe (III) character.

Table 4.2 Quoted Mössbauer δ and Δ ranges of Fe (II) and Fe (III) character (4).

Sample	δ mm/s (Fe)	Δ mm/s
Fe (II)	0.7 - 1.6	1.5 - 3.7
Fe (III)	0.1 - 0.7	0 - 1

Figures 4.7-4.9 show the Mössbauer spectra for these samples which indicates that the

Kodak sample contains a large amount of iron (III) impurities and only a small amount of the iron (II) compound.

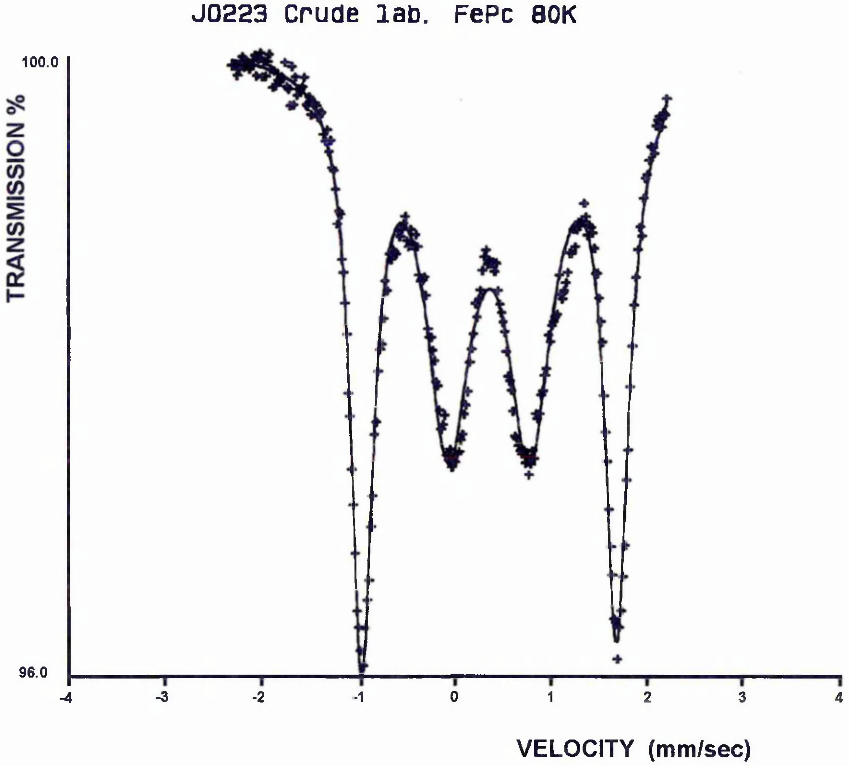

Figure 4.7 Transmission Mössbauer spectrum at 80K of crude lab. prepared FePc.

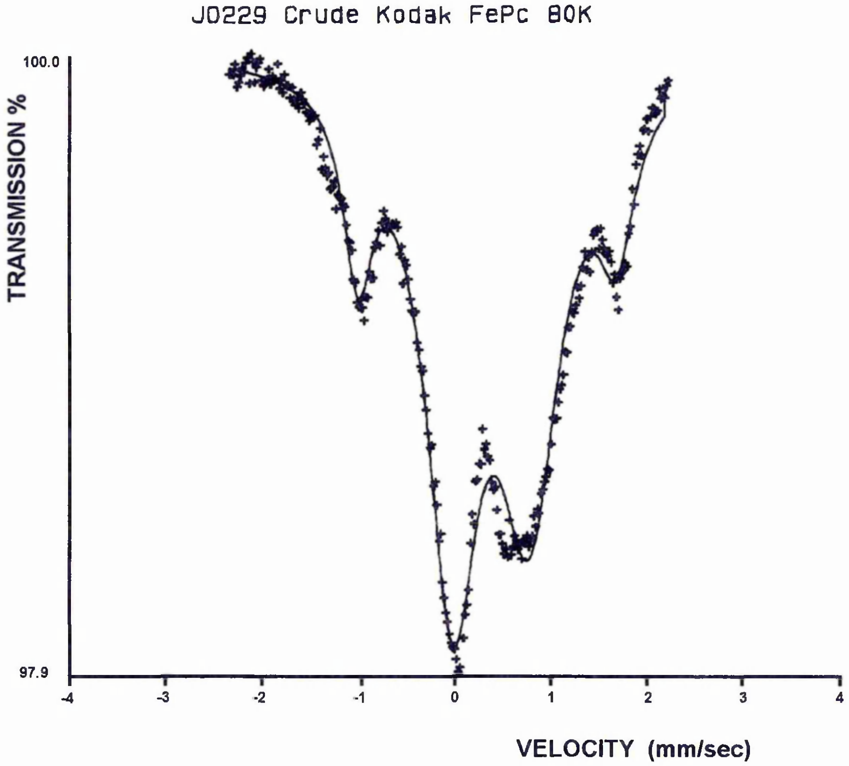

Figure 4.8 Transmission Mössbauer spectrum at 80K of crude Kodak supplied FePc.

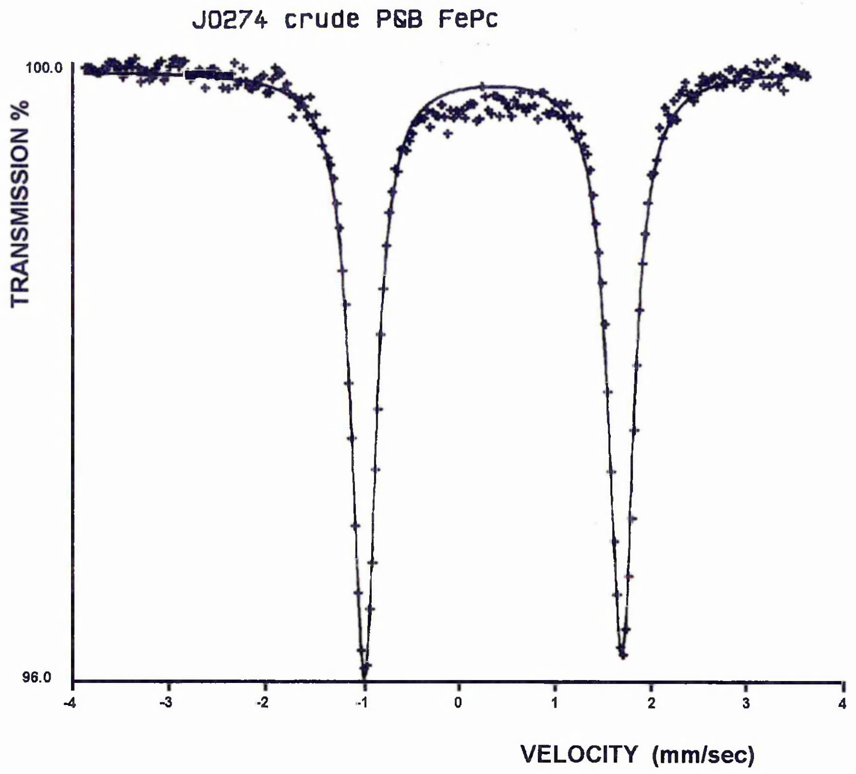

Figure 4.9 Transmission Mössbauer spectrum at 80K of crude Pfaltz and Bauer supplied FePc.

The sample from Pfaltz and Bauer shows no iron (III) impurity and produces a well defined spectrum. The crude FePc prepared in the laboratory shows a small iron (III) impurity and large iron (II) presence. It was thought that purification of these crude powders would be most efficient with both the Pfaltz and Bauer sample and the laboratory prepared sample but would give a low yield with the Kodak sample.

4.10.4 Entrainer Sublimation

Entrainer sublimation was one technique used to purify the crude FePc. This purification yielded purple needle like crystals which were β-phase crystals (identified later). The purification removed impurities such as excess phthalonitrile. Transmission Mössbauer spectra of the FePc before and after purification can be seen in figures 4.10 and 4.11.

Table 4.3 contains the related Mössbauer parameters of FePc demonstrating the effect of purification.

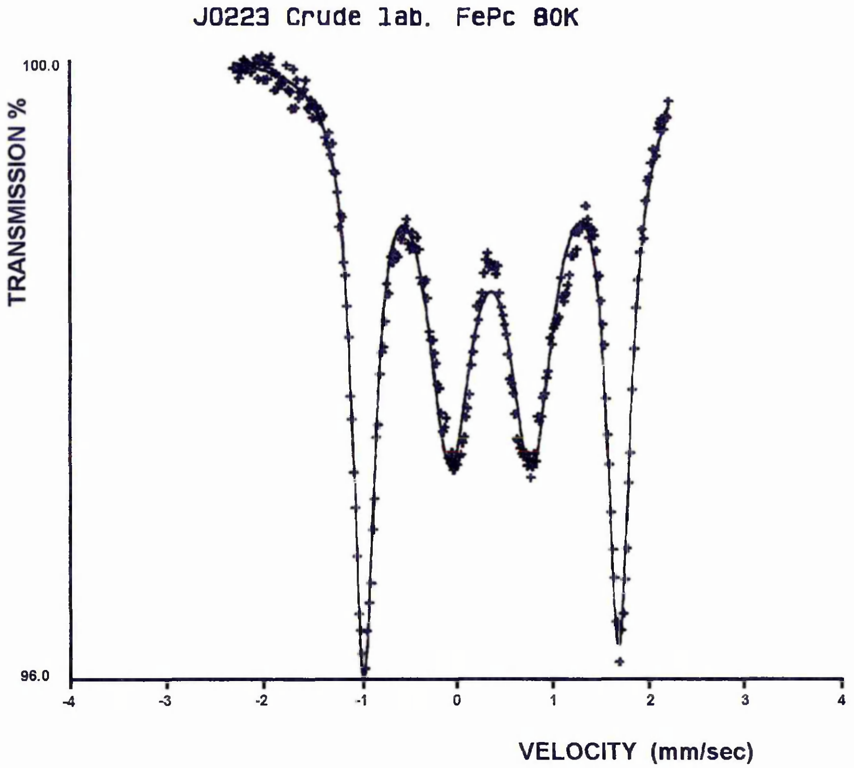

Figure 4.10 Transmission Mössbauer spectrum at 80K of FePc before purification.

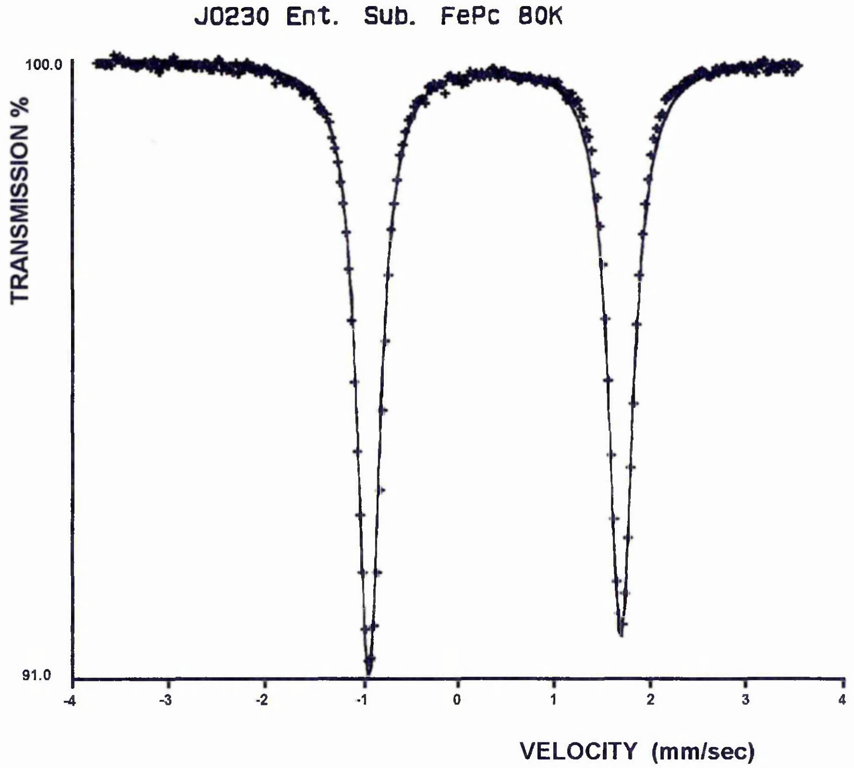

Figure 4.11 Transmission Mössbauer spectrum at 80K of FePc after purification.

Table 4.3 Mössbauer parameters of FePc demonstrating the effect of purification.

Sample	δ mm/s (Fe) ± 0.02mm/s	Δ mm/s ± 0.02mm/s
FePc as synthesised	0.48 0.47	2.64 0.85
FePc after purification	0.48	2.62

Comparison of these spectra clearly shows the Fe(III) impurity is removed during the entrainer sublimation process.

4.10.5 Medac Analysis

The purified laboratory prepared FePc was sent to Medac, at Brunel university for carbon (C), hydrogen (H) and nitrogen (N) analyses. The iron (Fe) content was determined using atomic absorption spectroscopy in the laboratory. Table 4.4 contains the information from these analyses.

Table 4.4 Medac analysis of FePc.

Sample (Pure)	C %	H %	N %	Fe %
Theoretical	67.61	2.84	19.71	9.8
FePc 1-J. O'Rourke laboratory prepared FePc	67.63	2.85	19.75	9.8
FePc 2-Kodak FePc	-	-	-	10.3
FePc 3-N. Bell laboratory prepared FePc	-	-	-	9.9

From table 4.4 it can be seen that the entrainer sublimed laboratory prepared sample was essentially pure FePc. The theoretical and found values for each sample show good agreement.

4.10.6 Iron Phthalocyanine Phases

As already mentioned in the literature review, there are at least two phases (α and β) of FePc (5). Entrainer sublimation has been shown to yield only the β-phase crystals (6). It was necessary to use another method to produce the α-powder. α-phases of some metal phthalocyanines have been produced by dissolving crystals of the β-form in a minimum of concentrated sulphuric acid (7) and then precipitating the α-form by pouring the solution into a large amount of Millipore water and filtering. The precipitate then needs to be washed with water to remove traces of sulphuric acid (8). This method was attempted with pure β-FePc crystals. The transmission Mössbauer spectrum of the product can be seen in figure 4.12 which consists of two doublets. The parameters are listed in table 4.5. Also listed in table 4.5 are some Mössbauer parameters of FePc from the literature.

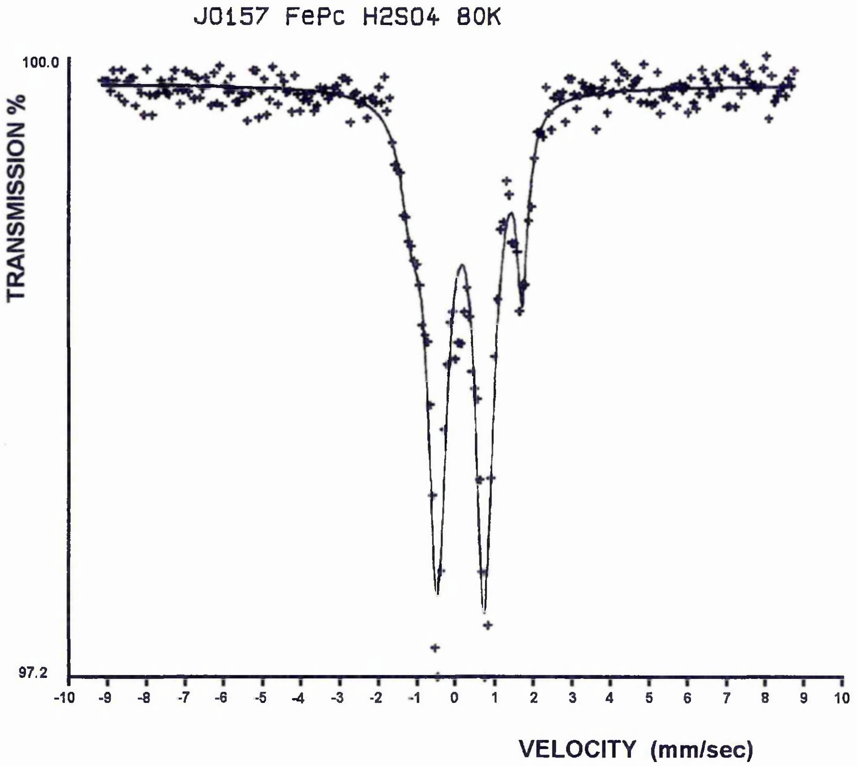

Figure 4.12 Transmission Mössbauer spectrum at 80K of acid pasted sample.

Table 4.5 Mössbauer parameters of FePc after acid pasting and literature values.

Sample	δ mm/s (Fe)	Δ mm/s	References
Lab. sample after acid pasting: JO157	0.24 ± 0.02 0.37 ± 0.02	1.22 ± 0.02 2.88 ± 0.02	
α-FePc	0.46 ± 0.01 0.48 ± 0.01	2.49 ± 0.01 2.68 ± 0.01	5 5
Monomer FePc on carbon support	0.26 0.45 0.48	1.25 0.63 2.46	9 9 9
Polymer FePc on carbon support	0.35 0.23 0.44	2.88 1.95 0.82	9 9 9

Comparison of the parameters obtained at 80K with literature valves of α-FePc clearly indicate that the transformation from β to α has not occurred. A change has taken place since they do not correspond to the β-phase either. Blomquist et al (9) quotes values for monomeric and polymeric forms of FePc on a carbon support. It is interesting that the dominant doublet (underlined) from the monomer and polymer on the carbon support correspond to both doublets in the sample after acid pasting. This area was not further pursued since the aim was to produce α-FePc which has clearly not been achieved. A second attempt at the β to α conversion involved placing the β-crystals in solvents in a stoppered bottle at 50°C for 48 hours followed by filtration and drying at 50-70°C under reduced pressure (10). Table 4.6 contains the infrared spectral bands of the resultant samples in the region 700-800cm^{-1} which is the region used to distinguish between the phases.

Table 4.6 Infra-red bands of acid pasted samples.

Sample	Infra-red bands cm^{-1}			
β-FePc	740	760	767(sh)	785,
α-FePc (11)	725		770	
Pyridine treated sample	730	760	770(sh)	782
Picoline treated sample	740	760		784
1, 4 dioxane treated sample	740	760	767(sh)	785
Dimethylamine treated sample	740	757	770(sh)	782

These results show that 1,4-dioxane and dimethylamine have not caused any phase change. The absence of the shoulder at $770cm^{-1}$ with the picoline product indicates that some change has occurred. With the pyridine the peak is at $730cm^{-1}$ rather than at $740cm^{-1}$, implying that a phase change has occurred, however the occurrence of the shoulder rather than a peak at $770cm^{-1}$, and a peak at $782cm^{-1}$ indicates that this is not the alpha form. The desired change from β to α form has not taken place and again these experiments were not pursued.

Another method for preparation of the α-phase FePc involved vacuum sublimation of the crude material on to a water cooled finger (5). The α-FePc has been formed by vacuum sublimation of crude FePc at 500°C on to a water cooled finger and the β-phase formed by vacuum sublimation of crude FePc at 500°C on to a finger held at 250°C (5). A temperature of 500°C was found to be difficult to maintain in a controlled way with the apparatus available. A graphite bath (bunsen heated) reached 500°C but the material turned bronze in the tube which was probably a result of a decomposition and a film formed on the sides of the tube not on the finger. Use of a naked bunsen flame seemed to work without decomposing the sample, but was the least controllable way of maintaining a constant temperature. Heating in this manner resulted in the sample being heated too quickly and physically moving up the tube (not subliming) sticking to the cold finger. Pure β-FePc and crude FePc were individually sublimed using this apparatus. The bunsen was used carefully and the sample allowed to heat as slowly as possible. A lot of white impurity initially sublimed from the crude sample onto the cold finger which was removed. The sample which was deposited on the cold finger had its infrared spectrum recorded. The spectrum indicated the material on the cold finger was the β-phase and so the process had not been successful in producing the α-phase FePc with the equipment used. Another attempt at producing the α-phase using the cold finger apparatus involved using a furnace which allowed the apparatus to be heated to 500°C in a controlled manner. A vacuum system was used which allowed a pressure of 10^{-6}torr to be reached. Heat resistant blocks were placed in the furnace which allowed the apparatus to sit in the top of the furnace in a graphite bath containing a thermocouple to monitor the temperature. The β-FePc was placed in the tube and the apparatus heated to 500°C. A dark purple powder was deposited on the water cooled finger while purple needle like crystals formed on the walls of the tube. Transmission Mössbauer spectra were recorded of the samples and can be seen in figures 4.13 and 4.14. The residue showed no spectrum and the parameters of the material from the cold finger (CF) and wall (W) are listed in table 4.7.

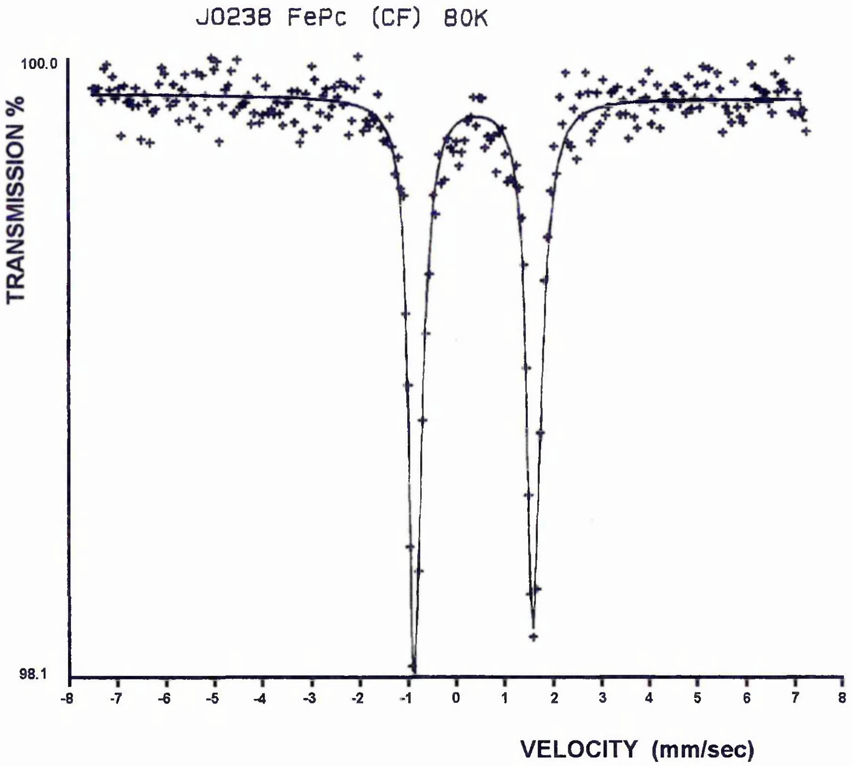

Figure 4.13 Transmission Mössbauer spectrum at 80K of the material from the cold finger.

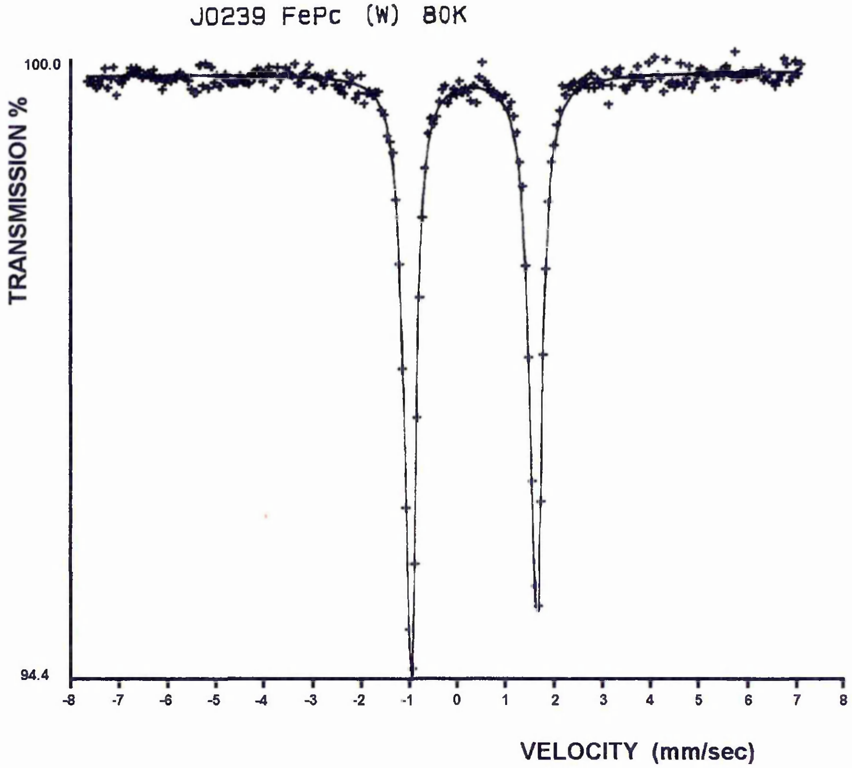

Figure 4.14 Transmission Mössbauer spectrum at 80K of the material from the walls.

Table 4.7 Mössbauer parameters of FePc deposited on CF and W.

Sample	δmm/s (Fe)	Δmm/s	Reference
JO238 FePc Cold finger	0.46 ± 0.02	2.45 ± 0.02	
JO239 FePc Wall	0.49 ± 0.02	2.61 ± 0.02	
α-FePc	0.46 ± 0.01	2.49 ± 0.01	5
β-FePc	0.48 ± 0.01	2.60 ± 0.01	12

These results showed that the procedure for producing α and β-FePc from crude laboratory prepared FePc had been successful. The α-phase is produced as a purple powder on the water cooled finger whilst the β-phase is collected as small purple needle like crystals from the walls of the tube. A temperature gradient forms from the bottom of the tube at a maximum of 500°C and the crystals were probably formed at a position on the tube where the temperature was about 250°C. Thin FePc films were produced in the Edwards E306A vacuum coater. The films were sublimed onto graphite, glass and alumina substrates for investigation using Mössbauer spectroscopy, infra-red spectroscopy and scanning electron microscopy.

4.11 SUMMARY OF RESULTS AND DISCUSSION

Crude FePc has been prepared in the laboratory based on a method by Tomoda et al. Mössbauer spectra of crude FePc from laboratory, Kodak, and Pfaltz and Bauer samples indicate that Pfaltz and Bauer is purest followed by the laboratory prepared sample, and the Kodak sample is highly impure. The β-FePc phase can be prepared as purple needle like crystals from crude FePc by entrainer sublimation and vacuum sublimation on to the walls of a tube along which a temperature gradient exists, forming at approximately

250°C. The α-phase purple powder can be produced from crude FePc by vacuum sublimation onto a water cooled finger. Transmission Mössbauer spectroscopy has been used to confirm the identity of the α and β phases. Production of the α-powder, β-crystals and FePc films have been completed for further experiments with these samples.

REFERENCES

1 Daryle H Busche, Editor-in-Chief, Inorganic Synthesis, volume XX, *Inorganic syntheses series 1*, Wiley Interscience.

2 H. Tomoda, H. Saito, S. Ogawa, S. Shiraishi, *Chem Letts.* 1980, 1277-1280.

3 *CRC Handbook of Chemistry & Physics*, CRC Press, RC Weast, 60th Edition, (1979-1980).

4 N.N Greenwood and T.C. Gibb in *Mössbauer Spectroscopy*, Chapman and Hall Ltd, London, 1971.

5 T.Srivastava, J. Przyblinski, A. Nath, *Inorg. Chem.* 1974, 13, 1562-1564.

6 J. Sharp, M. Larder, J. *Phys.Chem*, 1968, 72, 3230 -3235.

7 J. Beynon, A. Humpheries, *Trans Faraday Soc*, 1955, 51, 1065-1071.

8 T.Kobayashi, N.Uyeda, E.Suito, *J.Chem.Phys*, 1968, 72, 2446-2456.

9 J. Blomquist, L.Moberg, J. *Inorg Nucl Chem*, 1981, 43, 2287-2292.

10 F.Iwatsu, T. Kobayashu, N. Uyeda, *J.Phys.Chem*, 1980, 84, 3223-3230.

11 J.Silver, P.Lukes, A. Houlton, S.Howe, P.Iley, M Ahmet, *Sens. & Actuators*, 13, 2, (8), 1992.

12 R.Taube, H. Drevs, E. Fluck, P.Kuhn, K.F. Brauch, *Z Anorg. Allg. Chem.* 1969, 364, 297.

CHAPTER FIVE

EXPERIMENTAL

5 IRON PHTHALOCYANINE STUDIES

5.1 IDENTIFICATION OF FePc PHASES BY INFRA-RED SPECTROSCOPY

The literature indicates that if the beta form is vacuum sublimed on to a substrate an alpha film results. Annealing this alpha film should result in the beta film (1). Infra-red (IR) spectroscopy has been used to determine the phase of the as-deposited film and monitor any phase change occurring upon heat treatment.

Six potassium bromide discs were placed in a holder and 90nm entrainer sublimed laboratory prepared beta FePc films deposited using the Edwards coater. An IR spectrum of each film was recorded before and after annealing at specified temperatures using a Galaxy series FT-IR 6020 instrument. The discs were annealed in air for three hours at the following temperatures :- 134°C, 160°C, 178°C, 205°C, 220°C, 249°C. The infrared spectra can be seen in figures 5.1-5.4. At 249°C (figure 5.4) it can be seen that the film decomposed during the annealing process. A change in the spectrum can be seen in the sample annealed at 134°C (figure 5.1), but the maximum change was seen in the sample annealed at 205°C (figure 5.3), indicating a phase change is complete at this temperature. The literature indicates that the phase of the deposited film can be affected by the temperature of the substrate onto which a film is sublimed. To investigate this, reflectance FT-IR spectroscopic investigations were carried out on selected films. FePc films were sublimed on to aluminium foil wrapped around a glass slide and around a water cooled stage in the Edwards vacuum chamber. The films were prepared from

Figure 5.1 Sample not annealed (top) and sample annealed in air at 134°C for 3 hours (bottom).

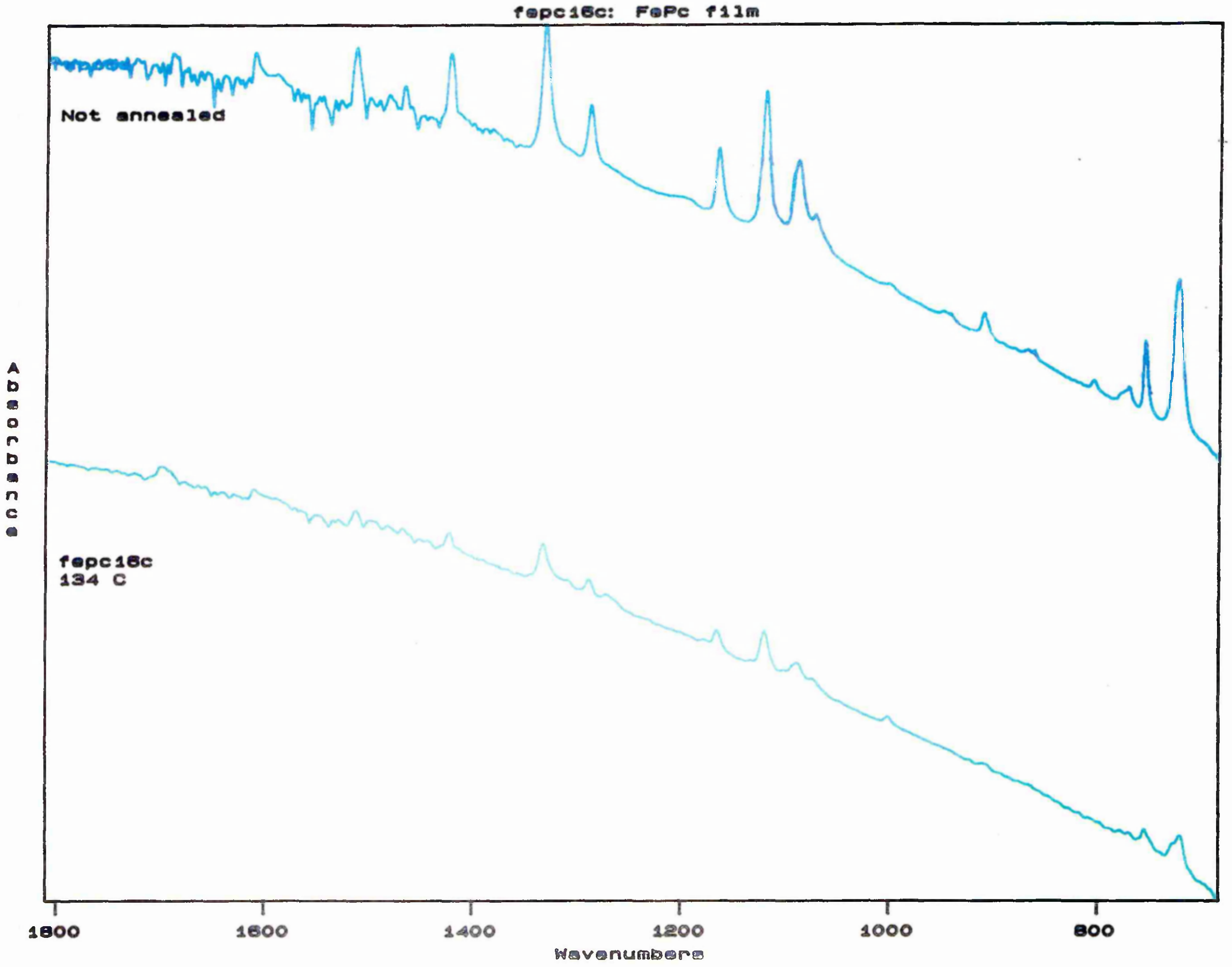

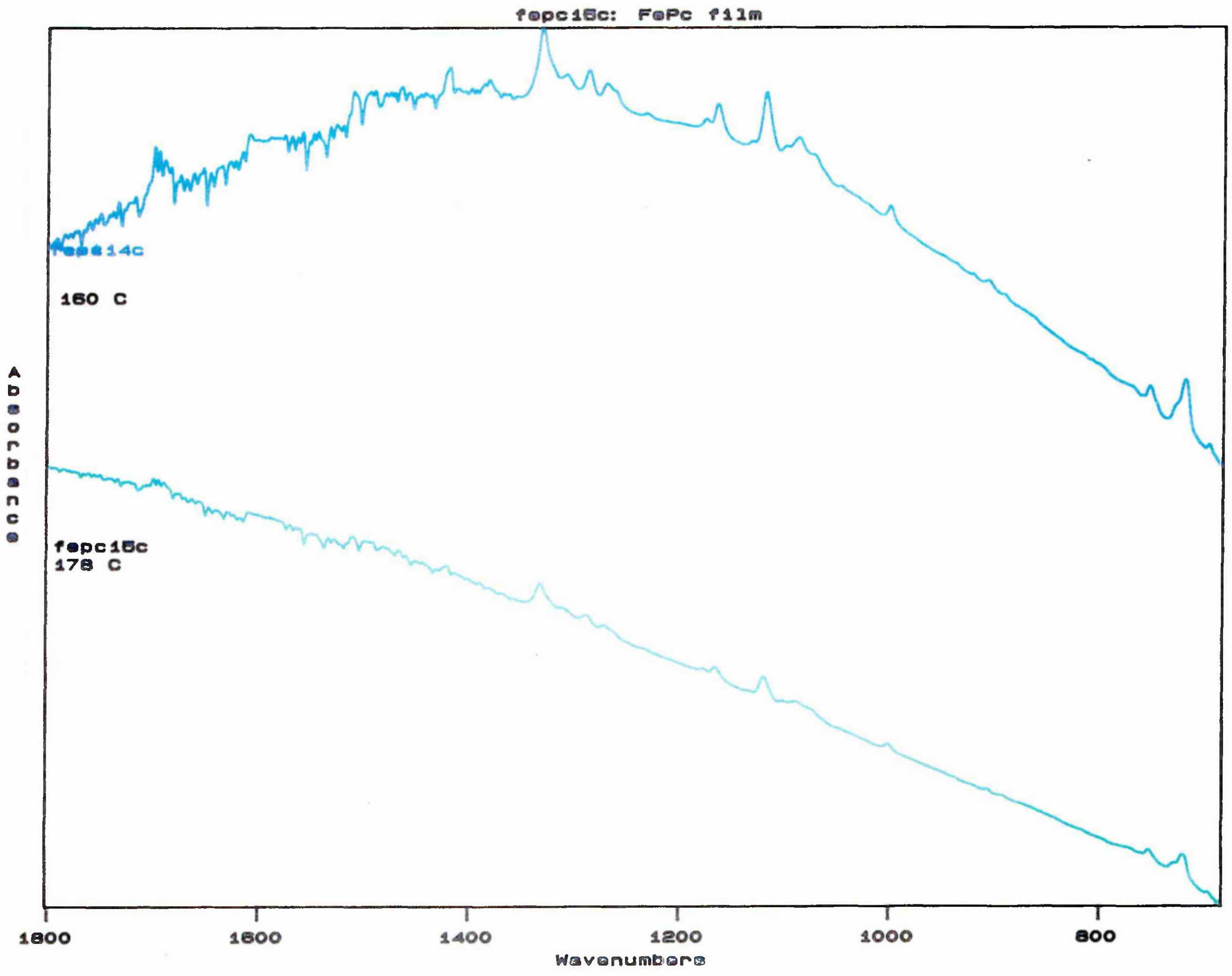

Figure 5.2 Sample annealed in air at 160°C (top) and 178°C (bottom) for 3 hours.

Figure 5.3 Sample annealed in air at 205°C (top) and 220°C (bottom) for 3 hours.

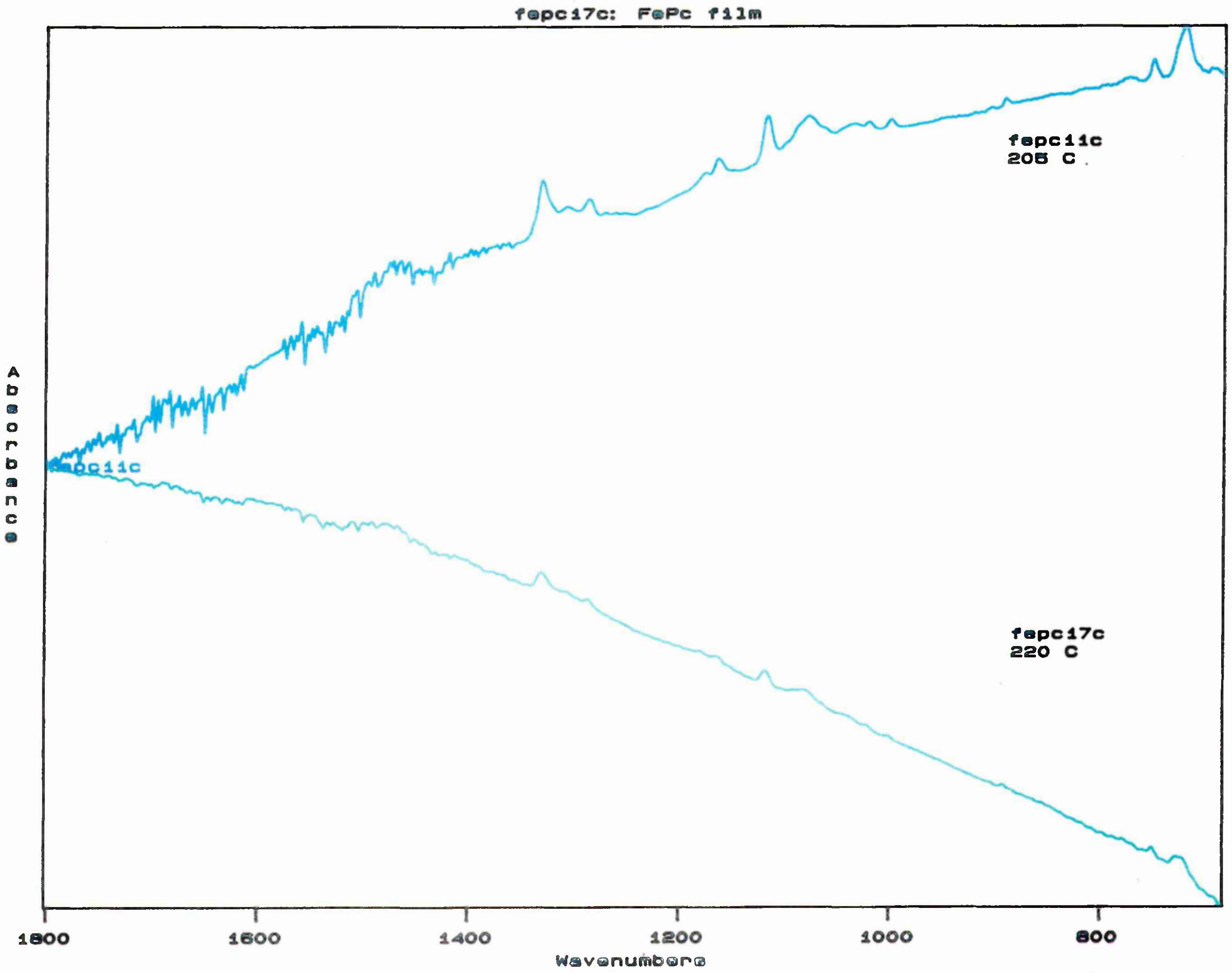

Figure 5.4 Sample annealed in air at 249°C (top) and 292°C (bottom) for 3 hours.

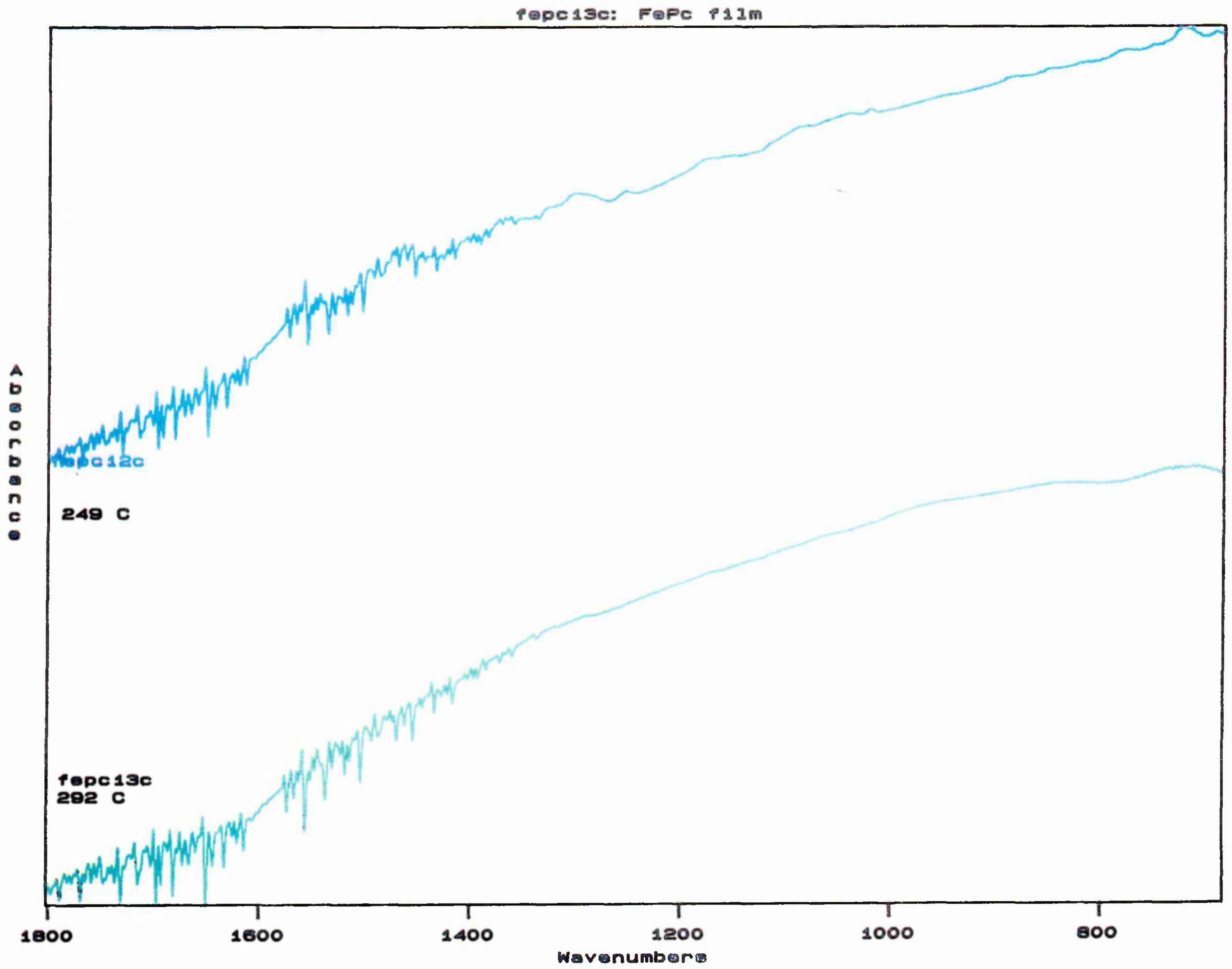

both crude Pfaltz and Bauer FePc and beta FePc (originating from a Pfaltz and Bauer sample). Table 5.1 gives the IR bands for these four films compared with the literature data for an alpha FePc film.

Table 5.1 Infra-red bands of FePc deposited on substrates at different temperatures.

Sample	IR bands cm^{-1}
JOR1 Cold stage crude FePc	695s, 722s, 755s, 771m, 804w, 870w, 910m, 949w, 1071w, 1087m, 1119s, 1165m, 1288m, 1332m, 1429m, 1469w, 1515m
JOR2 No cold stage crude FePc	706s, 723s, 755s, 771m, 909m, 949w, 1069w, 1086w, 1119s, 1164m, 1288w, 1332m,1429w, 1519w
JOR3 Cold stage pure FePc	722s, 755s, 771m, 909m, 949w, 1072w, 1088m, 1120s, 1165s, 1286m, 1332s, 1423s, 1469w, 1514m
JOR4 No cold stage pure FePc	715s, 755s, 771m, 870w, 909m, 949w, 1071w, 1087m, 1119s, 1165m, 1286m, 1331s, 1422m, 1469w, 1514m
α - FePc (2)	665w, 725s, 770m, 805w, 865w, 910m, 950w, 1060m, 1085s, 1120s, 1165s, 1285s, 1330s, 1425s, 1470m, 1515s

w = weak, m = medium, s = strong

The IR bands show that the four films are all alpha phase FePc films. It was not possible to investigate the phase produced when the films were sublimed on to heated substrate owing to lack of equipment.

5.2 USE OF SCANNING ELECTRON MICROSCOPY TO MONITOR THE HEAT TREATMENT OF FePc FILMS

Scanning electron microscopy (SEM) has been used to distinguish between the alpha and beta phases of the phthalocyanines (3, 4). Annealing the alpha film should result in the beta form (1). SEM was used to examine the morphology of FePc films after heat treatment at various temperatures in air, in an attempt to compare the alpha and beta morphologies. Aluminium SEM stubs were mounted on a rotating carousel in the Edwards coater. Beta FePc crystals (originating from crude laboratory prepared FePc) were placed in the quartz crucible and 500nm alpha FePc films were deposited.

The Phillips XL40 SEM was used to monitor the morphology of the films before and after annealing in air. To improve the image quality the films were each coated with a thin layer of conducting material. Gold was used and the image was greatly improved. Table 5.2 contains the results obtained at each temperature examined.

Table 5.2 SEM results using the Phillips XL40.

Sample conditions	Description
FePc as deposited (figure 5.5).	Small microcrystalline particles. The film is oriented so that the rod like crystals are seen end on. End diameter 0.1µm.
FePc annealed at 260°C in air.	Same as above.
FePc annealed at 275°C in air.	Some slightly bigger microcrystals are seen interdispersed through the surface. Diameter of larger microcrystals 0.2µm.
FePc annealed at 290°C (figure 5.6) and 300°C in air.	Same as at 275°C.
FePc annealed at 359°C and 380°C (figure 5.7) in air.	Surface changes quite dramatically, the microcrystals appear to merge together in clumps. Clump size 1-2µm.

Figures 5.5 - 5.7 show the micrographs obtained at a variety of temperatures using the XL40.

The XL30 FEG in Bern was used to obtain another set of scanning electron micrographs.

Figure 5.5 Pure FePc as deposited (XL40). Magnification 30000X.

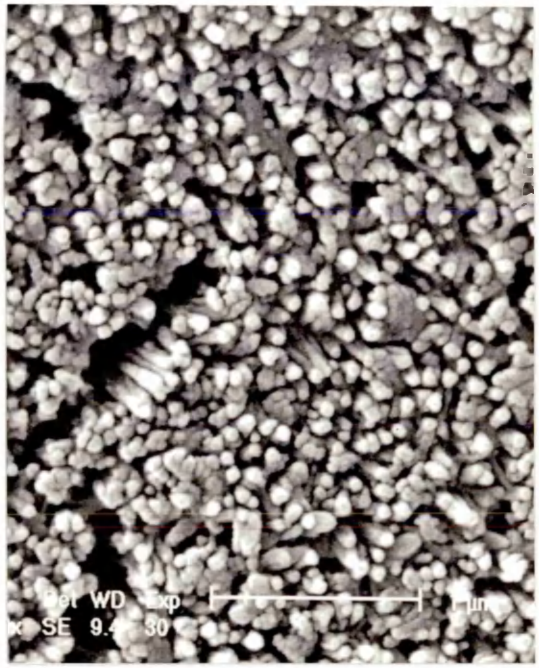

Figure 5.6 Pure FePc annealed in air at 290°C (XL40). Magn. 30000X.

Figure 5.7 Pure FePc annealed in air at 380°C (XL40). Magn. 30000X.

It was not necessary to gold coat the samples since the images produced without coating were of excellent quality. Table 5.3 contains the SEM results of the annealed samples from pure FePc using the XL30 FEG, the micrographs can be seen in figures 5.8 - 5.11.

Table 5.3 Results from the XL30 FEG.

Sample conditions	Description
Pure FePc as deposited - RT (figure 5.8).	Sharp angular crystallites, tips translucent, aligned in varying directions. Width 0.1μm (approx.).
Pure FePc annealed at 134°C in air.	Same as at RT.
Pure FePc annealed at 160°C in air.	Some slightly larger microcrystallites appearing, and the smaller ones appear to have blunter, curved ends. Width 0.15μm (approx.).
Pure FePc annealed at 178°C in air.	Same as 160°C.
Pure FePc annealed at 205°C in air (figure 5.9).	Some larger crystallites dispersed throughout the surface. Again the smaller crystallites are not as pointed as they were at RT. Width of large crystallites - 0.2μm (approx.).
Pure FePc annealed at 220°C in air.	Crystallite size over the area seems more uniform 0.05 - 0.1μm. The crystallites are not as sharp and angular as at RT.
Pure FePc annealed at 249°C in air (figure 5.10).	The crystallites have begun to merge together and are very curvy. Small gaps have been left in the surface.
Pure FePc annealed at 292°C in air (figure 5.11).	The surface has changed quite dramatically, the crystallites have merged together in clumps.

Table 5.4 contains SEM results of annealed samples originating from crude FePc along with samples sublimed onto substrate held at different temperatures using the XL30 FEG. The micrographs can be seen in figures 5.12 - 5.17.

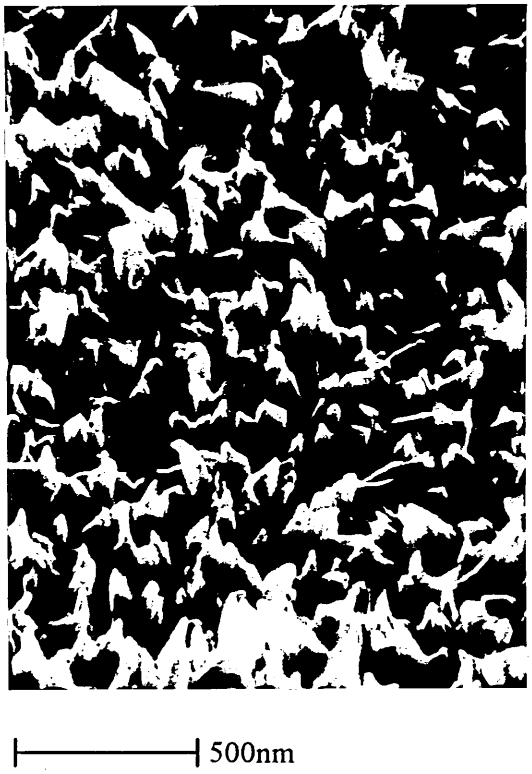

Figure 5.8 Pure FePc as deposited (XL30). Magnification 40000X.

Figure 5.9 Pure FePc annealed in air at 205°C (XL30). Magn. 40000X.

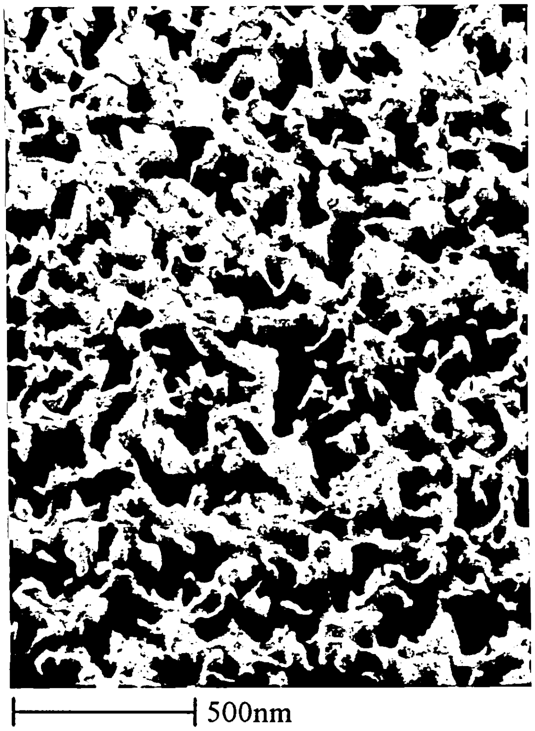

Figure 5.10 Pure FePc annealed in air at 249°C (XL30). Magn. 40000X.

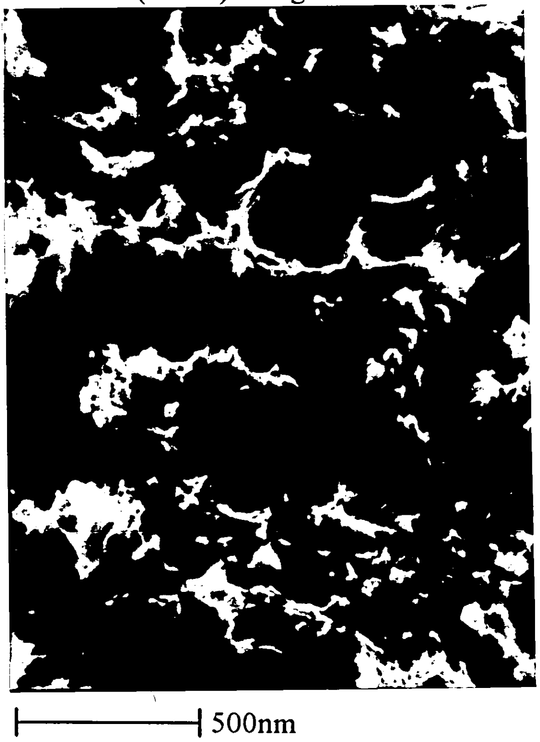

Figure 5.11 Pure FePc annealed in air at 292°C (XL30). Magn. 40000X.

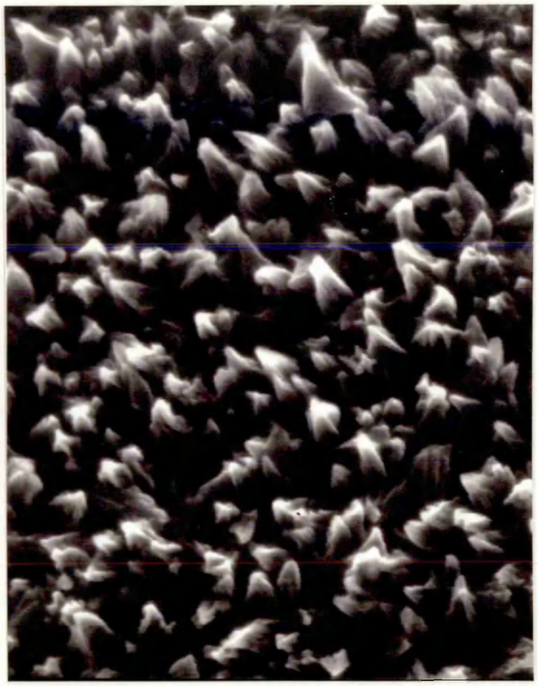

Figure 5.12 Crude FePc as deposited (XL30). Magnification 40000X.

Figure 5.13 Crude FePc annealed in air at 207°C (XL30). Magn. 40000X.

Figure 5.14 Crude FePc annealed in air at 249°C (XL30). Magn. 40000X.

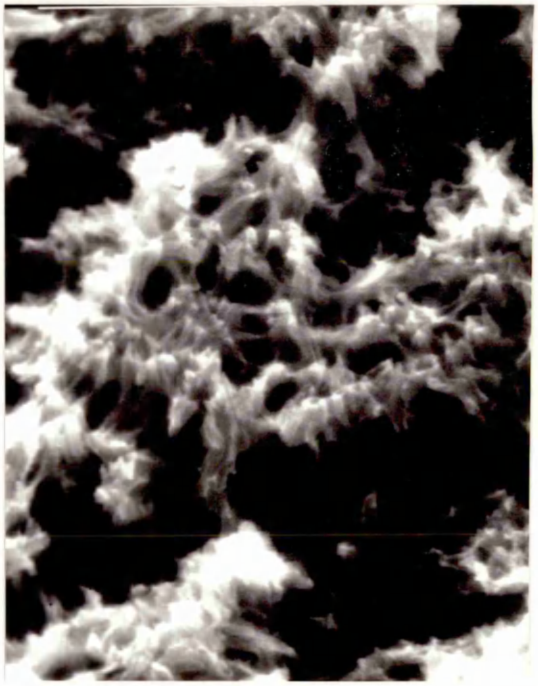

Figure 5.15 Crude FePc annealed in air at 292°C (XL30). Magn. 40000X.

Figure 5.16 Pure FePc, cold stage at RT (XL30). Magnification 40000X.

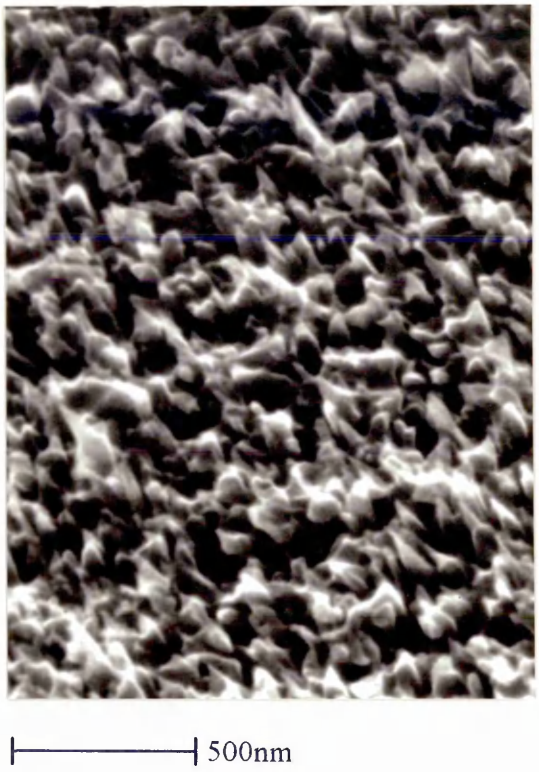

Figure 5.17 Crude FePc, cold stage at RT (XL30). Magnification 40000X.

Table 5.4 Results from the XL30 FEG.

Sample conditions	Description
Crude FePc as deposited - RT (figure 5.12).	Sharp well defined crystallites, no particular preferred orientation. Width 0.05 - 0.1µm (approx.).
Crude FePc annealed at 175°C in air.	Similar to that observed at RT with a few larger crystallites appearing. Width of larger crystallites 0.15µm (approx.).
Crude FePc annealed at 207°C in air (figure 5.13).	Similar to 175°C but crystallites are less sharp.
Crude FePc annealed at 249°C in air (figure 5.14).	Crystallites appear to start merging together some gaps are seen.
Crude FePc annealed at 292°C in air (figure 5.15).	Crystallites have merged together in clusters.
Pure FePc - Cold stage RT (figure 5.16).	The crystallites appear to be aligned in mainly one direction.Width 0.05 - 0.1µm (approx.). The crystallites are less sharp and generally smaller than the same sample deposited without the cold stage (figure 5.8).
Crude FePc - Cold stage RT (figure 5.17).	Similar to above.

The startling difference between the micrographs obtained from the coated and uncoated films can be seen by comparing the as-deposited pure FePc films in figures 5.5 (XL40) and 5.8 (XL30). Although the magnifications differ it can be seen that the uncoated crystals examined using the XL30 FEG were sharp and pointed whereas the coated films viewed with the XL40 were very different showing smaller spherical crystallites. There was not a difference in subliming crude or pure FePc on to the substrate followed by annealing, which is not surprising since the process of sublimation on to a substrate should also be a purification. The FePc film from deposition on to a cold stage and as-deposited film differ. The cold stage deposited sample showed alignment in one direction rather than no particular direction, as in the as-deposited samples.

Although there is a large difference in the SEM micrographs from both instruments, both sets of micrographs show that as the temperature is increased the microcrystallites experience growth and at higher temperatures they merge together in clusters or clumps. The results from the XL30 FEG would appear to be most reliable since the samples do not have a gold coat and these show that a phase change may start occurring at about 205°C which also supports the infra-red results. The infra-red results indicate that the material decomposes at 249°C which would support the SEM image produced at 249°C when the microcrystallites merge together in clusters.

5.3 GAS SENSING WORK

Gas sensing work has been carried out to determine whether FePc has a response to nitrogen dioxide or chlorine. If a response is found FePc can be used as a model in an attempt to study the changes occurring upon exposure to a gas using Mössbauer spectroscopy.

The sensor consisted of an alumina substrate with an interdigitated electrode pattern on one face and a platinum heater on the other, commercially available from Rosemount Plc (5). The dimensions of the substrate are 3mm square and 0.5mm thick. A schematic diagram of the Rosemount can be seen in figure 5.18. The Rosemount was mounted by soldering onto a four-pin transistor header and then placed in the Edwards coater. FePc films of 500nm thickness were vacuum sublimed on to the electrode pattern (Figure 5.19). The gas sensor rig used at the Health and Safety Executive is shown in figure 5.20. The sensor was placed in a circuit shown schematically in figure 5.21. A constant voltage of 2V is supplied by means of a potentiometer. Upon exposure to a gas any change in resistance across the sensor is detected by a change in the current.

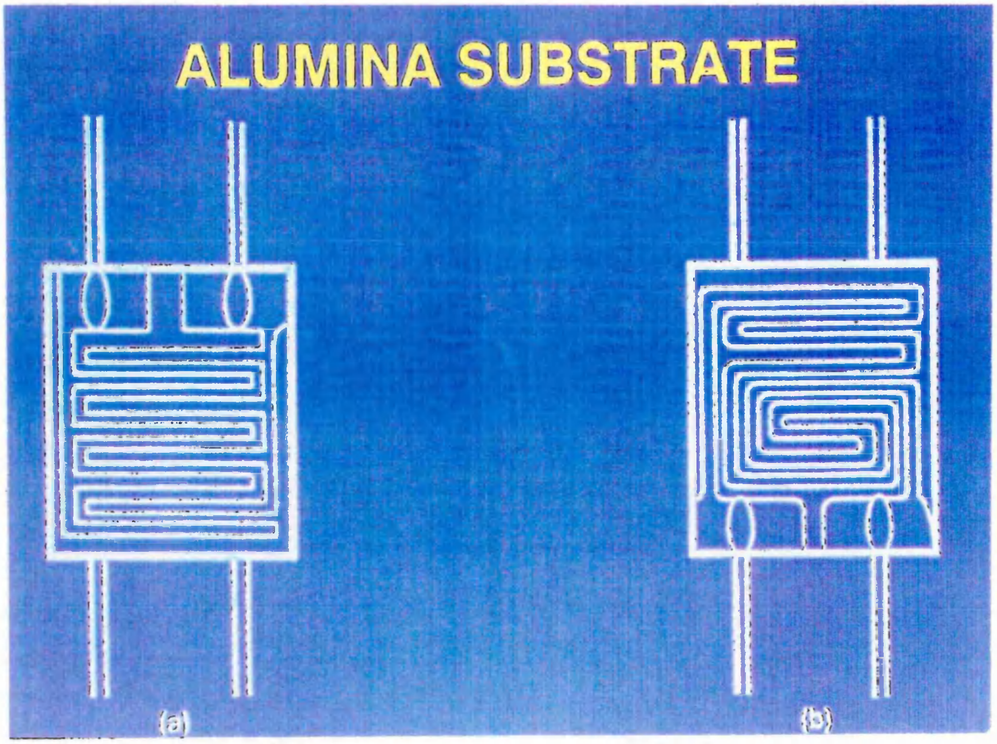

Figure 5.18 Schematic diagram of a Rosemount with an interdigitated electrode pattern on one face (a) and a platinum heater on the other face (b).

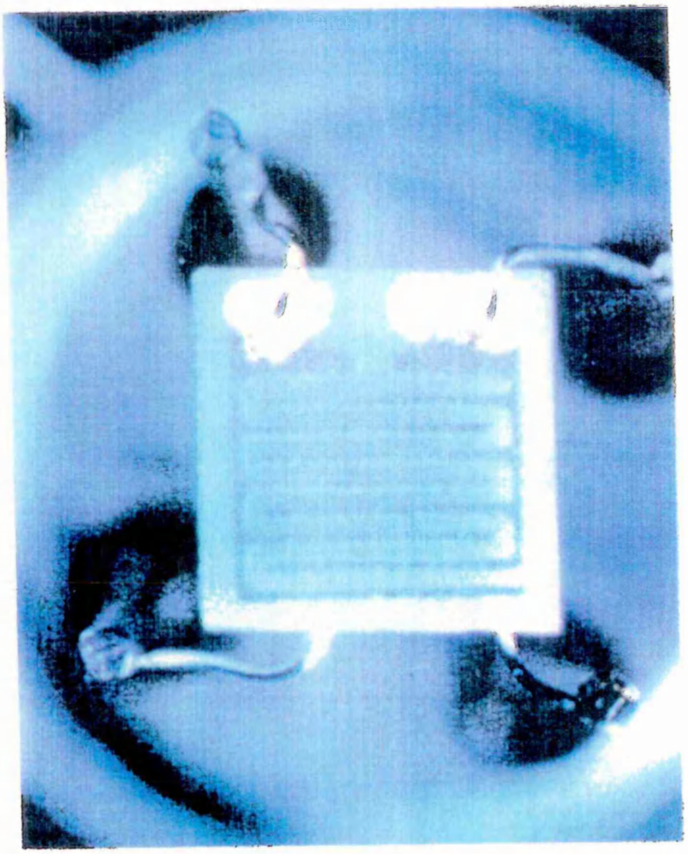

Figure 5.19 FePc film vacuum sublimed onto a Rosemount.

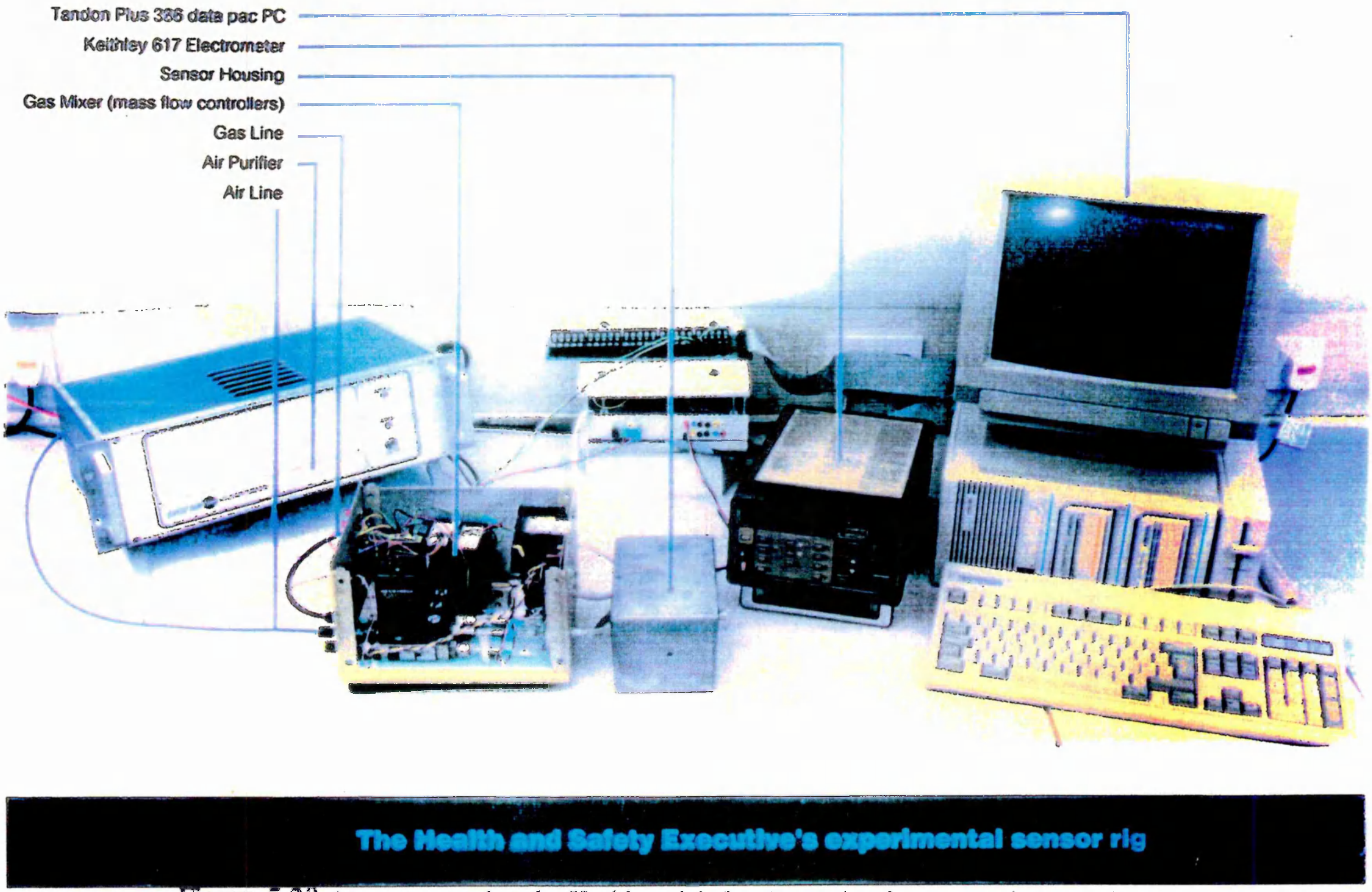

Figure 5.20 Apparatus used at the Health and Safety Executive for gas sensing experiments.

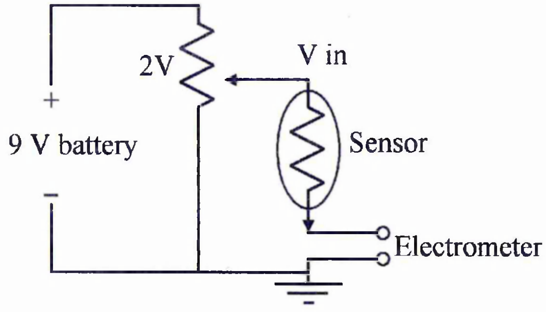

Figure 5.21 Schematic diagram of the sensor circuit.

The sensor was exposed to 2 minutes of air, followed by two minutes of gas and this pattern was repeated. The results of the gas exposure experiments were plotted as conductance (calculated from change in current) against time of sensing, in air and gas. The alpha FePc film was exposed to 1-5ppm nitrogen dioxide (NO_2), 3ppm NO_2 and 5ppm NO_2. Figure 5.22 shows the exposure to 1-5ppm NO_2. An increase in conductance as the concentration of NO_2 increases can be seen. The response is fast and approximately exponential. The recovery is also fast but it does not recover to the original starting point so an increase in base level can be seen throughout the experiment.

Upon repeated exposures to 3ppm (figure 5.23), and 5ppm (figure 5.24) NO_2, the response and recovery characteristics were the same as for 1-5ppm NO_2. These two experiments illustrate the reproducibility of the conductance response upon repeated exposure to the same concentration.

Exposing the alpha FePc film to 9ppm Cl_2 (figure 5.25) gave the opposite effect. There was a decrease in conductance and the response was fast as was the recovery but the baseline decreased with time.

NO_2 and Cl_2 are both electron-acceptor gases and FePc acts as a p-type semiconductor with NO_2, which is the expected behaviour of pure phthalocyanines (6). The decrease in conductance upon exposure of alpha FePc to Cl_2 is surprising as it was expected that NO_2 and Cl_2 would have the same effect on FePc. FePc acts as an n-type semiconductor in the presence of Cl_2. This effect has been seen previously by workers at the Health and Safety Executive and the presence of water vapour on the material was thought to be the cause which could also be the case at present. The gas sensing experiments have demonstrated that FePc responds with a change in conductance upon exposure to NO_2 and Cl_2. These results allow FePc to be considered not as a good sensor but as a model to examine chemical or physical changes occurring when a gas sensor is exposed to a gas.

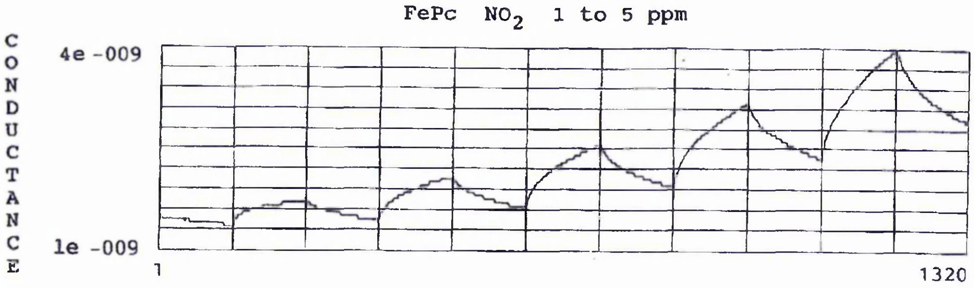

Figure 5.22 Exposure of FePc film to 1-5ppm NO_2.

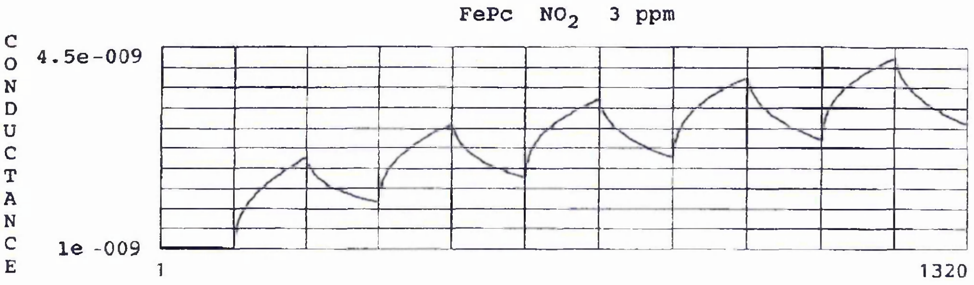

Figure 5.23 Repeated exposure of FePc film to 3ppm NO_2.

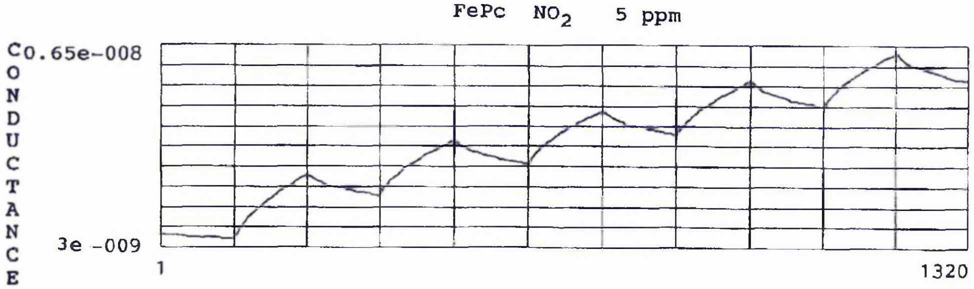

Figure 5.24 Repeated exposure of FePc film to 5ppm NO_2.

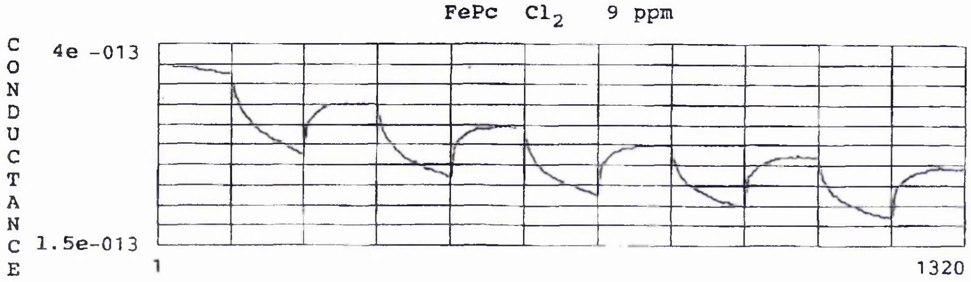

Figure 5.25 Repeated exposure of FePc film to 9ppm Cl_2.

5.4 MÖSSBAUER SPECTROSCOPY

Phthalocyanines have been noted for their use as gas sensors (7, 8, 9). Iron phthalocyanine can be used as a model in an attempt to elucidate the gas sensing mechanism and to study chemical changes which occur. The advantages of Mössbauer spectroscopy compared with other surface sensitive techniques for this work is that it can be used at ambient temperatures and pressures hence mimicking sensor operation conditions. The aim of this work has been to study the gas sensing behaviour of iron phthalocyanine using Mössbauer spectroscopy. Transmission Mössbauer spectroscopy was used to gain information relating to the bulk of the sample. A transmission variable temperature study was completed to obtain information about vibrational states of the material and hence the Debye temperature. The recoil free fraction was calculated from the Debye temperature and gave an indication of the amount of absorption to be expected from the material. Backscatter Mössbauer spectroscopy was used to study the surface of iron phthalocyanine before, during, and after exposure to a gas in an attempt to observe any physical or chemical surface changes.

5.4.1 Transmission Mössbauer Spectroscopy

The spectrometer was calibrated using enriched ^{57}Fe foil. The source, ^{57}Co in a rhodium matrix, was kept at room temperature for all experiments. The velocity range used was ± 5mm/s. The spectra obtained were computer fitted by a least squares method using Lorenzian lineshapes. Alpha and beta FePc samples were cooled to 80K using the liquid nitrogen cryostat, and transmission spectra collected. Figures 5.26 and 5.27 show the spectra of the alpha and beta form respectively. Table 5.5 contains the Mössbauer parameters for these phases at 80K and a comparison with those found in the literature. Comparing the parameters of the samples made in the laboratory to those found in the literature shows good agreement. These results confirm that the samples are alpha and beta iron phthalocyanine. The spectra of both phases show a single quadrupole doublet typical of iron (II) character. Both phases exhibit asymmetry. The relative individual line intensities of alpha and beta FePc are given in table 5.6.

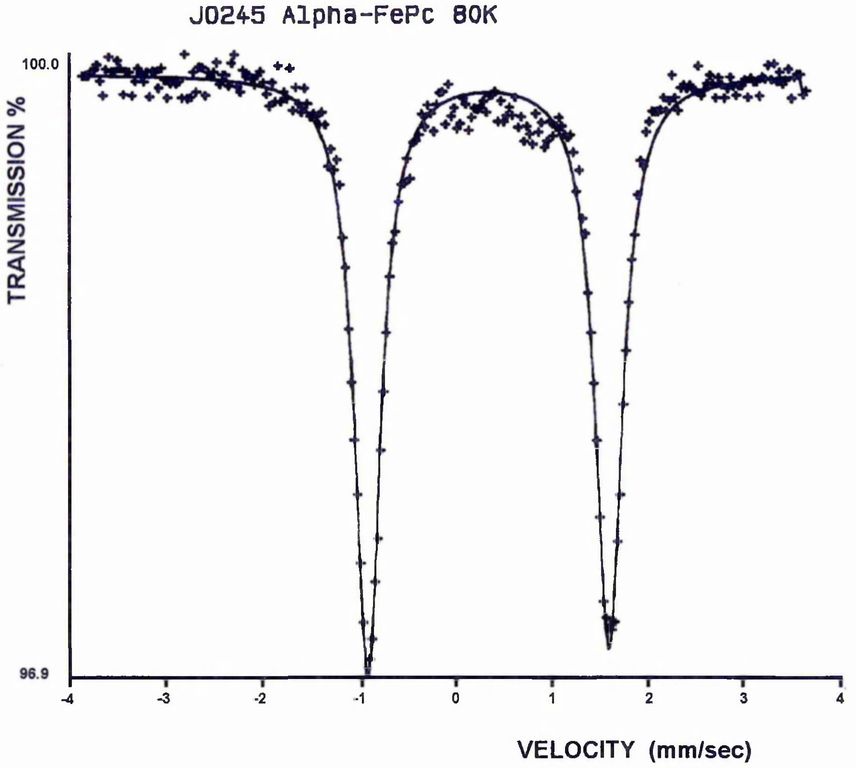

Figure 5.26 Transmission Mössbauer spectrum of alpha FePc at 80K.

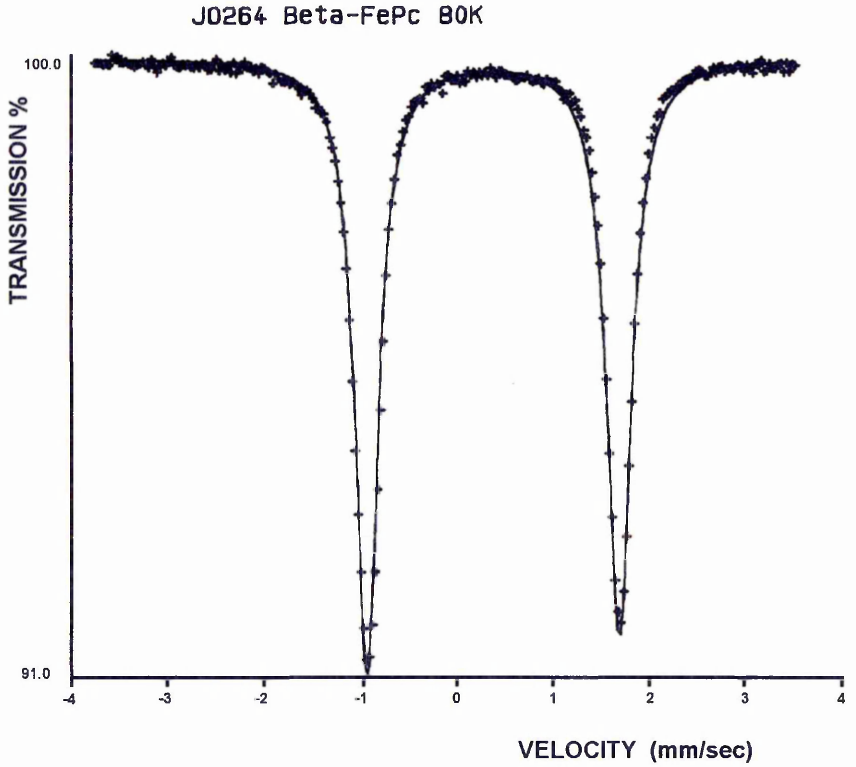

Figure 5.27 Transmission Mössbauer spectrum of beta FePc at 80K.

TABLE 5.5 Transmission Mössbauer parameters of α and β-FePc at 80K.

Temp (K)	Sample	Isomer shift δmm/s (α-Fe)	Quadrupole splitting Δmm/s	Ref.
80	α-FePc	0.46 ± 0.02	2.50 ± 0.02	This work
80	α-FePc	0.46 ± 0.01	2.49 ± 0.01	10
77	α-FePc	0.44	2.46	2
80	β-FePc	0.49 ± 0.02	2.62 ± 0.02	This work
80	β-FePc	0.48 ± 0.01	2.68 ± 0.02	10
80	FePc	0.48	2.63	11
80	FePc	0.48 ± 0.02	2.60 ± 0.02	12
80	FePc	0.51 ± 0.02	2.62 ± 0.02	9

Table 5.6 Line intensities of α and β-FePc before grinding.

Sample	Left line %	Right line %	Difference %
β-FePc	100	93	7
α-FePc	100	96	4

The asymmetry effect is greater in the beta phase. In order to determine whether the asymmetry was a result of crystal orientation due to the crystal structure or a true Goldanski Karyagin effect (a truly randomly orientated polycrystalline material) the following experiment was carried out. Two samples of beta FePc from the same batch were taken, one was mixed with graphite and placed in a sample holder and the other sample ground up using a pestle and mortar for a few minutes until the sample looked like a random powder rather than the original needle-like crystal appearance. Figures 5.28 and 5.29 show the transmission Mössbauer spectra at K before and after grinding respectively. Table 5.7 shows the relative individual line intensities of the beta phase before and after grinding.

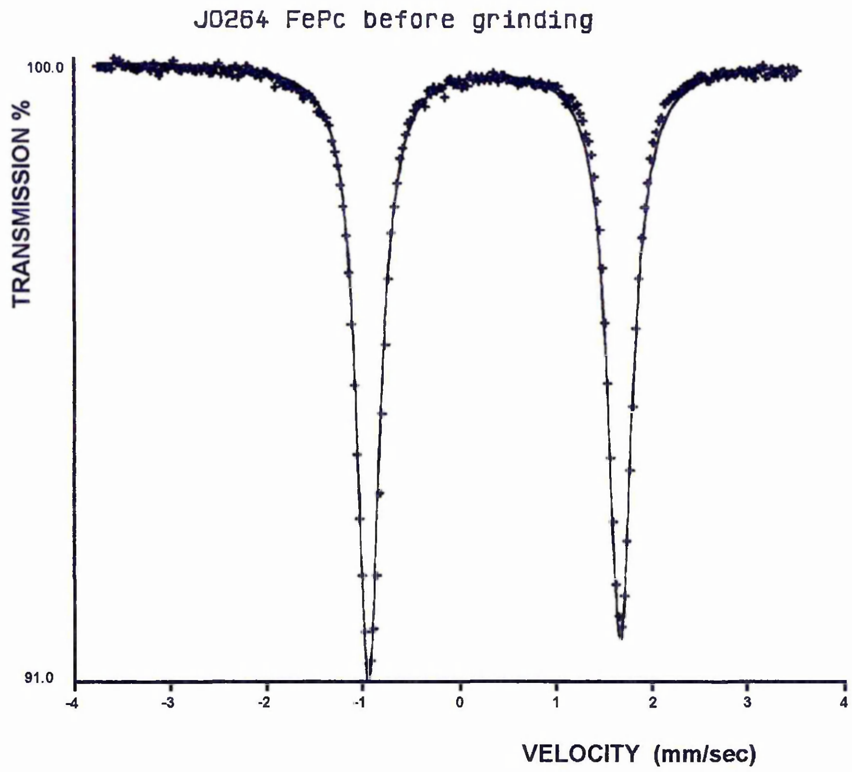

Figure 5.28 Transmission Mössbauer spectrum of FePc before grinding at K.

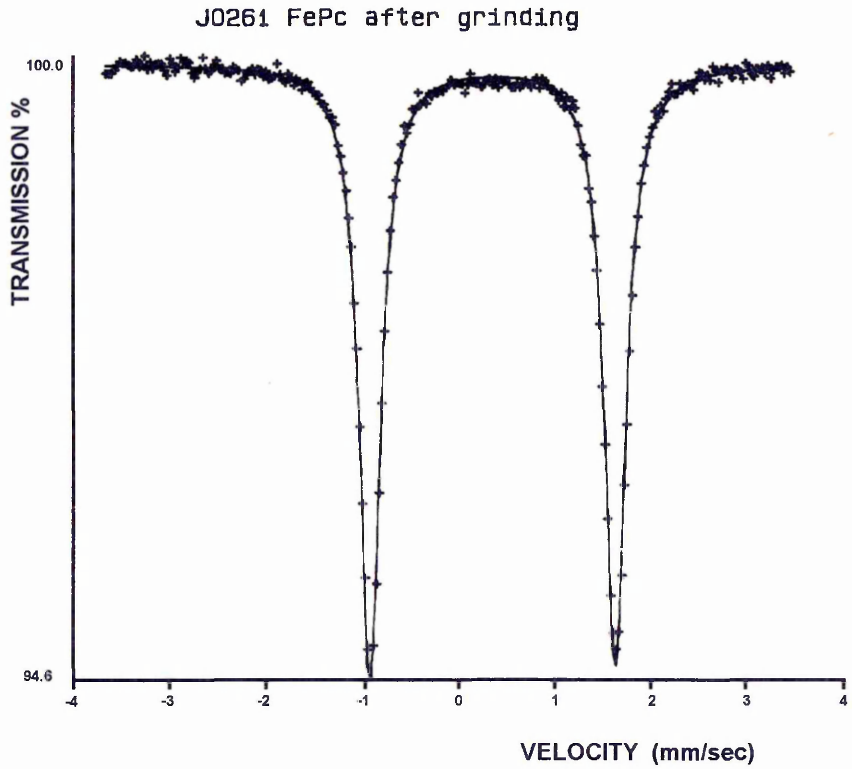

Figure 5.29 Transmission Mössbauer spectrum of FePc after grinding at K.

TABLE 5.7 Line intensities of α and β-FePc after grinding.

Sample	Left line %	Right line %	Difference %
β-FePc Before grinding	100	93	7
β-FePc After grinding	100	97	3

The difference in line intensity of beta FePc after grinding has decreased to 3% showing a decrease in the asymmetry of the lines. This decrease indicates that the asymmetry is a result of crystal orientation. The greater asymmetry of the beta phase compared to the alpha phase is due to the beta phase consisting of thin needle-like crystals whilst the alpha phase is a powder.

5.4.2 Transmission Variable Temperature Study

Preliminary investigations using conversion electron Mössbauer spectroscopy showed that collection of a room temperature spectrum from an FePc film was not possible (see section 5.4.3). One possible reason for this was a low recoil free fraction for the alpha phase. This led to a transmission variable temperature Mössbauer study. This variable temperature was completed in an attempt to explain these difficulties by obtaining the Debye temperatures and hence calculating the recoil free fractions of the different phases of FePc at room temperature. Variable temperature experiments were carried out using alpha powder and beta crystals of FePc. The alpha and beta FePc samples were prepared in the laboratory and purified using the cold finger apparatus (chapter 4). The amount of FePc used as a sample was calculated using equation 5.1 to ensure that the optimum Mössbauer thickness was used (see chapter 3).

$$t=\beta n f \sigma \tag{5.1}$$

80mg of sample was mixed with high purity graphite, placed in a sample holder and inserted in the liquid nitrogen cryostat for cooling to specific temperatures between 298K and 80K. The spectrometer was calibrated using enriched ^{57}Fe foil. The ^{57}Co source in a rhodium matrix was maintained at room temperature for all experiments. The source, absorber and detector geometry was secured with tape to ensure physical stability during the variable temperature study since absolute absorption data were to be recorded. The velocity scale was ± 5mm/s. Spectra were accumulated until a significant absorption was detected, which required runs of up to 30 hours at room temperature. The window of the pulse height analyser was checked between collection of each spectrum and adjusted to ensure the 14.4KeV γ-ray was isolated centrally and a standard window set. Figure 5.30 shows some of the Mössbauer spectra obtained for the alpha phase and figure 5.31 some for the beta form. The Mössbauer parameters for both phases are given in table 5.8. At all temperatures the spectra of both phases consisted of a single quadrupole doublet of iron (II) character. The asymmetry is a result of partial crystal orientation effects. The isomer shift (δ) values occur between high values characteristic of high spin and the lower values characteristic of low spin ferrous ion (14). The quadrupole splittings (Δ) are characteristic of high spin ferrous ion (14).

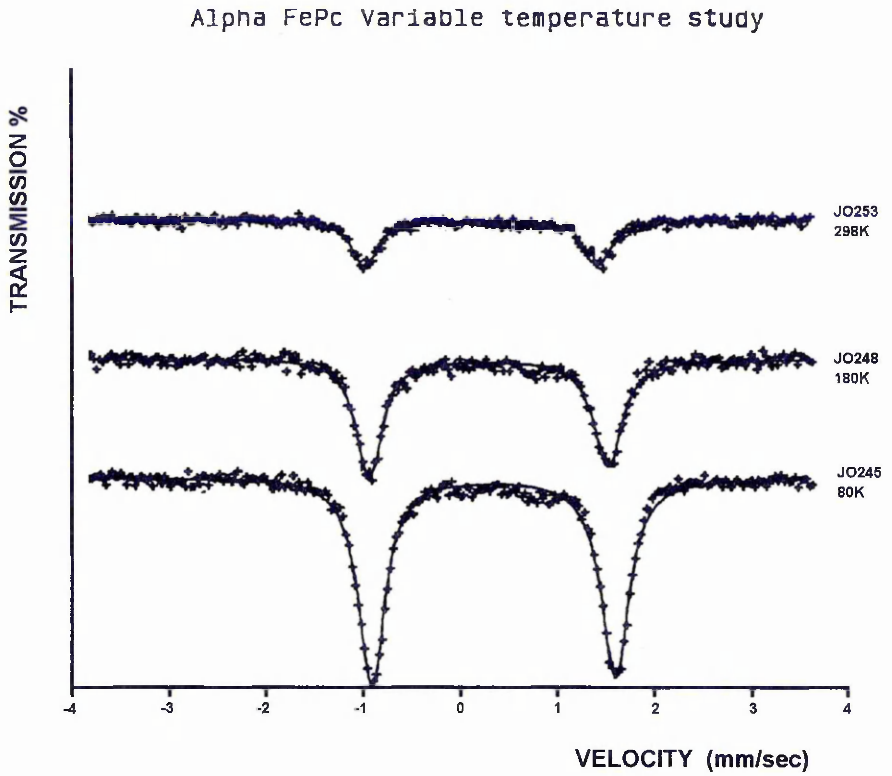

Figure 5.30 Transmission Mössbauer spectra of alpha FePc at various temperatures.

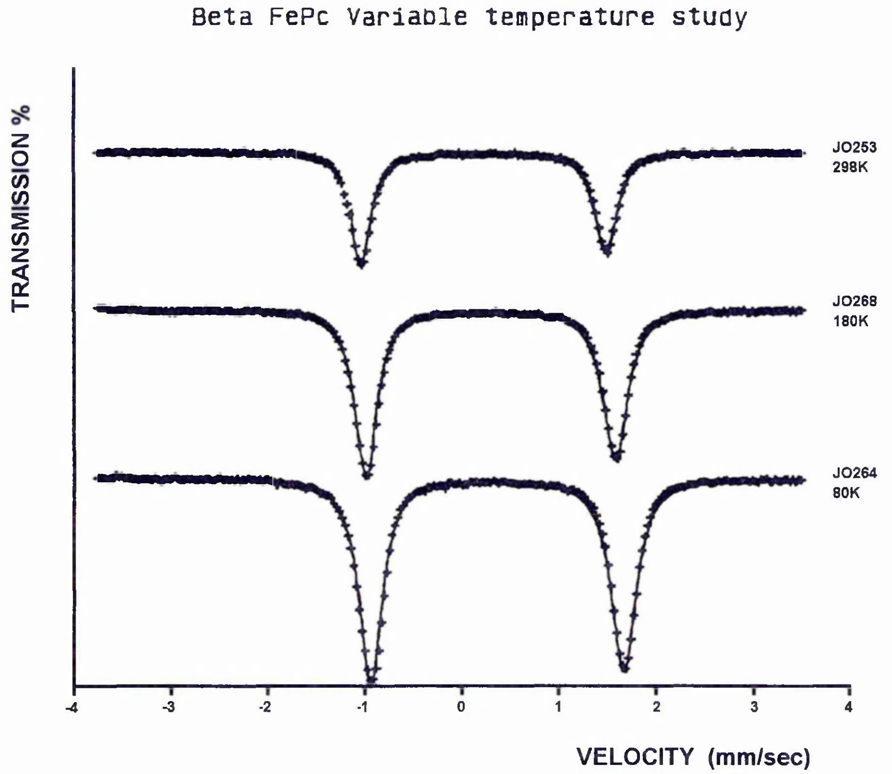

Figure 5.31 Transmission Mössbauer spectra of beta FePc at various temperatures.

TABLE 5.8 Transmission variable temperature Mössbauer parameters of α and β-FePc.

Temp (K)	Alpha FePc		Beta FePc	
	δmm/s (α-Fe) ± 0.02mm/s	Δmm/s ± 0.02mm/s	δmm/s (α-Fe) ± 0.02mm/s	Δmm/s ± 0.02mm/s
80	0.46	2.50	0.49	2.62
100	0.45	2.49	0.49	2.57
125	0.45	2.50	0.47	2.56
150	0.43	2.47	0.46	2.55
180	0.42	2.45	0.43	2.58
210	0.41	2.43	0.42	2.55
240	0.39	2.40	0.40	2.55
270	0.37	2.39	0.39	2.55
298	0.35	2.39	0.37	2.53

The isomer shift and quadrupole splitting vary smoothly with temperature for both phases. The interpretation of these temperature dependencies will be discussed later. These confirm the intermediate spin nature of FePc. The quadrupole splitting and isomer shifts of the beta form are greater than those of the alpha form and are a result of intermolecular interactions. The difference in structure between the alpha and beta phase is the angle at which the molecules are stacked (chapter 1, figure 1.7). In the beta form nitrogen atoms of neighbouring molecules are present in the octahedral positions above and below the central iron atom. In the alpha form nitrogens from the nearest neighbours do not form the nitrogen octahedron around the iron atom. The larger chemical shift of the beta form phase can be explained by visualising the π-electrons of the aromatic rings of the neighbouring molecules being delocalised through two axially substituted nitrogens above and below the central iron. This means enhanced shielding of the s-electrons by d-electrons and results in a decrease in the s-electron density at the iron nucleus and hence a larger chemical shift in the beta form than the alpha form. Figures

5.32 and 5.33 show the isomer shift against temperature graphs for the alpha and beta phases and figures 5.34 and 5.35 the quadrupole splitting against temperature for the alpha and beta phases respectively.

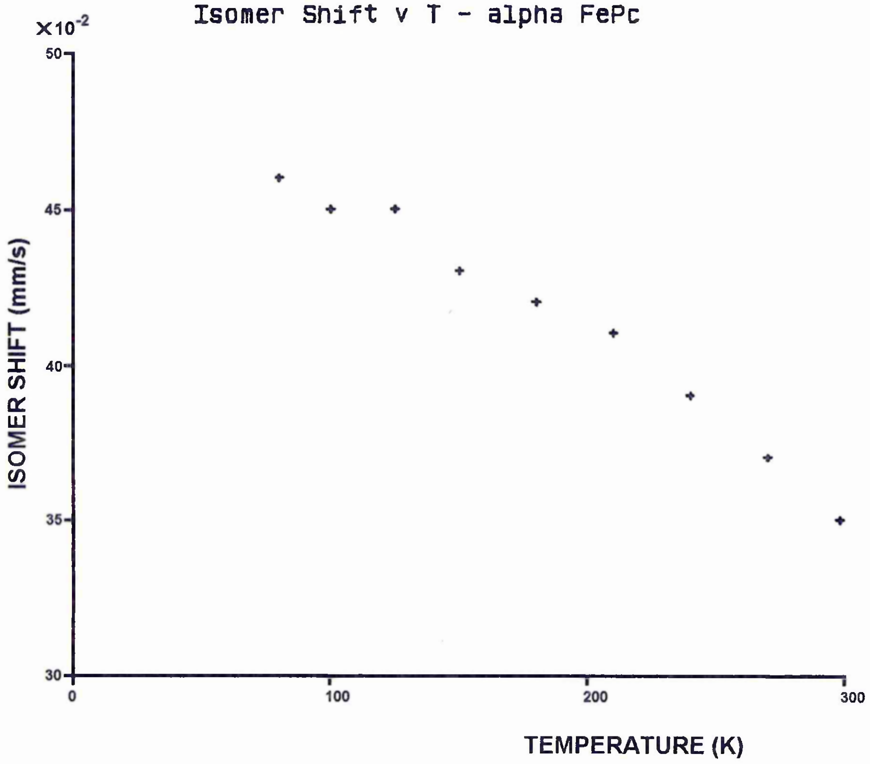

Figure 5.32 Isomer shift data against temperature for alpha FePc.

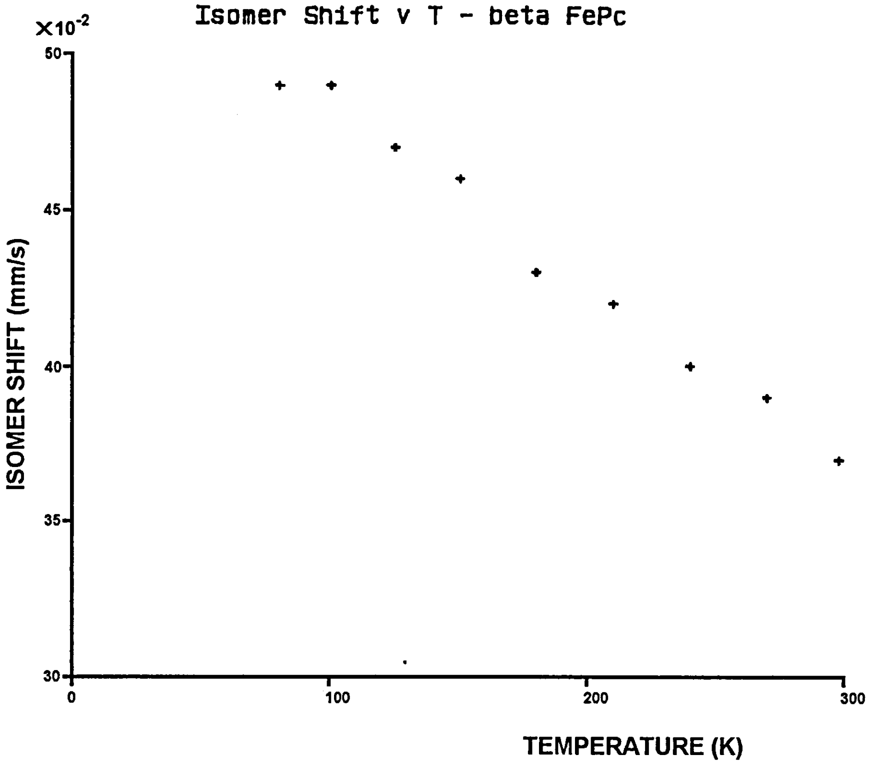

Figure 5.33 Isomer shift data against temperature for beta FePc.

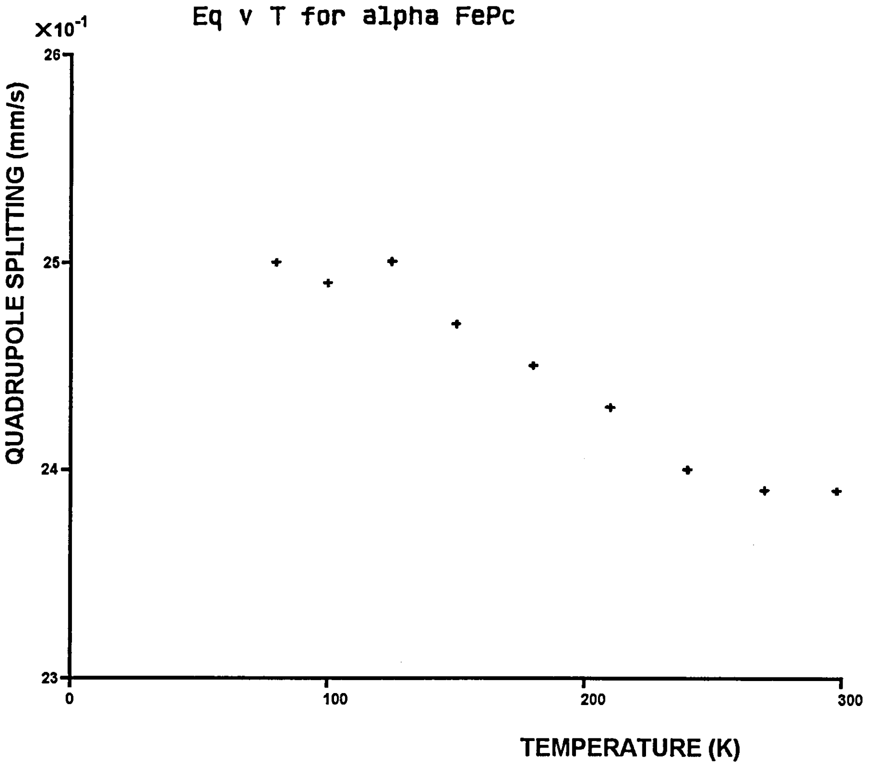

Figure 5.34 Quadrupole splitting against temperature for alpha FePc.

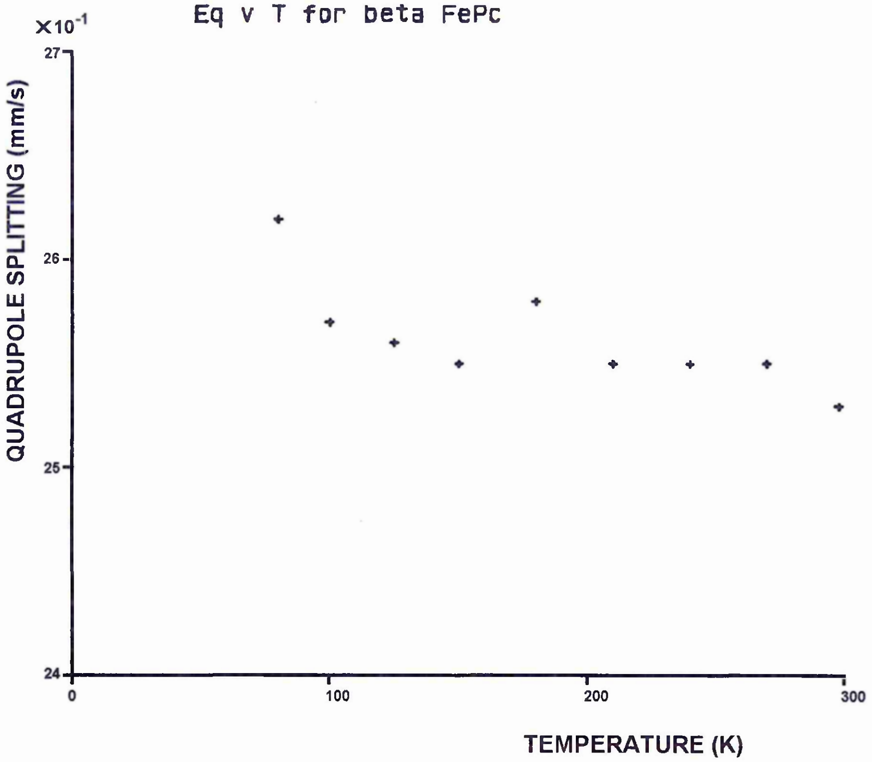

Figure 5.35 Quadrupole splitting against temperature for beta FePc.

5.4.2.1 Temperature Dependence of Area

The Debye temperature and hence the recoil free fraction (f) were calculated using a theoretical model (Chapter 3, section 3.6) fitted to the experimental data. The method involved the accurate measurement of the change in absorption line area with temperature. The method assumes that the vibrational properties of the sample can be represented by the Debye model of solids. Figures 5.36 and 5.37 show the ln-area versus temperature graphs for alpha and beta FePc. Table 5.9 contains the calculated Debye temperature (θ_D) and recoil free fraction (f) at 219K for both phases.

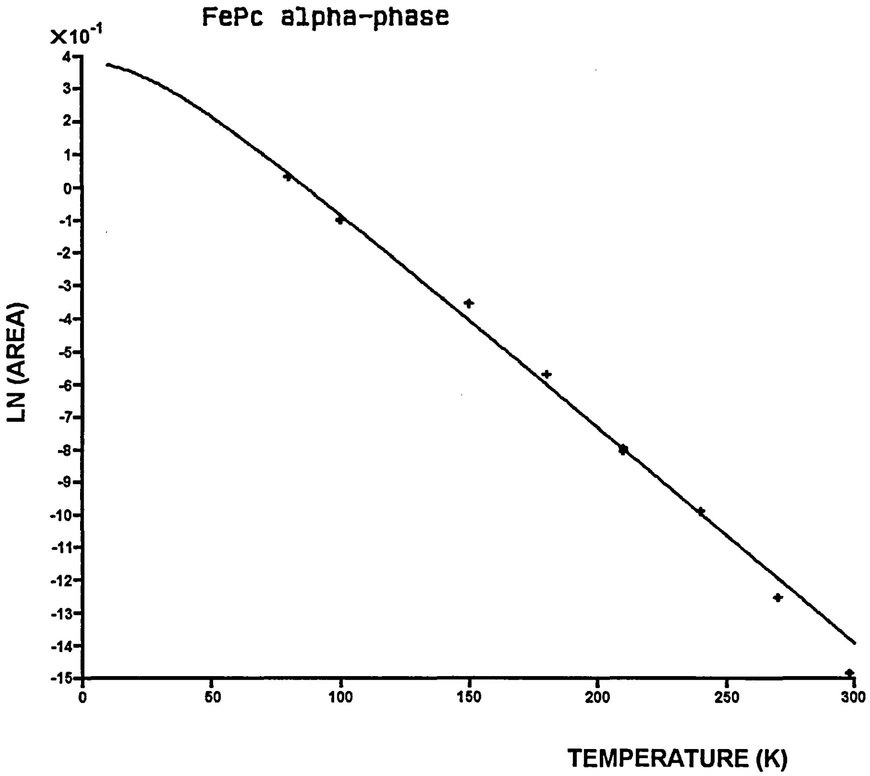

Figure 5.36 Ln-area data against temperature for alpha FePc.

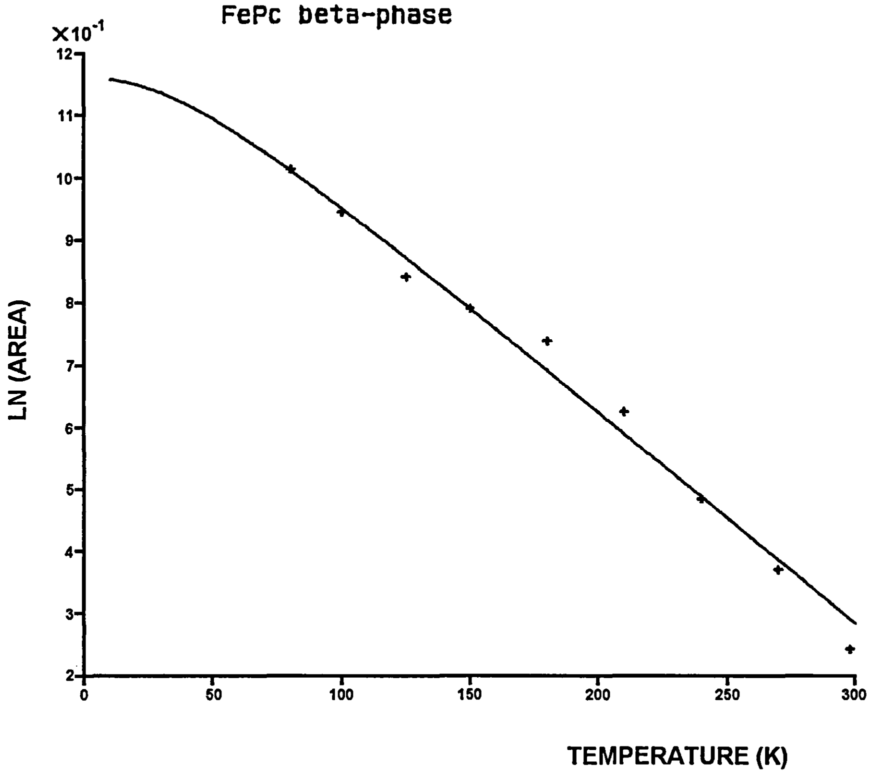

Figure 5.37 Ln-area data against temperature for beta FePc.

Table 5.9 Debye temperature and recoil free fraction for α and β-FePc using ln-area data.

Sample	θ_D (K)	f_{291K}
α-FePc	143	0.14
β-FePc	199	0.36

The recoil free fraction (f) can be expressed as:

$$f=\exp\left[\frac{-4\pi(X)^2}{\lambda^2}\right] \qquad (5.2)$$

where

$(x)^2$ = Mean square vibrational amplitude

λ^2 = Wavelength squared of the Mössbauer γ-ray

The difference in recoil free fraction is a result of a difference in mean square vibrational amplitude of the two phases and hence the rigidity of the lattice.

The f value is a measure of the probability of recoil events in the sample. The beta form has a higher recoil free fraction than the alpha phase. The higher f_{291K} value of the beta phase suggests that the structure is more rigid i.e. less free to vibrate in the lattice than the alpha phase. The results from the variable temperature study explain some of the difficulties in collection of a CEMS spectrum of the alpha FePc film at room temperature. The alpha phase has a low θ_D and hence f_{291K} value i.e. a low probability of recoil free events and it would not be expected to be easy to collect a CEMS spectrum. The results indicate that collection of backscatter spectra from the beta form should be possible.

5.4.2.2 Temperature Dependence of Isomer Shift

The isomer shift of the alpha and beta FePc versus temperature graphs can be seen in figures 5.38 and 5.39 respectively. The isomer shift data has been fitted to a Debye function using second order Doppler shift data (15). The resulting θ_D and f_{291K} parameters are listed in table 5.10.

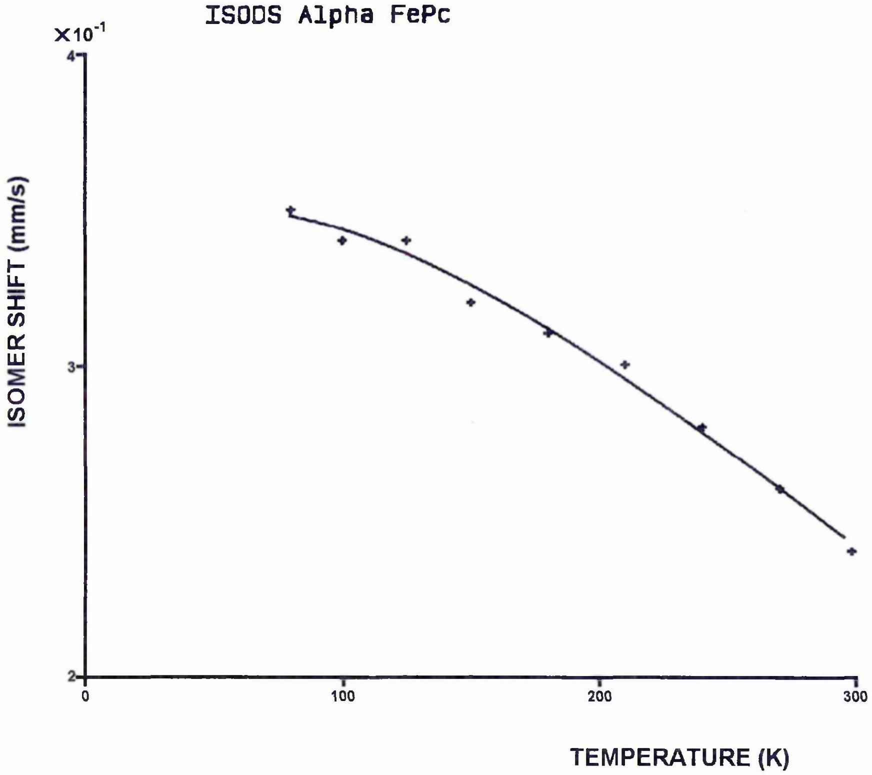

Figure 5.38 Isomer shift versus temperature graph for the alpha phase FePc.

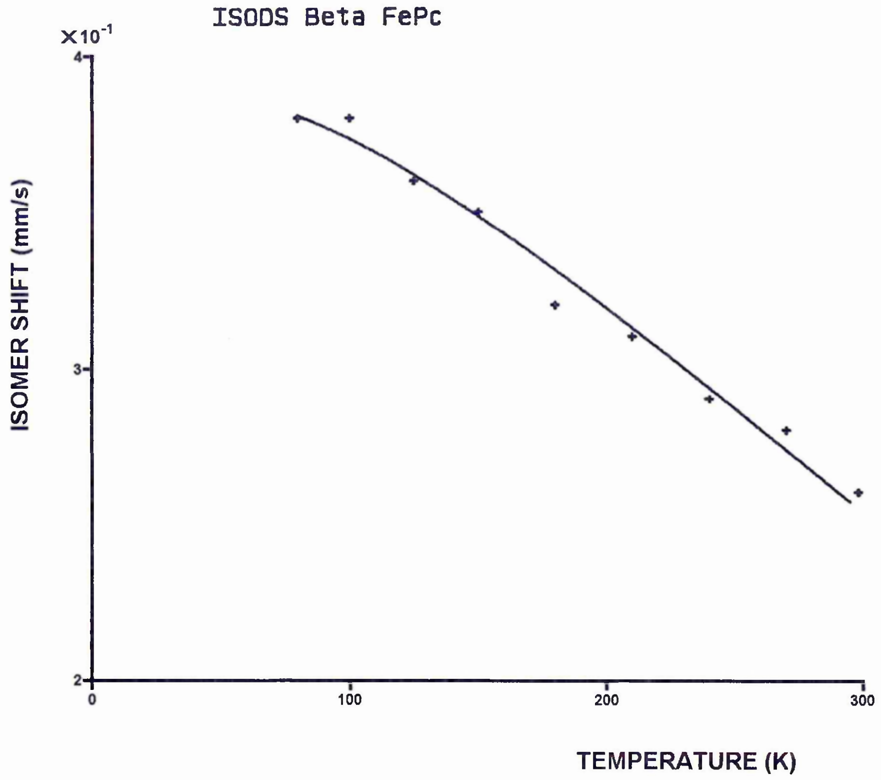

Figure 5.39 Isomer shift versus temperature graph for the beta phase FePc.

Table 5.10 Debye temperature and recoil free fraction of α and β-FePc using isomer shift data.

Sample	θ_D	f_{291K}
α-FePc	505	0.49
β-FePc	361	0.48

The calculated f_{291K} values from the second order Doppler shift data are effectively the same for both phases. This is confusing when compared with the absorption area calculations of f_{291K} (table 5.7), which show a marked difference between the alpha (f_{291K} = 0.14) and beta (f_{291K} = 0.36) phases. The different f_{291K} values obtained from the absorption area data seem more consistent with the different collection time for spectra of alpha and beta phases and the different structure of the two phases.

5.4.2.3 Temperature Dependence of the Quadrupole Splitting

The quadrupole splittings of both phases show a decrease with increasing temperature. Two fits have been attempted for each phase, one based on a model for high spin Fe^{2+} and one based on a linear model which is common in ferric compounds.

The quadrupole splitting of high spin ferrous iron is mainly due to the non-spherical $3d^6$ electron shell. The temperature dependence of the valence component of the quadrupole splitting can be derived with crystal field theory (16) and expressed in terms of a reduction factor F(T):

$$\Delta E_Q\ (T) = \Delta E_Q\ (Val)\ (0)\ F(T) + \Delta E_Q\ (Lat) \qquad (5.3)$$

Where:

ΔE_Q (T) = Quadrupole splitting at T K.

ΔE_Q (Val) (0) = Valence component of the quadrupole splitting at 0 Kelvin.

ΔE_Q (Lat) = Lattice component of the quadrupole splitting.

This model assumes zero probability of thermal occupation of the d_γ levels (figure 5.40) owing to the large energy difference. The degeneracy of the d_ε levels is removed by axial and rhombic distortions of the crystal field, resulting in two excited states separated by energies Δ_1 and Δ_2 from the ground state. Above absolute zero these excited states are thermally occupied.

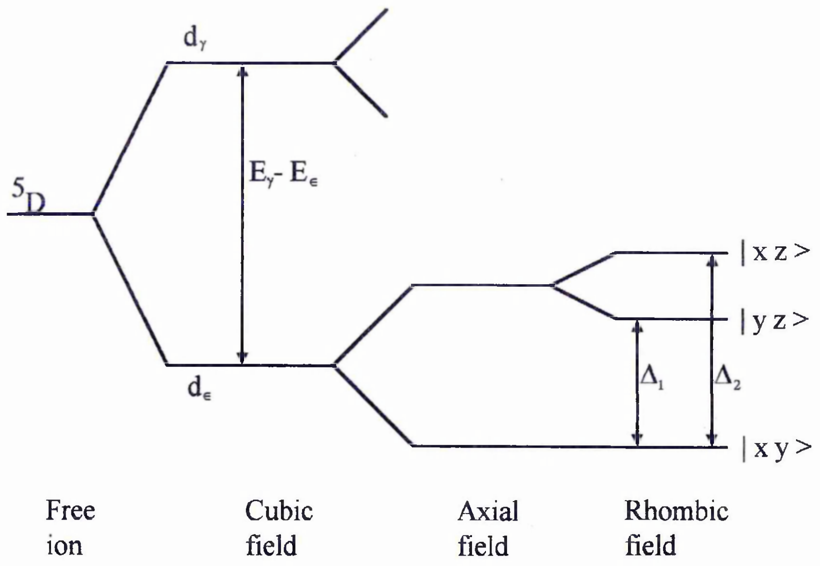

Figure 5.40 Crystal field splitting of the high spin Fe^{2+} ion.

Ignoring spin-orbit coupling allows F(T) to be expressed as follows:

$$F(T) = \frac{\left[1+\frac{-2\Delta_1}{e^{kT}}+\frac{-2\Delta_2}{e^{kT}}-\frac{\Delta_1}{e^{kT}}-\frac{\Delta_2}{e^{kT}}-\frac{-(\Delta_1+\Delta_2)}{e^{kT}}\right]^{1/2}}{1+\frac{-\Delta_1}{e^{kT}}+\frac{-\Delta_2}{e^{kT}}} \tag{5.4}$$

Where k=Boltzmann constant.

This high spin Fe^{2+} model was used in an attempt to fit the quadrupole splitting data against temperature for both phases. Figures 5.41 and 5.42 show the fits for the alpha and beta phases respectively. The calculated parameters are listed in table 5.11.

Table 5.11 High spin Fe^{2+} parameters for α and β-FePc.

SAMPLE	$E_Q(0)$Val mm/s	E_QLat mm/s	Δ_1 cm^{-1}	Δ_2 cm^{-1}	χ_2
α-FePc	0.48	2.02	306	10500	0.0005
β-FePc	3.8	0.63	18	4658	0.0014

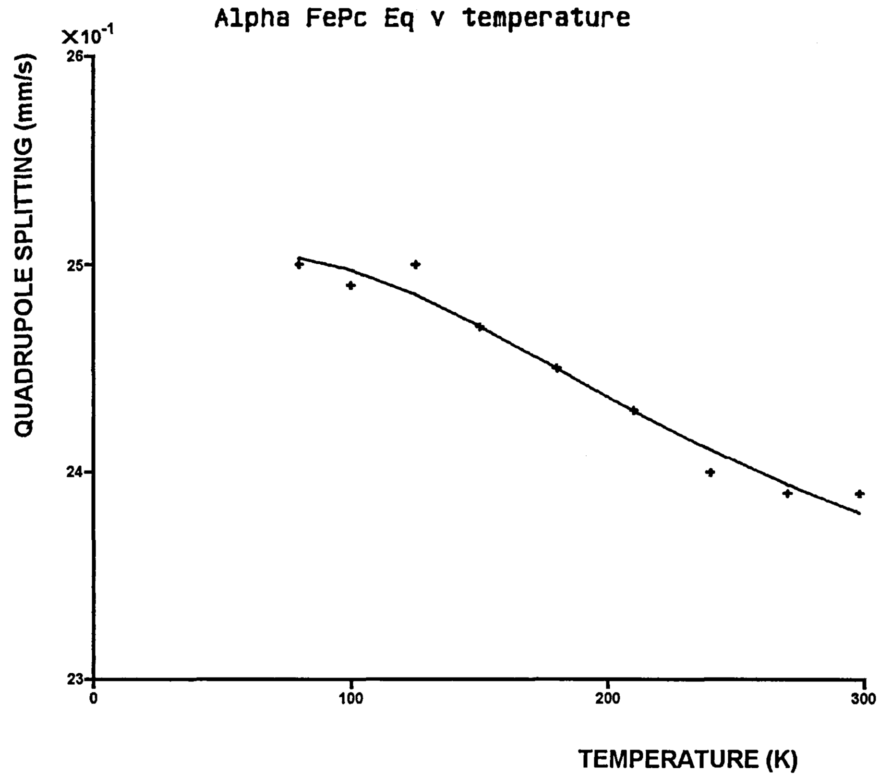

Figure 5.41 Quadrupole splitting data against temp. fitted to a Fe^{2+} model for α-FePc.

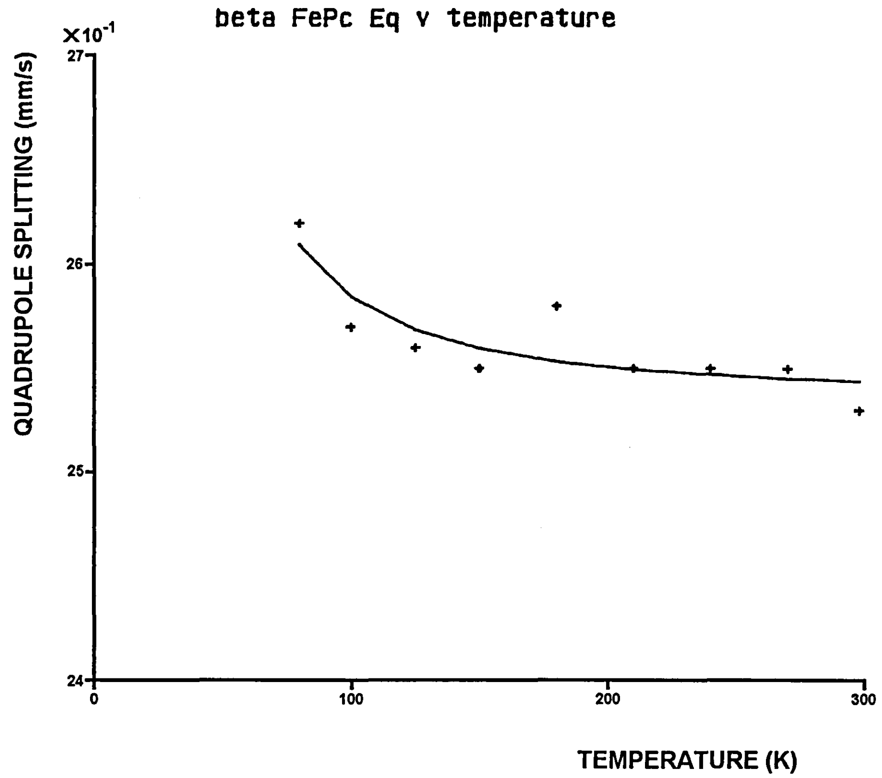

Figure 5.42 Quadrupole splitting data against temp. fitted to a Fe^{2+} model for β-FePc.

The fit for the beta phase is not very good and can be dismissed and the value for the separation of the excited states Δ_1 and Δ_2 are non physical for both fits and hence again dismissed. It can be concluded that the temperature dependence of neither phase is behaving as a high spin Fe $^{2+}$.

The temperature dependence of the quadrupole splitting could be explained by using a linear function, this is common in ferric compounds and assumes that the quadrupole splitting arises from the lattice contribution

$$\Delta E_Q\ (T) = \Delta E_Q\ (Lat)T = mT + \Delta E_Q\ (Lat)\ (0) \qquad (5.5)$$

Where:

m = Gradient mm/s/K

ΔE_Q (Lat) (0) = Quadrupole splitting at 0K

Figures 5.43 and 5.44 show the quadrupole splittings of the alpha and beta phases fitted to this linear function. The gradient and temperature coefficients are listed in table 5.12.

Table 5.12 Linear function fit for α and β-FePc.

Sample	Temperature coefficient gradient mm/s/K	ΔE_Q (Lat) (0) (mm/s)	χ^2
α-FePc	-5.9×10^{-4}	2.55	0.0008
β-FePc	-2.5×10^{-4}	2.61	0.002

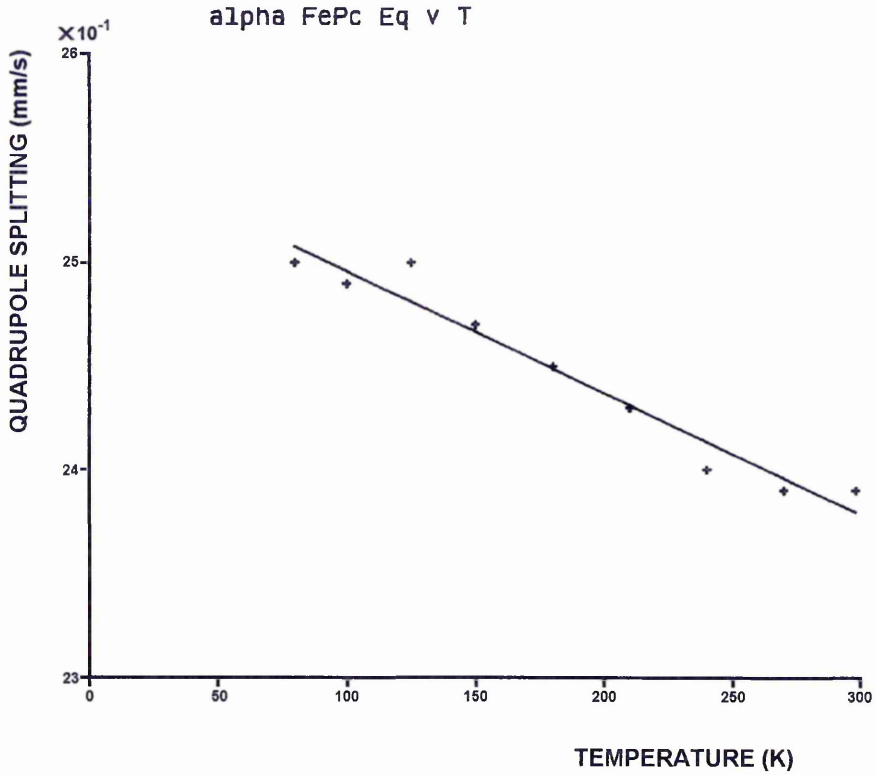

Figure 5.43 Quadrupole splitting against temp. fitted to a linear model for alpha FePc.

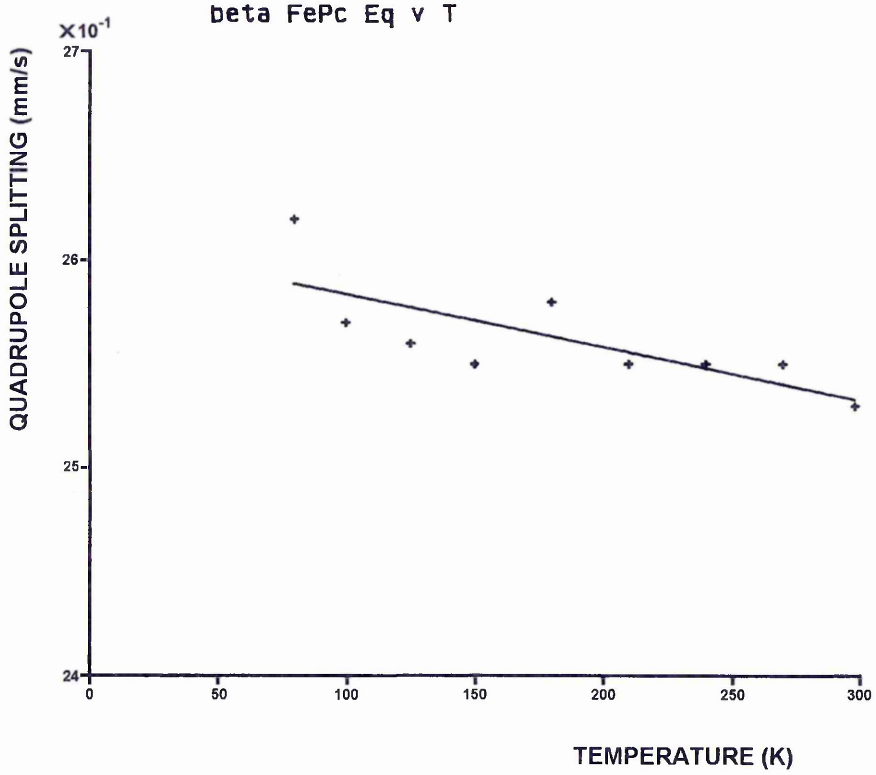

Figure 5.44 Quadrupole splitting against temp. fitted to a linear model for beta FePc.

The linear model gives reasonable fits and temperature coefficients. The higher temperature coefficient of the alpha phase could be compatible with the lower recoil free fraction of the alpha phase (derived from absorption area data) and indicative of a less rigid lattice.

The isomer shift data derived from the second order Doppler shifts give confusing results for θ_D and f_{291K} and cannot be explained, the absorption area data has been more informative and fits with the other information gained about the alpha and beta FePc.

The temperature dependence of the quadrupole splitting has been found to exclude the high spin Fe^{2+} model and the use of a linear function to fit the data was found to give reasonable fits and results, supporting the use of absorption area data to calculate the θ_D and f_{291K} of both phases.

5.4.3 Backscatter Mössbauer Spectroscopy

Backscatter Mössbauer spectroscopy gives surface information about a sample. Conversion electron Mössbauer spectroscopy (CEMS) has a probing depth of approximately 300nm and 66% of the electrons are detected from within 50nm (17) of a sample surface. Conversion x-ray Mössbauer spectroscopy (CXMS) is more penetrating up to 10μm (18).

This work has used backscatter techniques with FePc samples to obtain surface information about the material and to monitor any chemical changes occurring upon exposure to nitrogen dioxide.

Crude Pfaltz and Bauer FePc is a fairly pure sample (chapter 4, section 4.10.3) i.e. the transmission spectrum recorded at 80K did not contain any Fe (III) impurity which was present in the other crude samples. A sample of crude Pfaltz and Bauer (P&B) FePc was carefully pressed onto double sided Sellotape on a 3.0cm diameter PVC disc. The sample was placed in the CEMS detector and a CEMS spectrum collected over 3 days. Figure 5.45 shows the spectrum for crude P&B FePc and the parameters are listed in table 5.13.

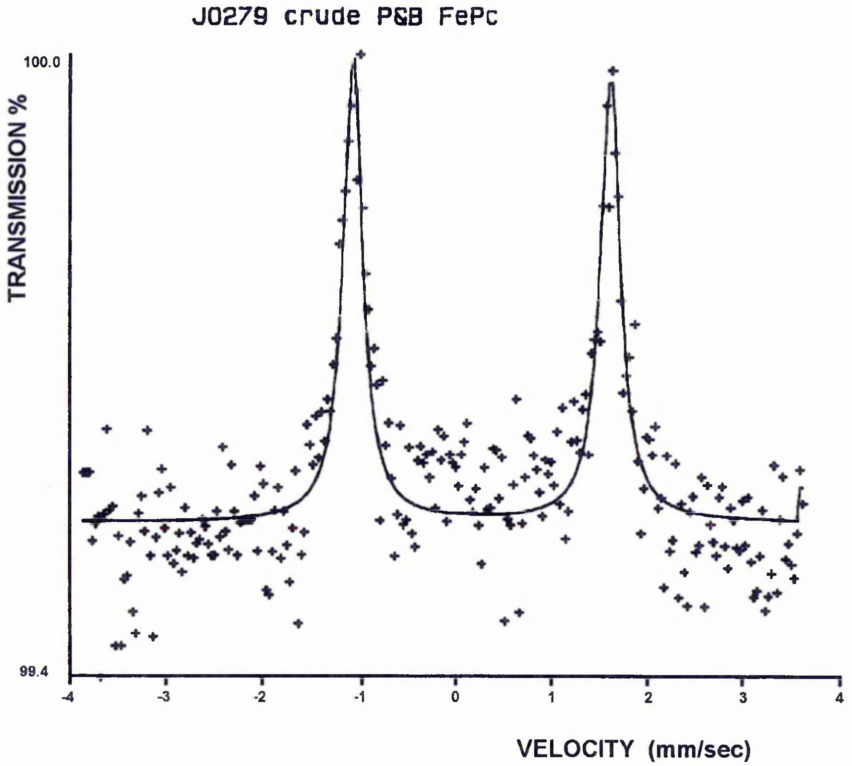

Figure 5.45 CEMS Mössbauer spectrum of crude P&B FePc.

Table 5.13 CEMS and transmission Mössbauer parameters of FePc.

Sample	Isomer shift ± 0.02mm/s (αFe)	Quadrupole split ± 0.02mm/s
JO279 CEMS crude P&B FePc RT	0.39	2.61
Transmission - α RT	0.35	2.39
Transmission - β RT	0.37	2.53
JO316 CEMS β-FePc	0.37	2.56

The spectrum consists of a quadrupole doublet typical of ferrous character. The parameters are outside the experimental error of the transmission parameters for the beta form but clearly are closer to this phase.

Having demonstrated the collection of a CEMS spectrum of crude FePc, the technique was applied to pure alpha and beta FePc samples. The alpha FePc being a powder was directly crushed onto double sided Sellotape and placed in the detector. The experiment was run for six days with no spectrum being collected. This was not surprising considering the low recoil free value of the alpha phase calculated from the variable temperature study. The beta FePc consists of purple needle-like crystals which were ground into a powder using a pestle and mortar. The sample was again crushed on to double sided Sellotape and a spectrum was seen after four days. Figure 5.46 shows the CEMS spectrum of beta FePc and the parameters are listed in table 5.13 (previous page).

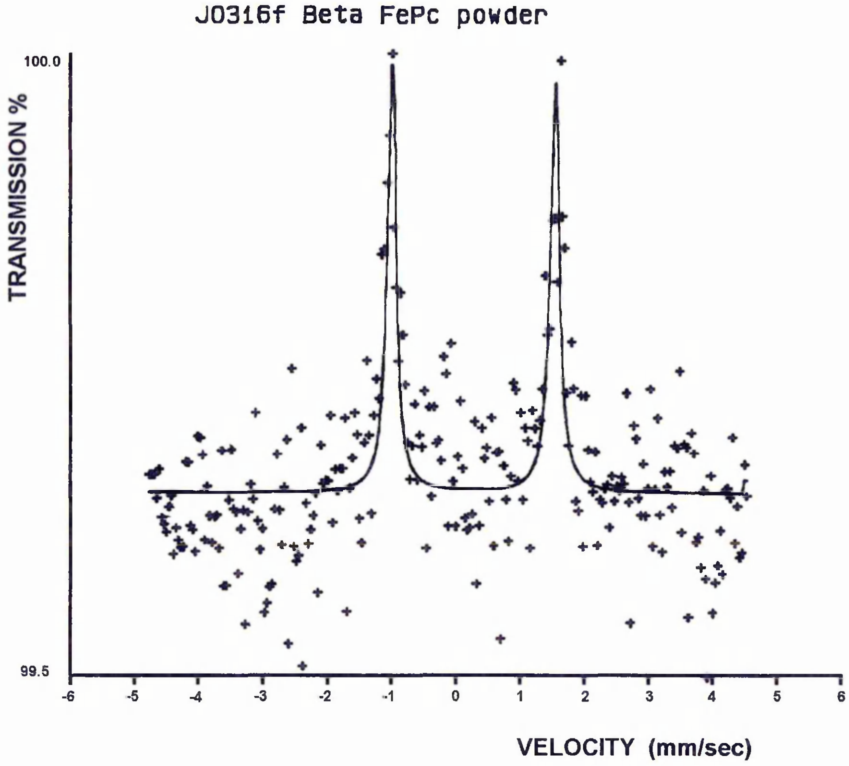

Figure 5.46 CEMS Mössbauer spectrum of beta FePc.

The parameters of the quadrupole doublet collected from the CEMS experiment of beta FePc at room temperature show good agreement to those obtained from beta FePc in a transmission experiment at the same temperature (see table 5.13). Evidence of a CEMS spectrum of beta FePc could be seen after 2 days. The higher recoil free fraction of beta FePc is a probable explanation as to why it has been possible to collect a CEMS spectrum of beta but not alpha FePc.

Attempts at collection of a CEMS or CXMS spectrum of a 1000nm alpha FePc film on a glass substrate were made. Owing to the low recoil fraction no peak was detected after four days. The maximum surface sensitivity for stainless steel by CEMS is 250nm (17) and by CXMS 10μm (17). Stainless steel has a large amount of iron present, but FePc has 10% of iron and so it was thought 1000nm could have been too thin for detection of backscatter spectra. 4000nm films of FePc were prepared in the Edwards coater. One of the films was annealed at 205°C for 3 hours in air in an attempt to convert the alpha phase to the beta phase. SEM work (section 5.2) has shown a phase change occurs by 205°C but there was no conclusive evidence that the phase became the beta form as observed in the bulk. The alpha film failed to produce a CEMS spectrum after 3 days. The annealed film also showed no peak in the CEMS experiment after 3 days. Possible reasons for failure to collect CEMS spectra of an FePc film are:

- the alpha film has a low recoil free fraction and it is not expected to produce a CEMS spectrum.
- annealing the alpha film at 205°C alters the phase but the produced phase may not be beta FePc and could still have a low recoil free fraction
- the films could be too thin for CEMS work owing to the small percentage of iron present in the compound.

To determine whether other iron organic compounds were similar to FePc i.e. gave little or no emission in CEMS experiments and to check the experimental procedure, 1000nm films of ferric acetylacetonate (ferric AcAc) were vacuum sublimed on to glass substrates. The ferric AcAc film was placed in the CEMS detector and left to accumulate a spectrum. After four days no peak was seen. This result indicated that collection of CEMS spectra from thin organic films other than FePc is also difficult, possibly for the reasons outlined above. To allow progress to be made pressed powder fluoresors were used for further studies.

5.5 GAS SENSING USING MÖSSBAUER SPECTROSCOPY

Nitrogen dioxide (NO_2) is a toxic gas which can be hazardous to health. FePc has been shown to respond to NO_2 and owing to the interest in monitoring this gas in the workplace the following set of experiments were carried out.

The aim of this set of experiments was to place an FePc sample in the backscatter detector and allow NO_2 to flow through the detector so that in vitro monitoring of the response before, during and after exposure to NO_2 could be monitored. The experiments were carried out at ambient temperature and pressure hence mimicking gas sensor operating conditions.

Cylinders containing 90ppm NO_2 normally contain oxygen (O_2) to prevent dissociation by forcing the following equilibrium to the left.

$NO_2 \rightleftharpoons NO + \frac{1}{2} O_2$

Presence of the oxygen would oxidize the anode in the CEMS detector and so was removed and replaced with helium. Helium was chosen since this is the normal ionising gas used in the CEMS experiment. To ensure that dissociation had not occurred without the presence of oxygen tests were carried out using Drager tubes. The tests showed the presence of NO_2 in the range 80-90ppm indicating no dissociation. Figure 5.47 shows a schematic diagram of the apparatus allowing the dilution of NO_2/He and delivery of the gas to the CEMS detector.

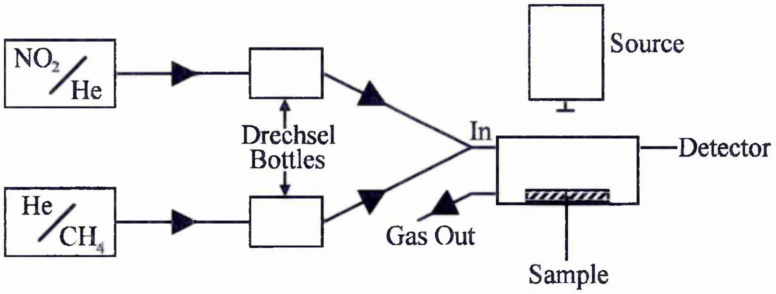

Figure 5.47 Schematic diagram of dilution and delivery of NO_2/He to the CEMS detector.

A CEMS spectrum of beta FePc powder crushed onto double sided Sellotape was recorded with the normal He/CH_4 gas mixture. The NO_2/He was then mixed with the He/CH_4 gas. The dilution was crude (i.e. 35 bubbles/min He/CH_4 : 9 bubbles/min NO_2/He) and resulted in about 15-20ppm NO_2 entering the detector. A CEMS experiment was carried out whilst the NO_2/He was bubbling through the detector. No spectrum was seen after 3 days. The NO_2 was turned off and immediately a CEMS experiment was attempted on the same sample without NO_2 flowing. This was not successful.

A CEMS spectrum was recorded of the beta FePc powder before exposure to NO_2, but during and after exposure to NO_2 a CEMS spectrum could not be collected.

Possible reasons for this failure:

- the NO_2 could be adsorbing onto the anode wire in the CEMS detector preventing any signal.

- the NO_2 could be chemically reacting on the surface and in the bulk with the beta FePc and preventing the escape of the conversion electrons from the surface.
- the NO_2 could be adsorbing onto the surface of the beta FePc, again preventing escape of the conversion electrons.

Further experiments were carried out to investigate these possible effects.

1. The pulse height spectrum was viewed using the β-FePc sample whilst bleeding NO_2 into the detector. With a high flow of NO_2 the pulse height spectrum began to tail off after an hour. Bubbling more He/CH_4 through the detector recovered the pulse height spectrum. This indicated that it could be the adsorption of NO_2 on the apparatus or surface of the sample affecting the pulse height spectrum; the He/CH_4 when bubbled through vigorously appears to remove the adsorbed NO_2.

2. Stainless steel (SS) contains much more iron than FePc and so a CEMS spectrum of SS collects much more quickly than one of FePc. CEMS spectra of SS before, after, and during exposure to NO_2 were collected. Table 5.14 shows the Mössbauer parameters. The Mössbauer spectra consist of a singlet.

Table 5.14 Mössbauer parameters of stainless steel before, during and after exposure to NO_2.

Stainless steel sample	Isomer shift mm/s ± 0.02 mm/s	Half width mm/s ± 0.02 mm/s
Before NO_2 exposure	-0.22	0.17
During NO_2 exposure	-0.20	0.18
After NO_2 exposure	-0.22	0.17

The spectra were accumulated over 26 hours. The pulse height spectrum during this time was normal and did not stop. This indicates that the NO_2 coating the anode wire does not affect the performance of the detector. Because of the inconclusive and contradictory evidence arising from the backscatter in vitro gas exposure experiments, a transmission experiment at 80K was carried out with beta FePc powder. 80mg beta FePc powder was mixed with graphite, placed in a sample holder and inserted into the liquid nitrogen cryostat. A spectrum (figure 5.48) with a characteristic quadrupole doublet corresponding to beta FePc parameters (table 5.15) was recorded. The sample holder was then opened and the powder placed in a jar filled with 90ppm NO_2 for 48 hours. The sample was placed back in the sample holder and immediately inserted into the cryostat and a spectrum recorded at 80K. The parameters are listed in table 5.12 and the spectrum shown in figure 5.49.

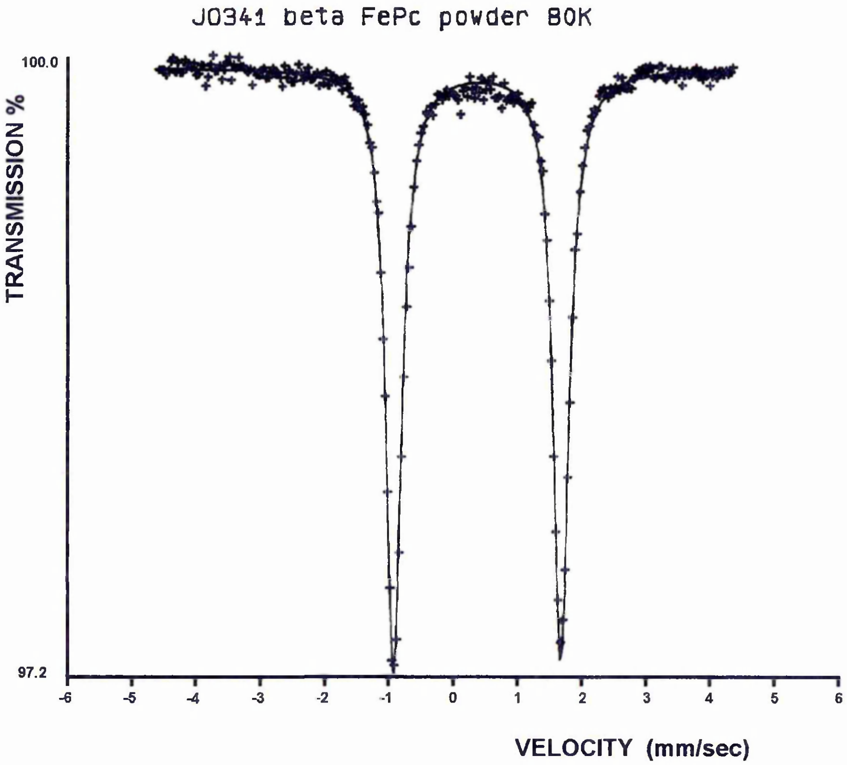

Figure 5.48 Transmission Mössbauer spectrum of beta FePc before exposure to NO_2.

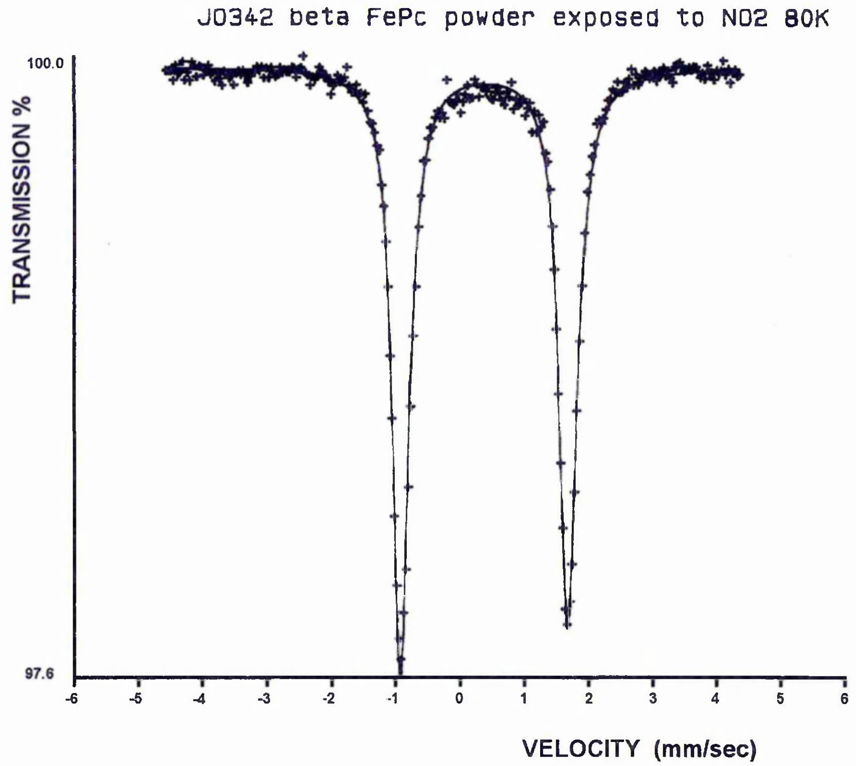

Figure 5.49 Transmission Mössbauer spectrum of beta FePc after exposure to NO_2.

Table 5.15 Transmission Mössbauer parameters of β-FePc before and after exposure to NO_2.

Sample	Isomer shift mm/s ± 0.02mm/s (α-Fe)	Quadrupole splitting mm/s ± 0.02mm/s
β-FePc	0.47	2.60
β-FePc exposed to 90ppm NO_2	0.47	2.60

The Mössbauer parameters are identical which demonstrates that NO_2 had not chemically reacted with the bulk beta FePc.

To determine whether NO_2 is adsorbing onto the surface of the beta FePc powder preventing the escape of conversion electrons, the following experiments were carried out.

Beta FePc powder crushed onto double sided Sellotape was left in a jar of 90ppm NO_2 for 48 hours. A CEMS experiment was attempted with this sample but no emission could be detected and the pulse height spectrum stopped. The sample was placed back in NO_2 for a further 48 hours and a CXMS experiment carried out. The gas used for CXMS is argon 95% and methane 5%. After 3 days a spectrum could be seen and was saved after 6 days. The conversion x-ray Mössbauer parameters are listed in table 5.16 and the spectrum shown in figure 5.50. The failure to collect a CEMS spectrum but the success of collecting a CXMS spectrum suggests that the NO_2 adsorbs onto the surface of the powder, preventing the escape of the conversion electrons hence the surface CEMS absorption is not seen. CXMS is comparatively a bulk technique and x-rays can escape from further in the sample forming a spectrum.

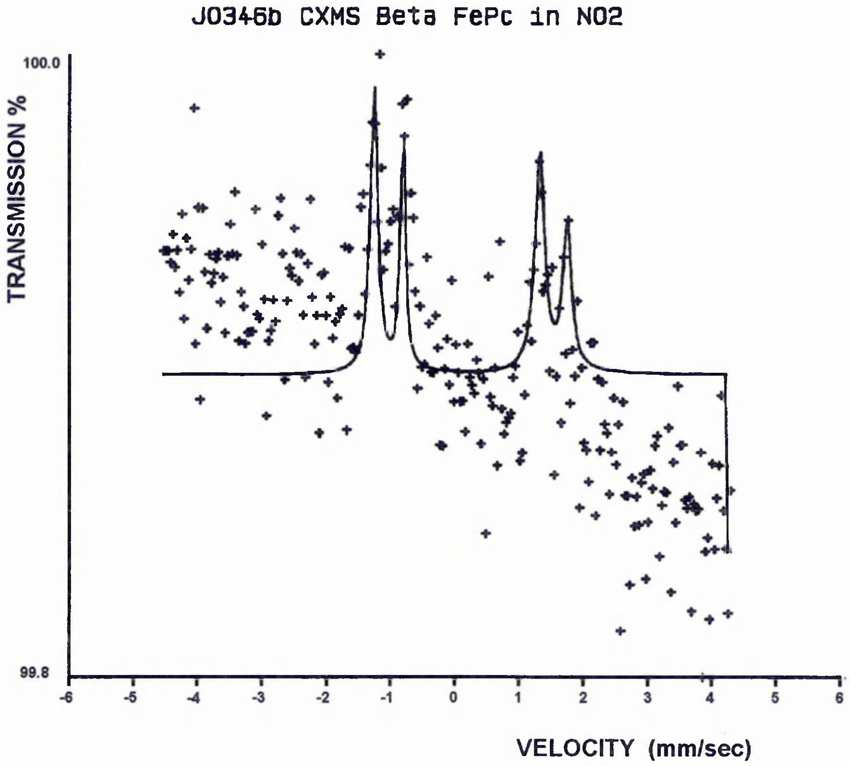

Figure 5.50 CXMS Mössbauer spectrum of beta FePc after exposure to NO_2.

Table 5.16 CXMS parameters of β-FePc after exposure to FePc.

Sample	δ(Fe) mm/s ±0.02mm/s	Δ mm/s ±0.02mm/s
JO346 (6 days CXMS)	0.01 0.58	2.58 2.56

The CXMS spectrum has been fitted as two quadrupole doublets, rather than the characteristic FePc single quadrupole doublet. This indicates that the NO_2 may have had some effect on the bulk of the sample. A CEMS experiment was run directly after the CXMS experiment and a spectrum collected (figure 5.51). The Mössbauer parameters are listed in table 5.17.

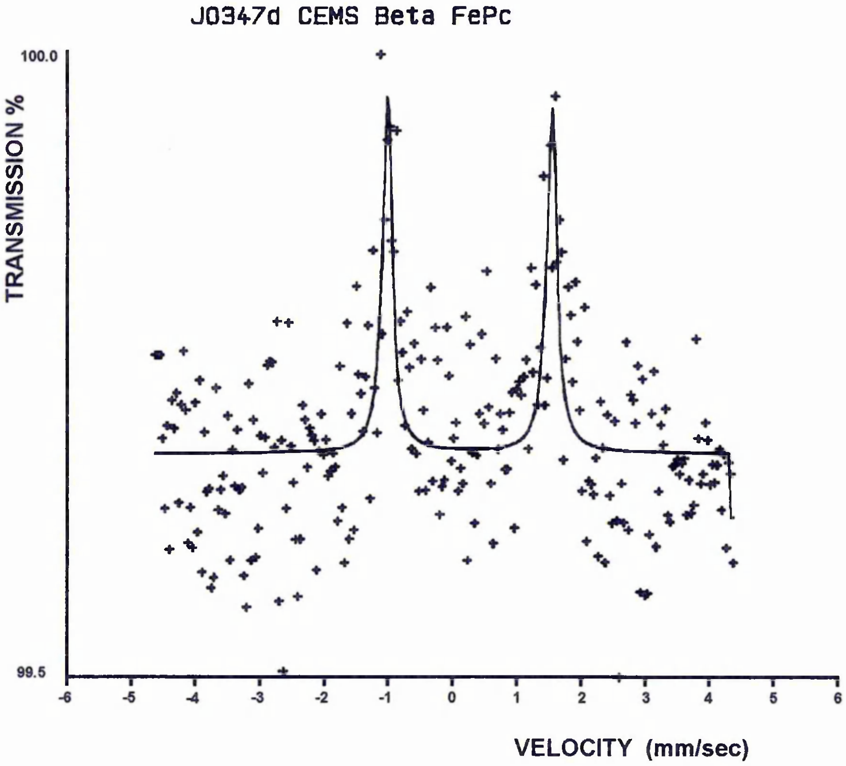

Figure 5.51 CEMS Mössbauer spectrum of beta FePc run directly after the CXMS experiment.

Table 5.17 CEMS parameters of β-FePc run directly after the CEMS experiment.

Sample	δ(Fe) mm/s ±0.02 mm/s	Δ mm/s ±0.02mm/s
JO347 (CEMS)	0.37	2.56

This suggests that the adsorbed NO_2 after six days has been removed by gas passing through the detector and hence allows collection of a CEMS spectrum.

The sample was placed in NO_2 for a further 48 hours and then placed in the detector and a CXMS experiment attempted again for a longer period (12 days) to improve the resolution. Figures 5.52 to 5.56 show the raw data of the CXMS experiment as it progressed over the 12 days. It is easy to see the resolution of the two doublets improving as the time increases. Two fits of this data were attempted, schematically represented in figures 5.57 and 5.58. The final fitted spectrum is seen (both fitting schemes) in figures 5.59 and 5.60 and the parameters listed in table 5.18.

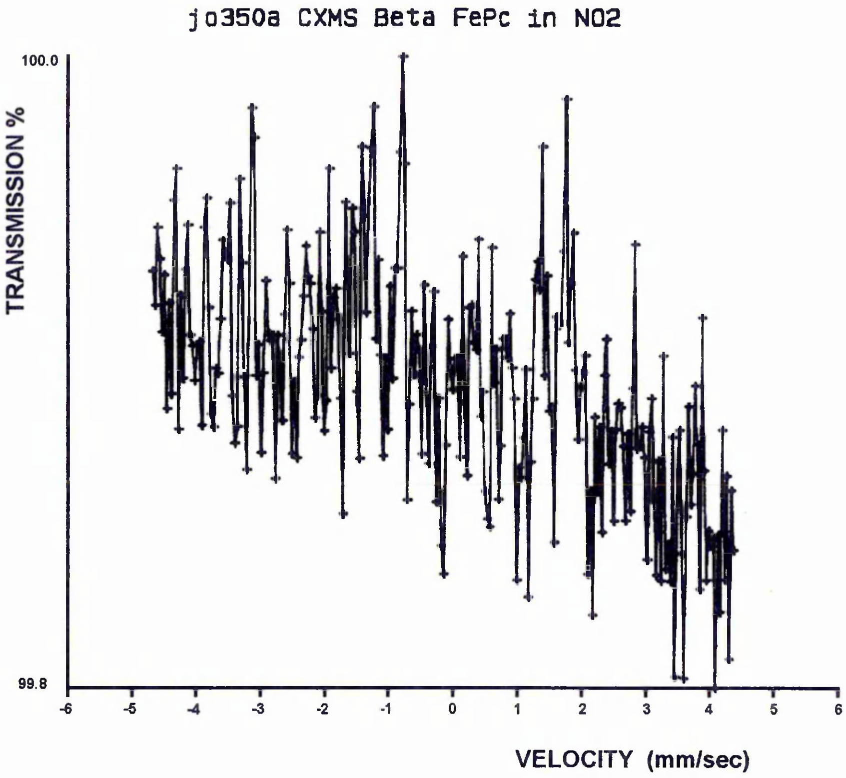

Figure 5.52 CXMS raw data spectrum of β-FePc, 2 days after initial exposure to NO_2.

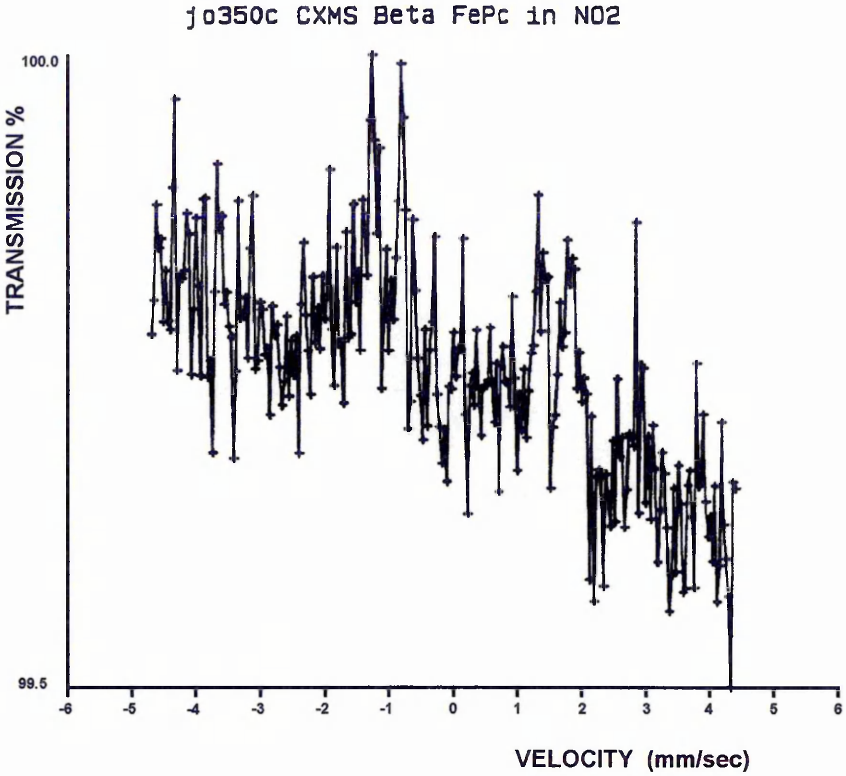

Figure 5.53 CXMS raw data spectrum of β-FePc, 6 days after initial exposure to NO_2.

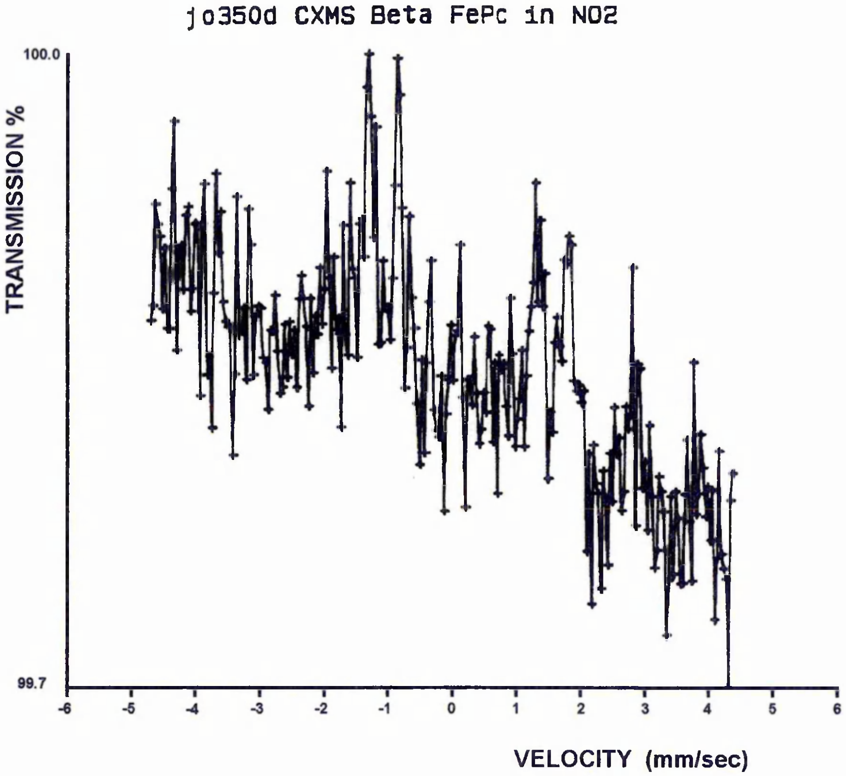

Figure 5.54 CXMS raw data spectrum β-FePc, 7 days after initial exposure to NO_2.

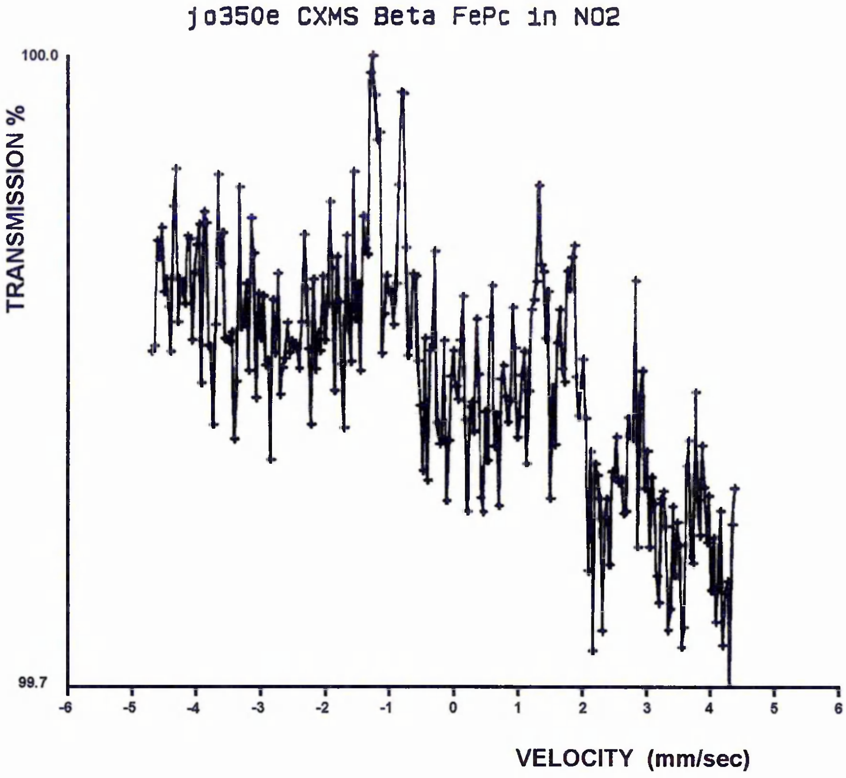

Figure 5.55 CXMS raw data spectrum β-FePc, 8 days after initial exposure to NO_2.

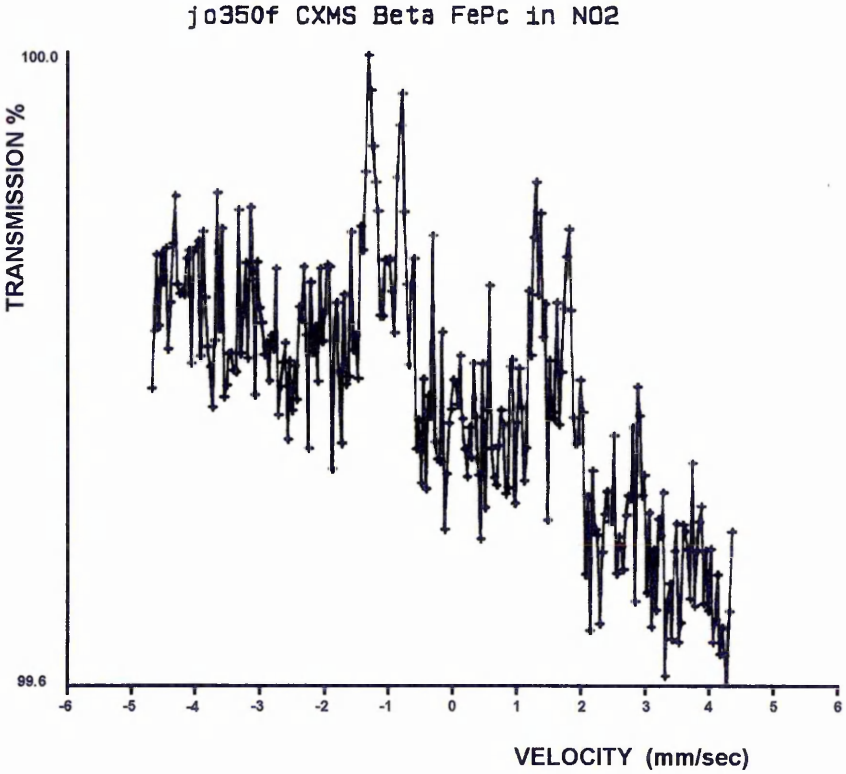

Figure 5.56 CXMS raw data spectrum β-FePc, 12 days after initial exposure to NO_2.

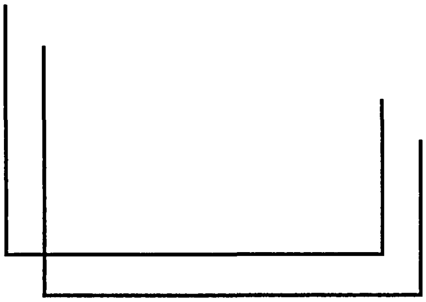

Figure 5.57 Schematic representation of one way of fitting the two quadrupole doublets - fit A.

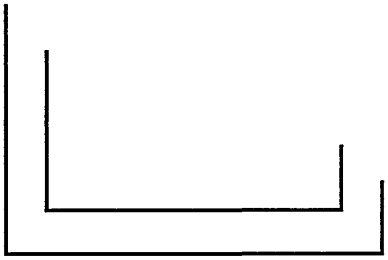

Figure 5.58 Schematic representation of a second fitting of two quadrupole doublets -fit B.

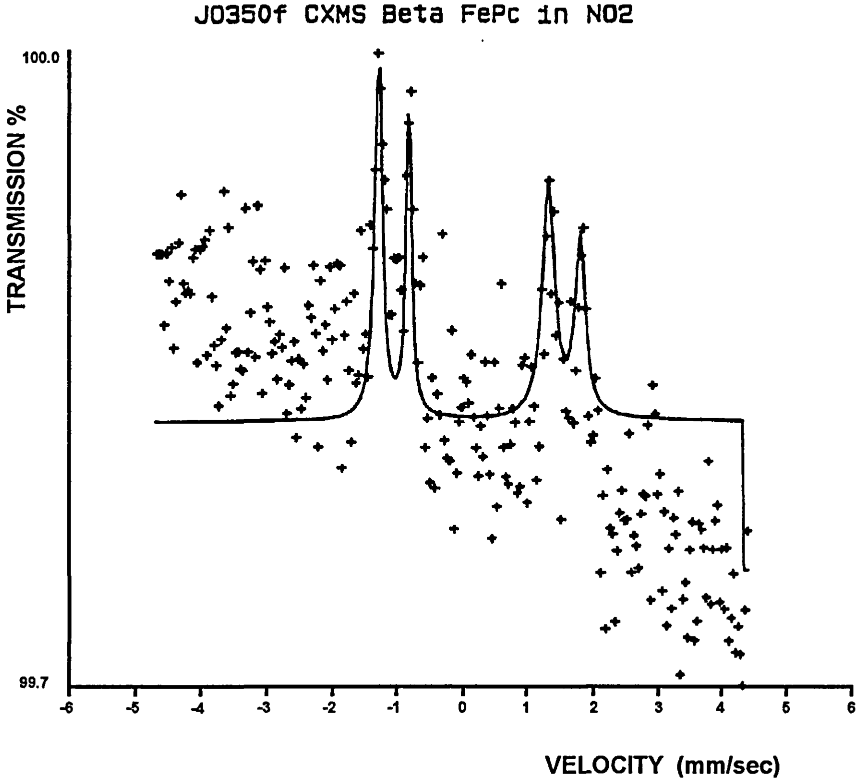

Figure 5.59 CXMS spectrum (fit A) β-FePc, 12 days after initial exposure to NO_2.

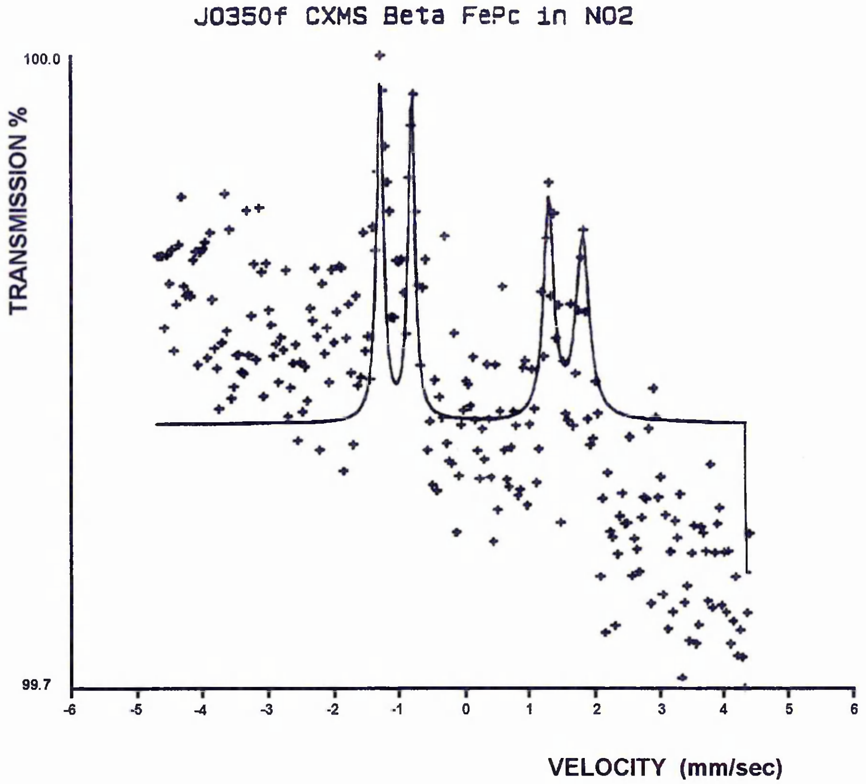

Figure 5.60 CXMS Mössbauer spectrum (data corresponds to fit B) of beta FePc collected 12 days after initial exposure to NO_2.

Table 5.18 CXMS parameters (two fits) of β-FePc after exposure to NO_2.

Sample	δ(Fe) mm/s ±0.02 mm/s	Δ mm/s ±0.02mm/s
JO350 Fit A	0.14 0.58	2.58 2.56
JO350 Fit B	0.38 0.39	2.15 3.14

Neither fit A or fit B contains the characteristic quadrupole doublet of β-FePc. The isomer shifts of fit A are similar to those found in β-FePc whilst the quadrupole splitting of fit B are the same as β-FePc. These results indicate that a chemical change may have occurred as a result of exposure to NO_2 in the surface layers of the β-FePc sample.

5.6 SUMMARY

Infrared spectroscopy has identified the as-deposited FePc film to be the alpha phase. There was a difference in the infrared spectrum of the FePc film annealed in air at 205°C compared with the as-deposited film. This is possibly a phase change but the resultant phase was not the beta form.

Scanning electron microscopy work supported the information gained from the infrared experiments since the crystallite size was seen to increase at about 205°C. Further heating caused the crystallites to merge together in clusters which could indicate the beginning of the sublimation process. This SEM work has shown that coating the samples with gold gives different images compared with uncoated samples. This highlights the possibility of incorrect interpretation of the structure of coated samples. The SEM work has shown that there is a difference in crystallite size from the as-deposited films and the films deposited onto substrates held at lower temperatures. (This difference was not identified by the infrared work).

Gas sensing studies have shown that the FePc film undergoes a change in resistance when exposed to NO_2 and Cl_2. FePc responds as a p-type semiconductor with NO_2 as expected. However upon exposure to Cl_2 the FePc acts as an n-type semiconductor. This latter result is confusing; one explanation is that the presence of water vapour on the film causes this response.

Transmission Mössbauer spectroscopy has been used to identify the alpha and beta phases of FePc in the solid form. A transmission variable temperature study showed that the alpha phase has a lower Debye temperature and hence recoil free fraction than the beta phase, when considering the temperature dependence of the area under the absorption line.

Backscatter (CEMS and CXMS) Mössbauer spectroscopy has been used in an attempt to monitor any chemical changes occurring upon exposure to NO_2. It has not been possible to collect backscatter spectra of an FePc film and so work was carried out on pressed powder forms of alpha and beta FePc.

The backscatter work has indicated that when beta FePc is exposed to NO_2, that the NO_2 adsorbs onto the surface of the sample preventing the escape of the conversion electrons, hence no CEMS spectra can be collected immediately after exposure. CXMS is comparatively a bulk technique and x-rays can escape from further in the sample allowing a CXMS spectrum to be collected immediately after exposure to NO_2. The adsorbed NO_2 is removed from the surface by gas passing through the detector hence allowing collection of a CEMS spectrum 6 days after exposure to NO_2.

REFERENCES

1 F. Karasek, J. Decius, *J. Amer. Chem.*, 1952, 74, 4716-4717.

2 J. Silver, P. Lukes, A. Houlton, S. Howe, P. Hey, M.Ahmet, *J. Mater. Chem.*,1992, 2, 849-855.

3 Y. Sadaoka, T. A. Jones, W. Gopel, *J. Mater. Sci. Lett.*, 1989, 8, 1095-1097.

4 Y. Sadaoka, W. Gopel, B. Suhr, A. Rager, *J. Mater. Sci. Lett.*, 1990, 9, 1481-1483.

5 Rosemount Engineering, Heath Place, Bognor Regis, PO22 9SH, 11340-AP-P-1 PNR.

6 S. Kanefusa, M. Nitta, *Sens. Actuators B*, 1992, 9, 85-90.

7 T. Jones, B. Bott, S. Thorpe, *Sens. Actuators*, 1989, 17, 467.

8 S. Pizzini, G. Timo, M. Beghi, N. Butta, C. Mari, J. Faltenmaier, *Sens. Actuators*, 1989, 17, 481-491.

9 S. Dogo, J. Germain, C. Maleysson, A. Nakajima, W. Nevin, *Appl. Phys. Lett.*, 1992, 61, 2184-2186.

10 T. Srivastava, J. Przybylinski, A. Nath, *Inorg. Chem.*, 1974, 13, 1562-1564.

11 J. Thompson, J. Ching, E. Fung, *Radiochim. Acta.*, 1972, 18, 57.

12 R. Taube, H. Drevs, E. Fluck, P. Kuhn, K. F. Brauch, *Z. Anorg. Allg. Chem.*,1969, 304, 297.

13 A. Hudson, H. Whitfield, *Inorg. Chem.*, 1967, 6, 1120.

14 I. Dézsi, A. Balázs, B. Molnar, V. Gorbehenko, I. Lukasherich, *J. Inorg. Nucl. Chem.*, 1967, 31, 1661-1666.

15 N. Greenwood, T. Gibb, *Mössbauer Spectroscopy*, Chapman and Hall, London, 1971, Page 50-54.

16 R. Ingalls, *Physical Review*, 133A, 1964, 3, 787.

17 M. J. Tricker in *Mössbauer Spectroscopy and its Chemical Applications*, Ed. Stevens and Shenoy, American Chemical Society, Washington D. C. 1981, Chapter 3, Page 63.

18 K. Swanson, J. Spijkerman, *J. Appl. Phys.*, 1970, 41, 3155.

CHAPTER SIX

CONCLUSIONS

6 SUMMARY

The aim of this work has been to study the surface and bulk properties of iron phthalocyanine (FePc), which has been used as a model in an attempt to study the gas sensing mechanism of metal phthalocyanines.

Crude FePc has been prepared in the laboratory in 75% yields based on a method by Tomoda et al (1). Mössbauer spectra of crude FePc from laboratory prepared, Kodak, and Pfaltz and Bauer FePc indicate that Pfaltz and Bauer is the purest sample followed by the laboratory FePc and that Kodak FePc is very impure. The β-phase of FePc can be prepared as purple needle like crystals from crude FePc using either entrainer sublimation or vacuum sublimation on to the walls of a tube along which a temperature gradient exists, the crystals forming at approximately 250°C. The alpha phase can be produced as a purple powder from crude FePc by vacuum sublimation on to a water cooled finger. Transmission Mössbauer spectroscopy has been used to confirm the identity of the alpha and beta phases. FePc films have been vacuum sublimed on to glass, graphite and potassium bromide discs using an Edwards vacuum coater.

Infrared spectroscopy has been used to show that a phase change occurs at 205°C from annealing studies in air, at different temperatures and scanning electron microscopy has been used to distinguish between the two phases of FePc. Two sets of SEM micrographs were recorded, one set from samples coated with gold and one set from uncoated samples. It was necessary to coat the FePc samples with gold in order to obtain a clear image when using the XL40 whereas the XL30 FEG produced good micrographs without gold coating. Comparing the micrographs from the two SEM instruments shows a large difference, and indicates that the Phillips XL40 was possibly producing micrographs of the gold coating which were very curvy, rather than the sharp crystals of the FePc film. However both sets of micrographs showed the same trend. The films which had been annealed at high temperatures showed an increase in the size of the microcrystallites, which as the temperature was further increased formed clusters, the film was presumably starting to melt or decompose. The FePc film as sublimed produced crystals 0.1µm in diameter.

Transmission Mössbauer spectroscopy has been used to gain information relating to the bulk of FePc. The transmission spectra of alpha and beta FePc consist of a single quadrupole doublet typical of iron (II) character. An asymmetry of the peaks appears as a result of crystal orientation effects. Collection of a conversion electron Mössbauer spectrum from an FePc film proved difficult and led to a transmission variable temperature Mössbauer study. In an attempt to explain these difficulties, the Debye temperatures were obtained, and the recoil free fractions of the different phases of FePc at room temperature calculated. The isomer shift values occurred between characteristic values for high and low spin ferrous iron whilst the quadrupole splittings were characteristic of high spin ferrous iron. The parameters confirmed the intermediate spin nature of FePc. The larger chemical shift values of the beta form compared with the alpha form can be explained in terms of the structure. The main difference in structure between the alpha and beta phases is the stacking angle of the molecules. In the beta form the nitrogen atoms of neighbouring molecules are present in the octahedral positions above and below the central iron atom. In the alpha form nitrogens from the nearest neighbours do not form the nitrogen octahedron around the iron atom. In the beta form, the iron atom has enhanced shielding of the s-electrons by d-electrons and results in a decrease in the s-electron density at the iron nucleus and hence a larger chemical shift in the beta form than the alpha form. Debye temperatures and hence recoil free fractions were obtained from absorption area and isomer shift data. The f values obtained from the absorption area data seemed more consistent with the collection times for spectra of alpha and beta phases and the different structure of the two phases. The temperature dependence of the quadrupole splitting has been found to exclude a high spin Fe^{2+} model behaviour and gave a reasonable fit to a linear function. The recoil free fraction of the beta form was higher than that of the alpha phase suggesting that the beta phase has a more rigid structure i.e. less free to vibrate in the lattice than the alpha phase. The f values also explain the difficulty in obtaining a CEMS spectrum of alpha FePc at room temperature. The alpha phase has a low θ_D and hence f_{291K} value i.e. low probability of recoil free events and it would not be expected to be easy to collect a spectrum.

Gas sensing work has shown that FePc responds with a change in conductance to nitrogen dioxide and chlorine. FePc has not proved to be a "good" gas sensor but can be used as a model to examine chemical or physical changes occurring when a metal phthalocyanine sensor is exposed to a gas.

Conversion electron Mössbauer spectroscopy gives surface information about a sample with a probing depth of approximately 300nm. Conversion x-ray Mössbauer spectroscopy is also a surface technique with a more penetrating depth of about 10µm. These backscatter Mössbauer techniques have been used to obtain surface information and to monitor any chemical changes upon exposure to nitrogen dioxide. The results indicate that the nitrogen dioxide is adsorbing on to the surface of the beta FePc and the conversion electrons are unable to escape from the surface, hence no CEMS spectrum can be collected. The bulk of the material was not affected by exposure to NO_2 since Mössbauer transmission spectra before and after exposure to NO_2 showed no change.

Conversion x-ray Mössbauer spectra of the material upon exposure to NO_2 have indicated that the NO_2 penetrates the near surface and causes a chemical change since two quadrupole doublets were seen instead of the single characteristic FePc quadrupole doublet.

6.1 Future Work

1. The beta phase film should be obtained and backscatter Mössbauer experiments completed with the film.
2. Further CXMS work with the beta FePc material before, during and after exposure to NO_2.
3. Other gases could be used to investigate the effect of FePc upon sensing a gas.
4. Gas sensing experiments at elevated temperatures.
5. A similar set of experiments with tin phthalocyanine could be carried out to see whether similar results are found.

REFERENCES

1 H. Tomoda, S. Ogawa, S. Shiraishi, *Chem Letts*. 1980, 1277-1280.

BIBLIOGRAPHY

1 G. M. Bancroft in *Mössbauer Spectroscopy: An Introduction for Geochemists*, McGraw Hill, London, 1973.

2 G. M. Bancroft and R. H. Platt in *Advances in Inorganic Chemistry and Radiochemistry* Volume II, Academic Press, New York and London, 1972.

3 F. Cotton, G. Wilkingson, *Advanced Inorganic Chemistry: A Comprehensive Text*, Wiley, New York, 1972.

4 T. Cranshaw, B Dale, G. Longnorth, C. Johnson, *Mössbauer Spectroscopy and its Applications*, Cambridge University Press, 1985.

5 U. Gonser in *Topics in Applied Physics: Mössbauer Spectroscopy*, Volume 5, Springer-Verlag, Berlin, Heidelberg, New York, 1975.

6 N. N. Greenwood and T. C. Gibb in *Mössbauer Spectroscopy*, Chapman and Hall Ltd, London, 1971.

7 G. J. Long in *Mössbauer Spectroscopy Applied to Inorganic Chemistry*, Vol. 1,Plenum Press, New York and London, 1984.

8 R. Moser, A. Thomas, *The Phthalocyanines,* CRC Press, Boca Raton, FL, 1983, Vols 1 and 2.

9 M. J. Tricker in *Mössbauer Spectroscopy and its Chemical Applications*, Ed. Stevens and Shenoy, American Chemical Society, Washington D. C. 1981.

ACKNOWLEDGEMENTS

The author wishes to thank Norman Bell, John Brooks, and Steve Thorpe for their supervision, guidance and support during the course of this research. Many thanks go to Sue Forder and Roger Smith for their advice and practical help especially in moments when the instrumentation seemed ready to give its last breath! Thanks too to Jess Cawley and Terry Hudson for their time spent, and patience in teaching me to try and use the SEM instrument, and for production of the SEM photographs. Thanks to the technicians in the MRI, Chemistry and Physics, for their help throughout my research. Many thanks also to Vicky Rogerson who has greatly helped in getting things done in Sheffield which I have been unable to do from Leicestershire. Special thanks to Tim Robinson, my fiancé, for his emotional support and vast time and effort spent on the production of diagrams (yes Tim they're excellent!) and much of the typing for my thesis. Thanks to my family and many friends for their support when things seemed difficult and the end was not in sight.

COURSES AND CONFERENCES ATTENDED

COURSES

December 1990	Advances in Chemical and Biological Sensors UMIST Manchester
Autumn 1990	Introduction to Mössbauer Spectroscopy Sheffield Hallam University

CONFERENCES

32nd Mössbauer Spectroscopy Discussion Group Meeting

July 1991, City University - London - Poster Presentation.

33rd Mössbauer Spectroscopy Discussion Group Meeting

July 1992, University of Nottingham - Oral Presentation.

34th Mössbauer Spectroscopy Discussion Group Meeting

September 1993, University of Nottingham.

Instrument Science and Technology Group Meeting - Biosensors

February 1991, The Institute of Physics - London.

The Royal Society of Chemistry 150th Anniversary Congress

April 1991, Imperial College - London.

Sensors and Their Applications

September 1991, Edinburgh - Poster Presentation.

Eurosensors VI

October 1992, San Sebastian - Spain - Oral Presentation.

The 4th International Meeting of Electronic Properties of Metal/Non-metal Microsystems

September 1993, Sheffield Hallam University - Oral Presentation of this Work by J. S. Brooks.

The 4th International Meeting on Chemical Sensors

September 1992, Tokyo - Japan - Poster Presentation of this work by S. Thorpe as it was not possible to attend this conference.

PUBLICATIONS

1. J. S. Brooks, N. Bell, J. O'Rourke, S. Thorpe, Iron-57 Mössbauer Studies of Iron Phthalocyanine Gas Sensing Systems in *Sensors - Technology, systems and applications*, Ed. KTV Grattan, 1991, 163-169.

2. J. K. O'Rourke, J. S. Brooks, N. A. Bell, S. Thorpe, Mössbauer and Microstructural Studies of Iron Phthalocyanine as a Potential Gas Sensor, *Sensors and Actuators B*, 1993, 13-14, 690-692.

3. J. K. O'Rourke, J. S. Brooks, N. A. Bell, S. Thorpe, Mössbauer and Microstructural Studies of Iron Phthalocyanine as a Potential Gas Sensor, *Sensors and Actuators B*, 1993, 15-16, 90-97.

4. J. K. O'Rourke, J. S. Brooks, N. A. Bell, S. C. Thorpe, Fe-57 Mössbauer Study of Iron Phthalocyanine, *Int. J. Electronics*, 1994 (to be published).